Transport Layer Optimization for High-efficiency and Stable Planar n-i-p Perovskite Solar Cells

by

Bao TU

Doctor of Philosophy in Applied Physics and Materials Engineering

2020

Institute of Applied Physics and Materials Engineering

University of Macau

Transport Layer Optimization for High-efficiency and Stable Planar n-i-p Perovskite Solar Cells

by

Author: Bao TU

SUPERVISOR: Prof. Haifeng Li

Co-SUPERVISOR: Prof. Zikang Tang, Prof. Zhubing He

DEPARTMENT: Institute of Applied Physics and Materials Engineering

Doctor of Philosophy in Applied Physics and Materials Engineering

2020

Institute of Applied Physics and Materials Engineering

University of Macau

Acknowledgements

Firstly, I want to give my sincerely gratitude to prof. Haifeng Li, prof. Zikang Tang and prof. Zhubing He, for their selfless guidance, encouragement, and inspiration during my doctoral period.

This joint PhD program is offered by the collaboration between the University of Macau (UM) and Southern University of Science and Technology (SUSTech). The PhD candidate is jointly sponsored and supervised by UM and SUSTech.

Simultaneously, I want to express my sincerely acknowledgment to chair prof. Songnan Qu, prof. Guichuan Xing, prof. Huaiyu Shao, prof. Hui Pan, prof. Aleksandra B. Djurišić, prof. Xugang Guo, prof. Alan Manching Ng and prof. Xingqiang Shi. I also thank Mr. Huqiang Yi from the Materials Characterization and Preparation Center belongs to the Department of Materials Science and Engineering (SUSTech) for some related characterizations.

In addition, I also want to thank all lab mates and friends, Wei Chen, Yinghui Wu, Yangfan Shao, Xiyuan Feng, Si Wu, Yinghao Zhu, Junchao Xia, Pengfei Zhou, Haoshi Gao, Yanlin He, Yudong Zhu, Leiming Xu, Xiaoqi Lan, Zhenggang Wu, Tian Chen, Guocong Chen, Yi Lin, Zhiqin Ying, Zheng Zhang, Yang Wang, Fangzhou Liu, for their helpful discussion and valuable friendship. Finally, I would like to express my gratitude to my family, especially my husband for his deeply understanding and support.

Abstract

Pollution-free renewable energy is becoming important at an accelerated pace to promote the comfortable survival of human civilization. Solar energy is inexhaustible and abundantly surface energy which can satisfy the growing energy demand. With outstanding optical and electrical properties of perovskite, perovskite solar cells (PSCs) has attracted tremendous attention and shown its simple manufacturing process and rapidly increased power convention efficiency (PCE). But there are also many obstacles in their development process, mainly include the further to be improved PCE, poor stability, small cell area and toxicity. And here we mainly committed to solving the problems around PCE and stability. Transport layer plays a critical role in the final performance, and optimization of transport layer is conformed as an effect strategy to bring about high-performance and stable PSCs. Based on these, transport layer optimization was proposed to achieve stable PSCs with high efficiency. Firstly, electron transport layer (ETL) optimization was realized by molecular doping of SnO_2. After n-type doping, the electrons are transferred from high polarly σ-bond mainly to the peripheral tin atoms instead of directly connected tin atoms, results in the presence of delocalized electrons at the surface, and consequently increased conductivity and decreased work function. These in turn results in an increased built-in field and a decreased energy barrier at SnO_2/perovskite interface, enables the PCE improved to 20.69%. Following, ETL optimization was realized by defect passivation of SnO_2. Based on the novel method proposed, SnO_2 was transferred into H_2N-SiO_X@SnO_2, which could passivate the defects and alleviate charge accumulation effectively, results in an obvious improvement in open-circuit voltage (Voc) and PCE, along with improved stability.

Meanwhile, hole transport layer (HTL) optimization was also realized by introducing dopant free hole transport materials (HTMs) to replace 2,2',7,7'tetrakis-(N,N-di-4-methoxyphenylamino)-9,9'-spirobifluorene (Spiro-OMeTAD). Our results suggested that BTTI-C6 based device show an encouraging PCE (19.69%) which is comparable to the reference, and largely improved long-term illumination and thermal stability compared to Spiro-OMeTAD based devices. Overall, improved efficiency and stability are achieved by transport layer optimization, and some new novel optimization methods are proposed, which can provide guidance for further understanding around PSCs and improve performance.

Declaration

I declare that the thesis here submitted is original except for the source materials explicitly acknowledged and that this thesis as a whole, or any part of this thesis has not been previously submitted for the same degree or for a different degree.

I also acknowledge that I have read and understood the Rules on Handling Student Academic Dishonesty and the Regulations of the Student Discipline of the University of Macau.

Table of Contents

List of tables

List of schemes

List of figures

1. Background

1.1 Introduction

Owing to the environmental pollution and prospective reserves caused by the consumption of fossil fuels, fossil energy can't satisfy the demands for future sustainable development (Fu et al., 2018; Wadia, Alivisatos, & Kammen, 2009). Therefore, pollution-free renewable energy is becoming more and more important at an accelerated pace to promote the comfortable survival of human civilization. Among them, solar energy is inexhaustible and abundantly surface energy which can meet the growing energy demand of future generations (Ansari, Qurashi, & Nazeeruddin, 2018; Dubey et al., 2018). Solar energy can be absorbed by solar cells whose photoelectric properties (e.g., current, voltage or resistance) will be changed once affect by solar radiation and convert directly into electrical energy, and the production cost of solar cells has declined by 75% within less than a decade (Ansari et al., 2018). Due to the substantial price reduction in recent years, solar energy has now become a cost-effective and reliable source of energy. The pie chart in Figure 1.1 shows the cumulative total installed capacity of photovoltaic in the top ten countries in 2014 and 2019 (Ansari et al., 2018), and our country Chain is outstanding there.

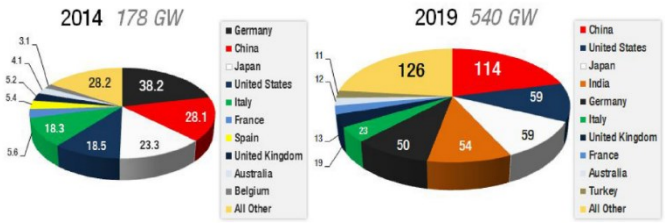

Figure 1.1 Pie chart of the cumulative total installed capacity of photovoltaics in the top ten countries in 2014 and 2019 (Ansari et al., 2018).

1.2 Solar cells

1.2.1 Development of solar cells

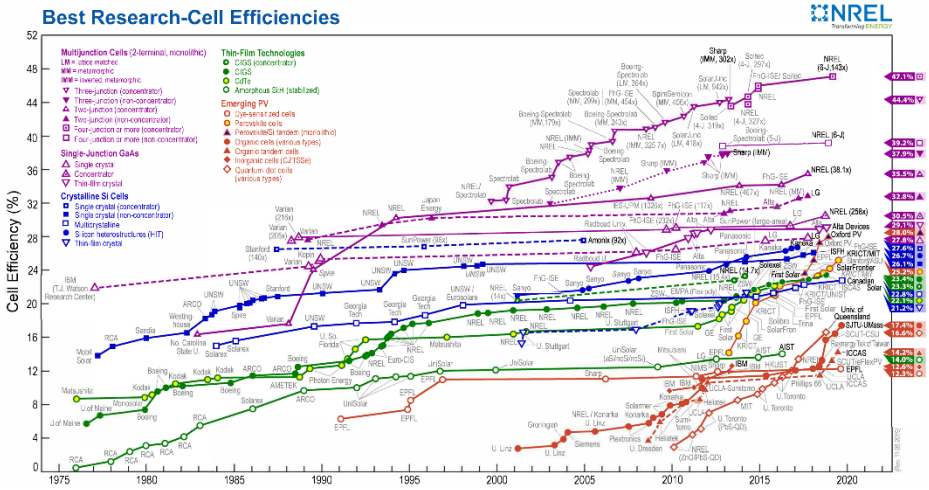

Figure 1.2 PCE statistics of solar cells from NREL.(NREL, 2020)

The history of solar cells can be traced back to 1839 when photovoltaic effect was first discovered by Becquerel (Becquerel, 1839). Based on the photosensitivity of selenium, the first solar cell with Au/Se/Metal structure was successfully prepared in 1876 (Adams & Day, 1876). In 1954, the crystal silicon solar cells with practical value up to 6% PCE was reported, which is an milestone in solar cells development (Chapin, Fuller, & Pearson, 1954). The proposed structures and mechanisms are continued to this day and provide guidance to researchers. In 1991, the first sensitization of dye molecules based on TiO_2 substrate was successfully prepared by Michael Grätzel, results in a PCE up to 7.9% (ORegan & Gratzel, 1991). In 2009, $CH_3NH_3PbI_3$ and $CH_3NH_3PbBr_3$ were used as dyes in dye-sensitized solar cells (DSSC) with 3.8% and 3.13% PCE, respectively (Kojima, Teshima, Shirai, & Miyasaka, 2009). The efficiency of solar cells is constantly being improved from the PCE statistics diagram (Figure 1.2) published by America New Renewable Energy Laboratory (NREL).

1.2.2 Principle of solar cells

Photovoltaic effect is a phenomenon when the device exposed to sunlight, the distribution of charge inside the device changes to generate current. And photovoltaic effect is the basic working principle of solar cells.

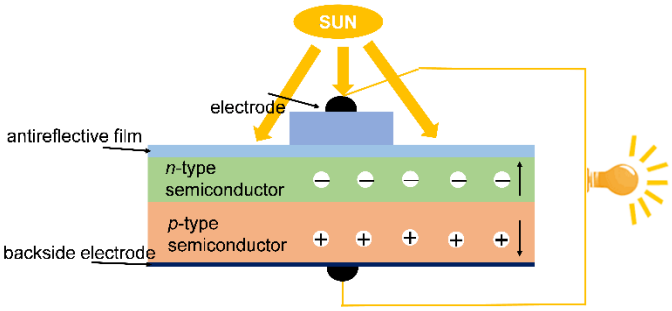

Figure 1.3 Schematic diagram of solar cells.

Figure 1.3 shows the working principle of solar cells. When the incident light (sunlight or sunlight simulated light source) illuminating on semiconductor surface, due to the greater photon energy compared to the band gap of semiconductor, numbers of photo-generated electron-hole pairs will be excited. Under the effect of built-in electric field, the generated photo-generated electron-hole pairs will be separated immediately. Following, electrons move to negative electrode, and holes to positive electrode. Finally, a potential difference will be formed between the positive and negative electrode. The existence of potential difference leads to the generation of photocurrent, then convert solar energy into electrical energy successfully.

1.2.3 Classification of solar cells

Solar cells have been discovered for almost 180 years since they were first discovered. Based on continuous improvement on manufacturing process, the types of solar cells have also become much more diverse. Here, according to the development stages, solar cells are classified as depicted in Figure 1.4.

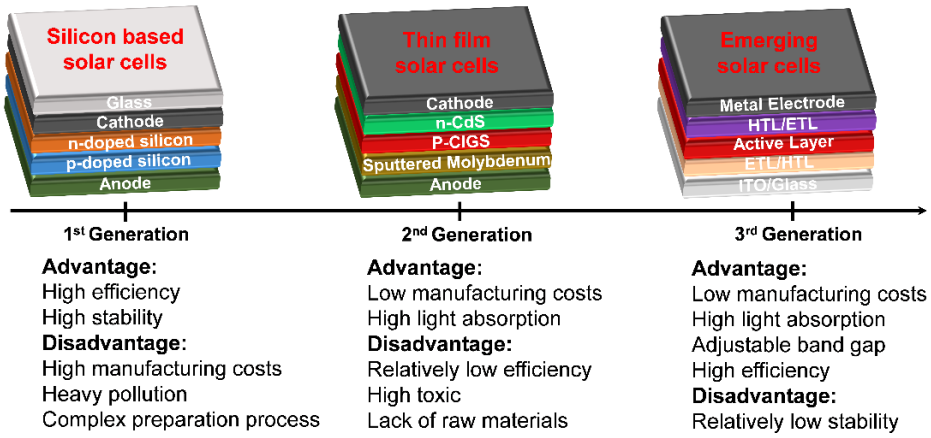

Figure 1.4 Classification of solar cells.

Silicon-based solar cells are the 1st generation solar cells which is built on monocrystalline and polycrystalline silicon (Rhodes et al., 2009). Due to the high efficiency and stability, silicon-based solar cells have accounted for much more than 80% of the world installed capacity today and currently accounts for 90% of the market shares (Gangopadhyay, Jana, & Das, 2013). While silicon-based solar cells are adverse in highly manufacture costs and pollution. The 2nd generation solar cells built on CdTe, amorphous silicon or copper indium gallium selenide which has been proposed as inexpensive alternative to 1st generation solar cells. It is cheaper but at the risk of reducing efficiency. Other thin-film technologies ongoing research are the 3rd generation solar cells, considered to be “emerging solar cells”, comprise by organic solar cells, DSSC, quantum dots solar cells, polymer solar cells, PSCs etc. PSCs is a promising solar cell among them, aroused considerable interest and attention from researchers.

1.3 Introduction of PSCs

In recent years, PSCs has attracted extensive research interests because of its simple manufacturing process and rapidly increased PCE, which has surpassed the efficiency from thin-film technologies.(Burschka et al., 2013; Green, Ho-Baillie, & Snaith, 2014; Kang & Park, 2019; Li et al., 2016)

1.3.1 Introduction of perovskite materials

Perovskite, a class of material discovered for the first time as $CaTiO_3$ (Nasti & Abate, 2019). Nowadays, perovskite formula is referred to simply as ABX_3 (Figure 1.5), where A is usually monovalent cation (Cs^+, formamidinium (FA), methylammonium (MA) or Rb^+,) or their mixture, B is usually divalent metal cation (Pb^{2+} or Sn^{2+}) or their mixture, and X is usually halide ion (I^-, Br^- or Cl^-) or their mixture (K. Wang et al., 2019). The ideal crystal structure of perovskite is usually cubic lattice where A located in position (0,0,0), B located in position (1/2, 1/2, 1/2) and X located in position (1/2, 1/2, 0), (1/2, 0, 1/2) and (0, 1/2, 1/2) (Nasti & Abate, 2019).

Ionic radii are important for perovskite and determined the Goldschmidt tolerance factor (t)

$$t = (R_X + R_A)/\sqrt{2}(R_X + R_B)$$

Where R_X, R_A and R_B are the ionic radii of halide ion, monovalent cation and divalent metal cation, respectively (Amat et al., 2014). According to this formula, perovskite material will show highest symmetrical cubic crystal structure when the tolerance factor is equal to 1. And, when the tolerance factor deviates from 1, the decreased symmetry can be described to the torsional phase transition in the lattice of perovskite. And for stable crystal structure, tolerance factor should be between 0.78 and 1.05 (Yang et al., 2017; Wu et al., 2008).

Perovskite, which is considered to be a promising material for photoelectric devices due to its attractive qualities (e.g. high absorption coefficient, tunable band gap, long carrier diffusion lengths, low temperature solution process, low trap densities and so on), as shown in Figure 1.5 (Shi, Duan, Zhao, Luo, & Zhang, 2020; Wu, et al., 2019). Their

superior optical and electrical properties make them take part in ideal candidates in light-emitting diode (LED), laser, photodetector and especially as the absorption material in solar cells (Lee et al., 2015; Lin et al., 2018; Saliba et al., 2016).

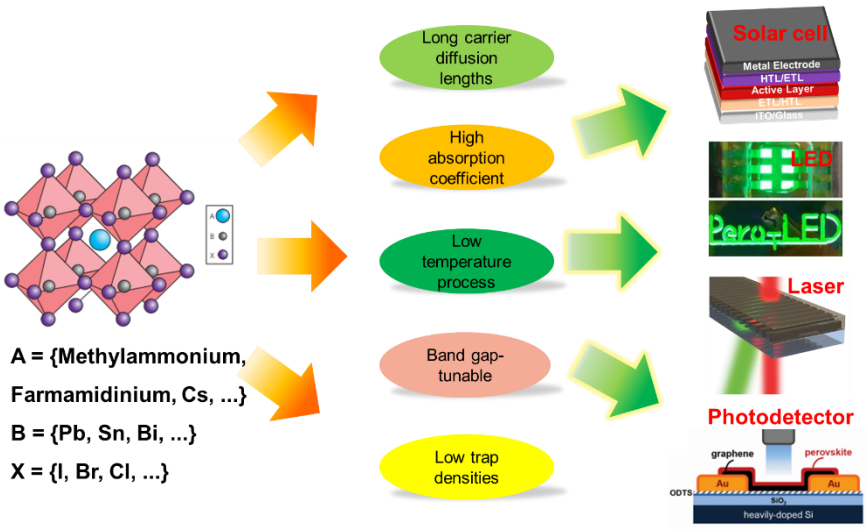

Figure 1.5 Introduction of perovskite materials.(Green et al., 2014; Lee et al., 2015; Lin et al., 2018; Saliba, et al., 2016; Shi et al., 2020)

1.3.2 Development of PSCs

The introduction of perovskite materials into photovoltaic application can be traced back to 1956 (Nasti & Abate, 2019). While the photovoltaic phenomenon based on it at that time was only related to internal electric field. Until 1978, MA ions ($CH_3NH_3^+$) was first introduced into the crystal structure of perovskite, results in a typical organic-inorganic hybrid perovskite material $CH_3NH_3MX_3$ (Weber, 1978). In 2001, perovskite as potential material for breakthrough application as semiconductor was proposed by Mitzi (Mitzi, 2001). The first pioneering work of PSCs was reported in 2006 when $MAPbI_3$ was used as a dye in DSSC with external quantum efficiency (EQE) up to 2.19% (Kojima, Teshima, Miyasaka, & Shirai, 2006). In 2009, other perovskite was used as dye in DSSC and achieved a PCE about 4% (Kojima et al., 2009). A few years later, an astonishing result of 6.54% EQE was obtained in 2011 where liquid electrolyte was used to extract

holes from the dye and transfer holes to the electrode (Im, Lee, Lee, Park, & Park, 2011). Up to 2012, PSCs has achieved a real breakthrough when modified the original configuration by using all-solid hole transporting material Spiro-MeOTAD to substitute the electrolyte, results in a efficiency as high as 9.7% (Kim et al., 2012). Since then, PSCs has received a series of fundamental scientific discoveries and breakthroughs in solar-to-electricity conversion efficiency (Figure 1.6).

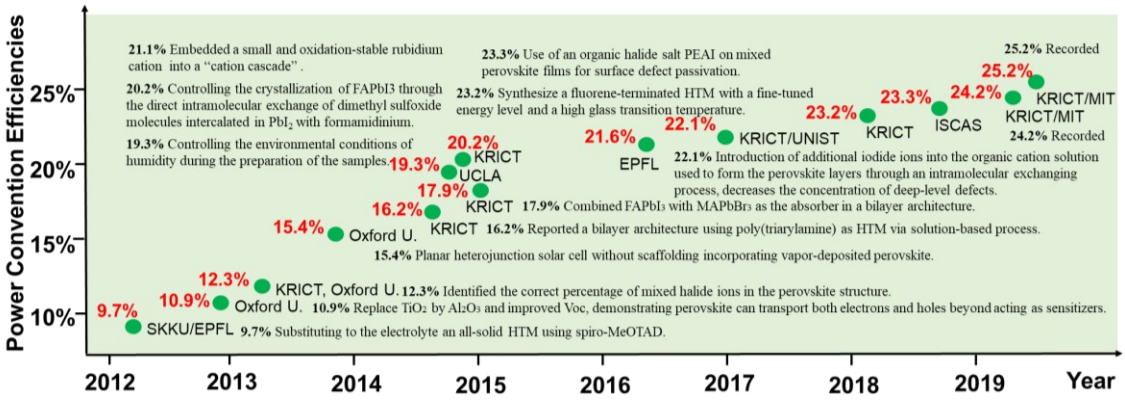

Figure 1.6 Photoelectric efficiency statistics diagram of PSCs.

Another breakthrough was proposed in 2012 when TiO_2 was replaced by an inert mesoporous Al_2O_3 layer, results in an improved V_{oc} and high efficiency to 10.9% (Lee, Teuscher, Miyasaka, Murakami, & Snaith, 2012), demonstrating perovskite can not only act as sensitizer but also transport carriers. The next year, in 2013, the recorded PCE was improved to 12.3% by identifing the correct percentage of mixed halide ions in perovskite structure (Noh, Im, Heo, Mandal, & Seok, 2013). Again in 2013, vapor deposition perovskite as absorption layer was proposed and results in 15.4% efficiency (Liu, Johnston, & Snaith, 2013). In 2014, a bilayer architecture using poly(triarylamine) as HTL via solution-based process was reported with 16.2% efficiency (Jeon et al., 2014). Following, the efficiency has been increased to 17.9% and 19.3% by combined $MAPbBr_3$ with $FAPbI_3$ as the absorber and controlled the environmental conditions of humidity during

preparation, respectively (Im, Jang, Pellet, Gratzel, & Park, 2014) (H. Zhou et al., 2014). In 2015, $FAPbI_3$-based PSCs with PCE exceed 20% was proposed by controlling the crystallization of $FAPbI_3$ through intramolecular exchange process (Yang et al., 2015). This record was quickly surpassed by Saliba who embedded a small and oxidation-stable rubidium cation into a "cation cascade" and results in an attractive efficiency up to 21.6% (Saliba, et al., 2016a). In 2017, excessive iodide ions were proposed to passivate the deep-level defects and improved efficiency to 22.1% (Yang et al., 2017). It is exciting when the efficiency was improved up to 23.2% by the introduction of a fluorene-terminated HTM (Jeon et al., 2018). Immediately, an organic halide salt was introduced on mixed perovskite film for surface defect passivation by Institute of Semiconductors, Chinese Academy of Sciences (ISCAS) and promoted the efficiency to 23.7% (Jiang et al., 2019). In 2019, the efficiency reported by Korea Research Institute of Chemical Technology (KRICT) and Massachusetts Institute of Technology (MIT) was 24.2% (Figure 1.2). Now the record was detained by a team from KRICT and MIT with a verified efficiency of 25.2% (Figure 1.2) (Nasti & Abate, 2019).

1.3.3 Construction of PSCs

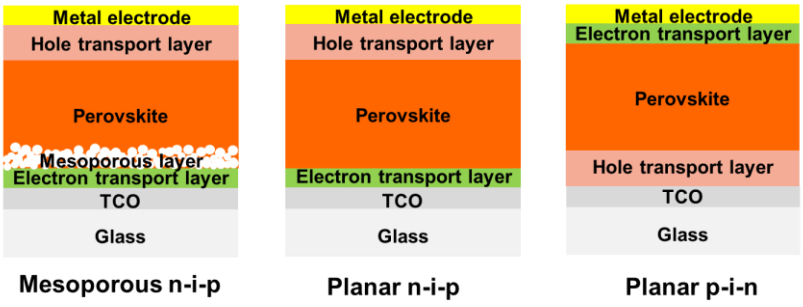

Figure 1.7 Common perovskite solar cell architectures of PSCs.

PSCs emerged in mesoporous or planar structure has recently attracted extensive interests with deepening research. When compared with mesoporous PSCs, planar PSCs

is more convenient along with reduced cost, simplified preparation process, and expanded application scope. All common structures as shown in Figure 1.7 show a layered structure includes glass with transparent conductive oxide, an n-type semiconductor as ETL, perovskite as light absorption layer and a p-type semiconductor as HTL, and metal as electrode (Rong et al., 2018). Mesoscopic PSCs developed after the investigation of DSSC where perovskite absorber was sensitized by mesoporous metal oxide (Yao et al., 2017). Due to the complexity prepare process of mesoporous structure, planar PSCs emerging in time. Although the perovskite absorption layer is deposited between ETL and HTL (Jiang et al., 2017; Arora et al., 2017), it should be noted that the preparation of planar n-i-p PSCs is not simple reversal planar p-i-n PSCs, appropriate ETL and HTL should be considered.

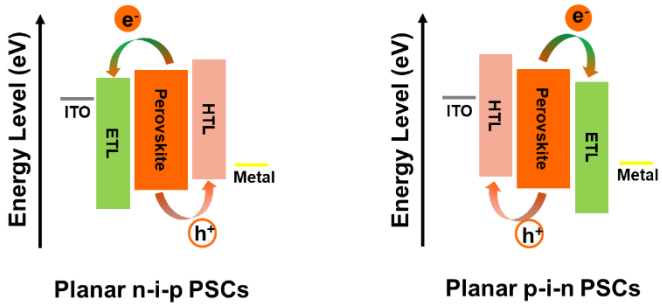

Figure 1.8 Working principle diagram of planar PSCs.

Working principle of planar PSCs is based on photovoltaic effect (as shown in 1.2.2) and the core idea is the separation and transport of carriers. Figure 1.8 shows the schematic diagrams of planar PSCs. When light irradiates on PSCs, bipolar perovskite absorbs photons and produces the electron-hole pairs. With the smaller exciton binding energy and larger dielectric constant of perovskite itself, the carriers can be dissociated easily. Then, excited electrons are injected to the conduction band of ETL and following collected by the negative electrode. Meanwhile, excited holes are transfer to the valence band of HTL and collected by the positive electrode. In the last, the potential difference is formed

between the positive and negative electrode. If they are connected by a load, there will be a closing current. At the same time, the load of the external circuit will work (Marchioro et al., 2014).

Noteworthy, ETL and HTL governs the subsequent important processes, including carriers transfer, recombination, and collection. Herein, some considerations should be taken for ETL and HTL, such as proper energy levels which advantageous to the extraction of carriers, wide bandgaps which minimize undesired absorption, high carriers mobility which decrease charge transport losses, low defect state density which eliminate nonradiative recombination. Thus, the optimization of transport layers is in favor of high efficiency and stable PSCs.

1.3.4 Preparation of PSCs

1.3.4.1 ETL of PSCs

In PSCs, two kinds of ETL are consisted: the dense layer and the mesoporous layer, which are used to transport electrons and block holes. Currently, numerous metal oxides such as TiO_2 (Jeon et al., 2014), SnO_2 (Jiang et al., 2017), ZnO (Kumar et al., 2013), Zn_2SnO_4 (Bera et al., 2015), WO_3 (Zhang, Shi, Chen, Wang, & Li, 2016), In_2O_3 (Qin et al., 2016), $SrTiO_3$ (Bera et al., 2014), Nb_2O_5 (Kogo, Numata, Ikegami, & Miyasaka, 2015) and CeO_x (Wang et al., 2017) have been used as ETL, and TiO_2 is the most used ETL among them (Duan et al., 2017; Shahiduzzaman et al., 2018; Xiong et al., 2018). However, the inefficient charge transfer and charge barrier at TiO_2/perovskite interface are averse to final device performance (Jiang, Zhang, & You, 2018). For efficient PSCs, ETL should satisfy these following condition: high transmittance for efficient optical energy absorption, high electron mobility for efficient electron transport, suitable energy levels for efficient charge transfer, easily processing and high stability (Chueh, Li, & Jen, 2015;

Pathak et al., 2014; Sun, Deng, Qiu, Fang, & Peng, 2015). Recently, SnO_2 was demonstrated as effective ETL in planar n-i-p PSCs due to its high transparency in visible light, suitable energy level, superior charge collection ability and high conductivity without high temperature process (Yang, Qin, Fang, & Li, 2018).

1.3.4.2 Absorption layer of PSCs

Perovskite absorption layer is an important part in PSCs. The photoelectric properties of PSCs are dependent on perovskite's quality and morphology directly (Dunlap-Shohl, Zhou, Padture, & Mitzi, 2019). Therefore, the perovskite optimization is also a key to improve PCE. Based on previous work, addition of additives, composition adjusting of precursors, modification on surface and deposition methods can affect the crystallization behavior of perovskite effectively (Prochowicz et al., 2019; Zhang, Nazeeruddin, & Choy, 2019). Meanwhile, the preparation process of perovskite is much more diversified. For example, chemical bath, doctor blade, spin-coating, metering rod, dip-coating, spray-coating, slot-casting, inkjet printing, aerosol jet and screen printing, as shown in Figure 1.9 (Pasquarelli, Ginley, & O'Hayre, 2011). Spin coating is outstanding among them because of its simple preparation process and high efficiency.

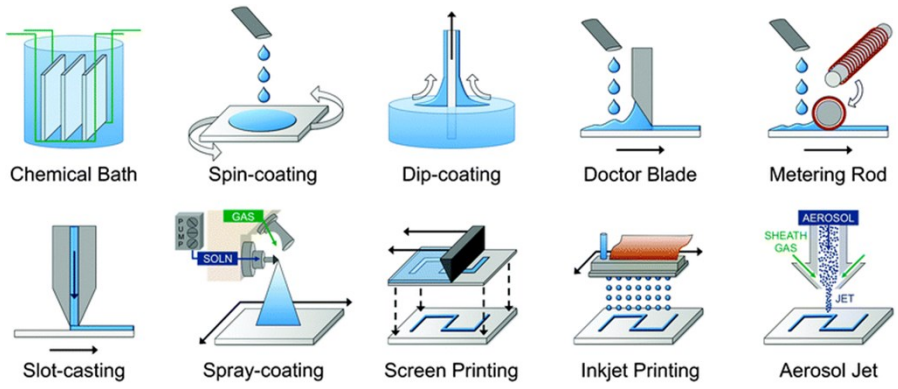

Figure 1.9 Preparation methods of perovskite thin films (Pasquarelli et al., 2011).

Spin coating has been classified to two categories (named one-step and two-step spin

coating) according to operation steps. One-step method is to mix all the precursors in a suitable solvent and deposit them by only just one operation step onto the substrate (Xiao et al., 2014; Xu, Zhang, Li, & Zhao, 2017). The nucleation and growth of perovskite crystal will be occurrence during the volatilization of solvents. One step method is a widely used method because of its fast reaction speed and simple preparation process. The two-step spin coating method also called continuous deposition method where the perovskite film is obtained by successive deposition of precursors.

1.3.4.3 HTL of PSCs

In PSCs, HTL is used to transfer holes to electrode and block electron transmission effectively, the quenching caused by the direct contact between perovskite and metal electrode can be avoided when HTL is introduced (Liu et al., 2019). In planar n-i-p PSCs, common HTMs include organic molecules (Such as Spiro-OMeTAD and PTAA), polymers (Such as P3HT) and inorganic crystals (such as CuI (Christians, Fung, & Kamat, 2014) and CuSCN (Ito et al., 2014)), and Spiro-OMeTAD is the commonly used material among them (Li, Meng, & Zhang, 2018).

Spiro-OMeTAD, the currently popular HTL in planar n-i-p PSCs, still suffers from severe instability due to the incorporation of necessary dopants named lithium bis(trifluoromethanesulfonyl)imide (Li-TFSI), which is highly sensitive to moisture, heat and even light (Liu et al., 2019). In addition, low hole mobility in the pristine state and high synthesis costs of Spiro-OMeTAD also unavoidably impede its industrialization. Therefore, the exploration of efficient dopant-free HTMs with low synthesis costs, good reproducibility and high stability seems imperative for the rapid evolution of planar n-i-p PSCs. But most reports for novel materials are results in lower performances compared to

Spiro-OMeTAD till now.

1.4 Existing problems and research hotspots of PSCs

Although the development of PSCs is rapidly with huge improvements in PCE which is comparable to silicon photovoltaic, there are still some problems in the commercialization of this photovoltaic technology. The mainly considerations mainly focus on the following aspects: high efficiency which is the main motivation of PSCs research, stability which is the main deficiency of PSCs research, scalable area which is the main obstruct of PSCs research and toxicity which is the disadvantage of PSCs research.

1.4.1 Main motivation of PSCs research-high efficiency

PSCs is a fast develop field. It has aroused great interests in the investigation on different layers (such as ETL, absorption layer, HTL) and results in a rapid progress in PCE. The increased PCE of PSCs are mainly achieved by optimizing ETL, interface optimization between absorbed layer and transport layer, perovskite composition optimization and perovskite layer modification.

1.4.1.1 Optimization of ETL

ETL is an important part in PSCs. Majority reported works on the optimization of ETL are focus on designing new ETL, proposing new preparation method and surface modification of ETL to make an improvement in efficiency. For example, a new ETL named cascade ZnO-ZnS has been proposed by Chen who convert surface ZnO into ZnS, created a novel pathway for electron transport, yielding in improved efficiency and stability (Chen et al., 2019). Tin acetylacetonate based ETLs have been explored by Abuhelaiqa who investigated device performance with non-colloidal SnO_2 precursors, their results show that the residue halide in films improving the thermal durability of SnO_2

film and providing a passivation layer, results in an unprecedented PCE of 22.19% (Abuhelaiqa et al., 2019). And Yang has reported a room-temperature colloidal synthesis method to control the carrier concentration of SnO_2 quantum dot and achieved a high PCE of 20.26% (Yang et al., 2018). N_2 plasma treated SnO_2 was introduced and resulted in a PCE of 20.3% (Subbiah, Mathews, Mhaisalkar, & Sarkar, 2018). And EDTA-complexed SnO_2 was proposed by Yang who improved the band energy level matching degree between ETL and perovskite, leading to a high PCE (21.60%) (Yang et al., 2018). Based on these, the optimization of ETL is a feasible way to achieve high efficiency PSCs.

1.4.1.2 Interface optimization between transport layer and absorption layer

Interface optimization, an effective and critical way to improve carriers transport and suppress carriers recombination, which improved final efficiency and attracted attentions from researchers (Deng, Liang, Kubiak, & Cameron, 2018; Ma et al., 2010). For example, SnO_2 thin films deal with atmospheric Ar/O_2 plasma energy has been proposed for the interface modification and yielded a more even surface with lower charge trap density, results in a superior PCE to 19.56% (Yu et al., 2018). And Cs_4SnO_4 was used as a modification layer to suppress interface defects and decrease band misalignment, results in an improved PCE to 19.23% (Zhao et al., 2018). At the same time, terminal functional groups molecules formed dipoles on the interface results in a passivation at the trap states via hydrogen bonding and an reduced charge recombination at interface effectively (Zuo et al., 2017).

1.4.1.3 Composition optimization of perovskite

Perovskite which containing a mixture of A-site cations such as FA or cesium (Cs^+) cations, has aroused considerable interest because of its improved stability and performance. Perovskite with a mixed cation combination of MA, FA and Cs has achieved

a high PCE to 21.2% (Saliba, Matsui, Seo, et al., 2016). Following, Rb^{+} was introduced and results in 21.6% PCE by Saliba (Saliba et al., 2016). B-site was also partially substituted by hetero-valent neodymium cation and results in superior film quality with low trap-state density, dramatically enhanced carrier mobility, and make an improvement in PCE (21.15%) (Wang et al., 2019).

1.4.1.4 Modification of perovskite layer

In absorption layer, gradient hetero-structure is beneficial to the transfer of carriers (Qiao et al., 2019). For example, perovskite-fullerene graded heterojunction was reported to suppress the photoelectron back-flow and achieved an impressive PCE of 18.21% (Wu et al., 2016). Sb^{3+} and In^{3+} with mismatched cation sizes created heteroatoms have also been introduced into the perovskite film spontaneously and results in an increased PCE to 21.04% (Qiao et al., 2019). The addition of additives into precursor solution is another valid approach to improve the PCE which could suppress the grain surface dominated charge recombination. For example, 2-mercaptopyridine was introduced and lead the PCE increased from 18.35% to 20.28% (Zhang et al., 2019). Molecules with passivation groups (such as carboxyl, isopropyl, amine, phenethyl, and tert-butylphenethyl groups) have been proposed for the modification of perovskite too. The results show that amine, carboxyl groups and aromatic could decrease trap density and yield a stabilized efficiency of 21.4% (Yang et al., 2019). Recently, an organic halide salt phenethylammonium iodide has been deposited on perovskite film for surface defect passivation and results in an attractive PCE up to 23.32% (Jiang et al., 2019).

1.4.2 Main deficiency of PSCs research-stability

Stability is another important problem for PSCs (Ye, Hong, Zhang, & Liu, 2016), the influences of illumination, high temperature, and ambient exposure are necessary to be

considered (Djurišić et al., 2017). There are several strategies that have been verified to improve stability, mainly include the alteration of perovskite itself, optimization of perovskite deposition, optimization of HTL and so forth.

1.4.2.1 Alteration of perovskite itself

Since perovskite along with relatively poor stability, the alteration of perovskite itself is an effective strategy to improve intrinsic stability. For example, compared to $MAPbI_3$, $MAPbBr_3$ is much more stable (Kim, Seo, & Park, 2016). Mixed cation perovskites also show improved stability (Mei et al., 2014). Moreover, alkali metal such as Rb^+ (Kim, Williams, Cho, Chueh, & Jen, 2015) or Cs^+ incorporation (Niemann et al., 2016) replace organic cation is also successful to improve stability. Simultaneously, 2D perovskite also shows better stability compared to 3D perovskites (Smith, Hoke, Solis-Ibarra, McGehee, & Karunadasa, 2014; Tsai et al., 2016).

1.4.2.2 Optimization of perovskite deposition

The crystallinity of perovskite is found to be an important factor for the stability of perovskite and PSCs (Kim et al., 2015). Therefore, perovskite films deposition is critical important. And the optimization of perovskite deposition is another effective way to achieve PSCs with high stability. For instance, solvent engineering was stand out as an valid method to improve stability of perovskite (Li et al., 2016). At the same time, the addition of phosphonic acid ammonium was also results in improved moisture resistance by crosslinking the neighbor grains (Li et al., 2015). Addition of additives was also proposed to improve quality and enhance stability (Sun et al., 2017).

1.4.2.3 Optimization of HTL

In planar n-i-p PSCs, it is imperative to explore novel HTMs as reliable alternatives for Spiro-OMeTAD which is suffers from unstable device operation (Liu et al., 2019).

Therefore, the exploration of efficient dopant-free HTMs with high stability, low-cost synthesis and good repeatability is another way to improve stability. As such, an improved stability in dopant-free PSCs by changing a flexible triphenylamine unit to a rigid quinolizino acridine core in star-shaped molecules was achieved in 2017 (Paek et al., 2017). At the same time, they revealed that by varying π-bridge in star-shaped molecules from monothiophene unit to terthienyl groups, highly ordered face-on orientation could be realized and significantly increased the stability (Rakstys et al., 2017). Alternatively, modulating periphery groups was established as a new strategy by Liu who has also reported an increased stability by using a more twisted Spiro[fluorene-9,9'-xanthene] group (Liu et al., 2019).

1.4.3 Main obstruct of PSCs research-scalable area

Fabricating high-quality and large-area perovskite film based on simple method is an essential condition for its commercializing (Abate, Correa-Baena, Saliba, Su'ait, & Bella, 2018). Remarkable progress has been achieved towards large-scale PSCs manufacturing in the past few years. For example, a simple vacuum flash-assisted method has been proposed in the deposition of perovskite and the resulting devices with area exceed 1 cm^2 shows high PCE up to 20.5% (Li et al., 2016). Based on the optimized blade coating process, Razza obtained 10 mm^2 solar cells with 13.3% PCE, with the series connection of modules, results in 10.4% and 4.3% PCE for a 10.1 cm^2 and 100 cm^2 active area, respectively (Razza et al., 2015). Another outstanding result is original from 2017, when 12.1% certified efficiency was achieved with 36.1 cm^2 aperture area (Chen et al., 2017).

1.4.4 Main disadvantage of PSCs research-toxicity

Environmental pollution is also a well serious problem for the application of PSCs (Babayigit, Ethirajan, Muller, & Conings, 2016). Lead is a well-known toxic metal, has

caused numerous cases of environmental contamination and health problems to humans (Havelaar et al., 2015). Therefore, the introduction of heavy metals (usually Pb) in perovskite precursor may be a main problem. To address this problem, considerable attentions are put into the exploitation for lead-free perovskite materials. Except tin-based perovskite, numbers of other materials have also been reported in recent years, such as $FAGeI_3$ (Krishnamoorthy et al., 2015), $MA_2CuCl_xBr_{4-x}$ (Cortecchia et al., 2016), $A_3Sb_2I_9$ (Harikesh et al., 2016), $MA_3Bi_2X_9$ and $Cs_3Bi_2X_9$ (Park et al., 2015; Singh, Kulkarni, Ikegami, & Miyasaka, 2016). Unfortunately, the achieved PCE base on these new perovskites are below 1%. Compared with these materials, tin-based perovskites generally show higher PCE, but still below that of lead-based PSCs. In 2012, the first tin-based PSCs was reported where a consecutive layer of CsI and $SnCl_2$ on ITO substrate with ITO/$CsSnI_3$/Au/Ti configuration (Chen, Wang, Ren, Yu, & Shum, 2012). The first promising results with tin PSCs emerge in 2014, 5.73% and 6.4% PCE have been obtained based on $MASnI_3$ perovskites by Green (Green et al., 2014) and Noel (Noel et al., 2014) respectively. In 2017, with the mix of FA and MA, Zhao (Zhao et al., 2017) promoted the PCE up to 8.12%. Recently, a PCE up to 9.41% has been achieved with a hierarchical 2D-quasi-2D-3D structure in the $FASnI_3$ PSC (Wang et al., 2018).

1.5 Topic significance and research content

PSCs has emerged as promising photovoltaic device and witnessed rapidly rising PCE, together with obvious advances in stability. With the simple preparation process compared to mesoscopic PSCs and high PCE to planar p-i-n PSCs, planar n-i-p PSCs has been proposed for our following research. Due to the huge charge accumulation original from the TiO_2/perovskite charge barrier and the high preparation temperature, much more attentions have been attracted by SnO_2 (Xiong, Guo, et al., 2018). At the same time, as

mixed cations perovskite absorption layer results in high efficiency and stability, the absorption layer is fixed as $Cs_{0.05}(FA_{0.87}MA_{0.13})_{0.95}Pb(I_{0.87}Br_{0.13})_3$(CsFAMA). We focus on the optimization of SnO_2 transport layer to obtain planar n-i-p PSCs with high PCE and improved stability. Beyond these, because of the commonly used HTL named Spiro-MeOTAD suffers from high-cost preparation, low mobility and the addition of moisture-sensitive dopants, we are also try to optimize the HTL by replace it with some dopant free molecules and maintained the PCE at the same time.

1.5.1 Optimization of SnO_2 transport layer by molecular doping

When an organic molecule is adsorbed on the surface of inorganic nanocrystals, charge transfer from the organic molecule to the inorganic semiconductor can occur without inducing defects within the inorganic semiconductor. To improve the PCE based on SnO_2 ETL, we try to dope SnO_2 itself, which could result in faster electron extraction and higher charge carrier concentration. Based on these, PSCs based on SnO_2 and triphenylphosphine oxide (TPPO) doped SnO_2 have been fabricated with the basic configuration of "ITO/SnO_2(-TPPO)/CsFAMA/Spiro-MeOTAD/Au". The photovoltaic parameters and the related results have been characterized comprehensively.

1.5.2 Optimization of SnO_2 transport layer by defect passivation

As n-type contact heterojunction (ETL/perovskite) plays a critical role in suppressing the interfacial recombination and reducing charge accumulation, we try to optimize the SnO_2 transport layer by passivate the defects at SnO_2 itself and interface between SnO_2 and perovskite. Based on these, the PSCs based a basic configuration of "ITO/SnO_2/CsFAMA/Spiro-MeOTAD/Au" with or without optimization have been fabricated. The photovoltaic parameters and the related results have been characterized comprehensively.

1.5.3 Optimization of HTL by introduce dopant free HTMs

Due to instability of Spiro-MeOTAD with dopants which is highly sensitive to moisture, heat and even light, the development of stable dopant-free HTMs is imperative. Hence, different dopant free molecules have been synthesized and used as HTL in PSCs with a basic configuration of "ITO/SnO_2/CsFAMA/dopant free HTM (Spiro-MeOTAD)/Au". At the same time, the effect of alkyl chains length is also considered. Native photophysical and electrochemical properties, mobility, PCE and stability have been characterized comprehensively.

1.6 Published papers

1. **B. Tu**, Y. F. Shao, W. Chen, Y. H. Wu, X. Li, Y. L. He, J. X. Li, F. Z. Liu, Z. Zhang, Y. Lin, X. Q. Lan, L. M. Xu, X. Q. Shi, A. M. C. Ng, H.-F. Li,* L.W. Chung, A. B. Djurišic´, Z. B. He,* "Novel molecular doping mechanism for n-doping of SnO2 via triphenylphosphine oxide and its effect on perovskite solar cells", ***Adv. Mater***. 2019, 31, 1805944.
2. **B. Tu**, Y. Wang, W. Chen, B. Liu, X. Feng, Y. Zhu, K. Yang, Z. Zhang, Y. Shi, X. Guo,* H.-F. Li,* Z. Tang, A. B. Djurišić, Z. B. He,* "Side-chain engineering of donor-acceptor conjugated small molecules as dopant-free hole-transport materials for efficient normal planar perovskite solar cells", ***ACS Appl. Mater. Inter***. 2019, 11, 51, 48556-48563.
3. **B. Tu**, et al. "In-situ modified SnO_2 electron transport layer for defect passivation in normal planar perovskite solar cells". (to be submitted)
4. Y. Zhu, S. Wu, **B. Tu**, S. Jin, A. Huq, J. Persson, H. Gao, De. Ouyang, Z. He, D.-X. Yao, Z. Tang, H.-F. Li,* "High-temperature magnetism and crystallography of a YCrO3 single crystal", ***Phys. Rev. B*** 2020, 101, 01411.

5. Y. Zhu, **B. Tu**, S. Wu, J. Xia, P. Zhou, A. Huq, W. Schmidt, Z. Tang,* Z. He,* H.-F. Li,* "Crystalline and magnetic structures, magnetization, heat capacity and anisotropic and negative thermal expansion in a yttrium-chromium oxide", under review.
6. Y. Wang, W. Chen, L. Wang, **B. Tu**, T. Chen, B. Liu, K. Yang, C. W. Koh, X.H. Zhang, H. L. Sun, G. C. Chen, X. Y. Feng, H. Y. Woo, A. B. Djurišić,* Z. B. He,* X. Guo* "Dopant-free small molecule hole-transporting material for inverted perovskite solar cells with efficiency exceeding 21%", ***Adv. Mater.*** 2019, 31, 1902781.
7. D. D. Zhao, Y. H. Wu, **B. Tu**, G. C. Xing, H. F. Li, Z. B. He,* "Understanding the impact of Cu-In-Ga-S nanoparticles compactness on holes transfer of perovskite solar cells", ***Nanomater.***, 2019, 9, 286.
8. W. Chen, Y. C. Zhou, G. C. Chen, Y. H. Wu, **B. Tu**, F. Z Liu, L. Huang, A. M. C. Ng, A. B. Djurišić,* and Z. B. He*, "Alkali chlorides for the suppression of the interfacial recombination in inverted planar perovskite solar cells", ***Adv. Energy Mater.***, 2019, 9, 1803872.
9. Y. H. Wu, W. Chen, Y. Lin, **B. Tu**, X. Q. Lan, Z. G. Wu, R. C. Liu,* A. B. Djurišić, and Z. B. He*, "General method to define the type of carrier transport materials for perovskite solar cells via kelvin probes microscopy", ***ACS Appl. Energy Mater.***, 2018, 1, 3984−3991.
10. W. Chen, Y. F. Wang, G. T. Pang, C. W. Koh, A. B. Djurišić,* Y. H. Wu, **B. Tu**, F. Z. Liu, R. Chen, H.Y. Woo, X. G. Guo,* Z. B. He*, "Conjugated polymer-assisted grain boundary passivation for efficient inverted planar perovskite solar cells", ***Adv. Funct. Mater.*** 2019, 29, 1808855.
11. W. Chen, Y. H. Wu, **B. Tu**, F. Z. Liu, A. B. Djurišić,* Z. B. He,* "Inverted planar

organic-inorganic hybrid perovskite solar cells with NiO_X hole-transport layers as light-in window", ***Appl. Surf. Sci.***, 2018, 451, 325-332.

12. W. Chen, Y. C. Zhou, L. J. Wang, Y. H. Wu, **B. Tu**, B. B. Yu, F. Z. Liu, H. W. Tam, G. Wang, A. B. Djurišić,* L. Huang,* Z. B. He*, "Molecular doped nickel oxide: verified charge transfer and high efficient planar inverted mixed cations perovskite solar cell", ***Adv. Mater.*** 2018, 30, 1800515.
13. Y. Li, F. Z. Liu, M. Waqas, T. Leung, H. W. Tam, X. Q. Lan, **B. Tu**, W. Chen, A. B. Djurišić, W. Chan and Z. B. He,* "Formamidinium-based lead halide perovskites: structure, properties, and fabrication methodologies", ***Small Methods***, 2018, 2, 170038.

2. Optimization of SnO_2 transport layer by molecular doping

2.1 Introduction

Doping is a general way to modulate the electronic structure of materials to improve their based device performance. Ionic doping is widely used in inorganic semiconductors to increase conductivity by increasing the carrier density of majority carriers. However, this process can result in increased disorder and defects in the crystal lattice, resulting in the degradation of carrier mobility and parasitic recombination. Ideally, a doped semiconductor should have both high conductivity and high charge carrier mobility. Different doping strategies have been used in organic materials, which typically contain large molecules and can have amorphous structure or small grain size and large number of imperfections or impurities compared to epitaxially grown inorganic semiconductors (Lussem et al., 2016). In contrast with inorganic material doping where dopant acts as a point defect in the crystal lattice, in organic molecules two processes can occur: formation of host and dopant ion pairs, then the formation of ground state charge transfer complexes (Mendez et al., 2015; Salzmann, Heimel, Oehzelt, Winkler, & Koch, 2016). While the organic systems offer excellent tunability by varying the chemical structure of host and dopant molecules, the doping efficiency needs to be improved.

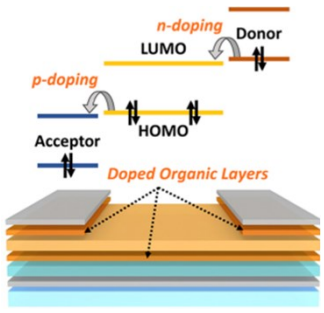

Figure 2.1 Simplified schematic diagram of organic doping process (Lussem et al., 2016).

One possible strategy to address the different problems existing in doped inorganic and organic materials is to develop hybrid organic-inorganic systems which would combine the advantages of both types from materials. As shown in Figure 2.1, when an organic molecule is adsorbed on the surface of inorganic nanocrystals, charge transfer from the organic molecule to the inorganic semiconductor can occur, without inducing defects within the inorganic semiconductor. Consequently, this approach was successfully applied to the surface doping of some inorganic nanocrystals by organic molecules in recent years (Kim et al., 2018; Kirmani et al., 2016; Martinez et al., 2015; Rietwyk et al., 2014; Schiessl et al., 2016; Schlesinger et al., 2015; Schultz, Niederhausen, Schlesinger, Sadofev, & Koch, 2018). In 2014, Rietwyk reported firstly this novel doping mechanism of electrons transferring from the absorbed molecular donor (methylcoboltocene) to the silicon surface (Rietwyk et al., 2014). Tarasov employed air stable dihydrobenzimidazole derivatives (2-Fc-DMBI-H) and benzimidazoline radicals ($(2\text{-Fc-DMBI})_2$) to obtain effective n-type doping of MoS_2 few-layer nanosheets (Tarasov et al., 2015). Kirmani successfully realized the electronic structure modulation of PbS quantum dots via molecular doping of some p and n type metal-organic chelates dopants (Kirmani et al., 2016). The new doping method has shown increasing impact on the academic research community of optoelectronics and energy (Schlesinger et al., 2015; Schultz et al., 2018). Thus, we aim to doping the inorganic metal oxide during the fabrication of PSCs.

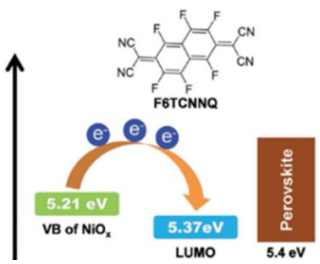

Figure 2.2 Organic molecular doping of NiOx (Chen et al., 2018).

More recently, our group demonstrated a successful surface molecular doping of NiO nanoscrystals by small molecule for high performance PSCs, where it is verified by multi-photophysical tools of electrons transfer from already p-type NiO nanocrystals film to F6TCNNQ due to stronger electron capture ability of fluorine atoms in the air stable F6TCNNQ molecules compared to the oxygen atoms in NiO nanocrystals (Chen et al., 2018). This results in higher hole concentration without detrimental effects on the NiO nanocrystals film, which improves the performance of PSCs. This good result moves us further to strengthen electronic properties of SnO_2 nanocrystals film by surface molecular doping, which acts already as another promising material for electron transport in PSCs (Jiang et al., 2017; Ke et al., 2015; Seok, Grätzel, & Park, 2018). However, compared with p-type molecular doping, successful n-type doping of inorganic semiconductors is more difficult (Kirmani et al., 2016; Schlesinger et al., 2015; Tarasov et al., 2015). So far, only some limited kinds of expensive, unstable and complex chelate molecules were involved as electron donors for n-type molecular doping of inorganic semiconductors.(Kim et al., 2018; Rietwyk et al., 2014; Schiessl et al., 2016) This problem is mainly due to the scarcity of molecules which exhibit strong reducibility along with stability simultaneously. Moreover, robust molecular structure as well as cost-effectiveness are also requirements in the evolution of this promising technique.

On the other hand, various surface modification of SnO_2 were successfully employed to enhance electrons transfer at the cathode side and hence to improve the device performances (Choi et al., 2018; Ke et al., 2016; Li et al., 2015; Liu et al., 2016; Rao et al., 2015; Wang et al., 2016; Wu, Chen, Cheng, & Caruso, 2017; Xie et al., 2017). The enhancements were mainly attributed to the surface trap states passivation of SnO_2 film and antisite defects of perovskites, dipole effect and band level alignment adjustments.

Therefore, organic doping of SnO_2 is another effectively way to improve the SnO_2 film quality and passivate the trap states in PSCs which could results in an improved PCE. In this work, a simple, air-robust and cheap electron donor, TPPO, was adopted to realize n-type doping of SnO_2.

2.2 Experimental section

2.2.1 Materials

Lead (II) bromide ($PbBr_2$) and Lead (II) iodide (PbI_2) were obtained from Tokyo Chemical Industry (TCI). Acetonitrile (ACN), N,N-dimethylformamide (DMF), DMSO, chlorobenzene(CB), isopropanol (IPA), Li-TFSI, TPPO, Cesium iodide (CsI) and tert-butylpyridine (tBP) were obtained from Sigma-Aldrich. Formamidinium Iodide (FAI) and Methylammonium bromide (MABr) were purchased from GreatCell Solar Ltd (Australia). tris(2-(1H-pyrazol-1-yl)-4-tertbutylpyridine)-cobalt(III) tris(bis(trifluoromethylsulfonyl)imide) (FK209), Li-TFSI and Spiro-OMeTAD were obtained from Xi'an Polymer Light Technology Corp. The SnO_2 colloid precursor (tin(IV) oxide, 15% in H_2O colloidal dispersion) was obtained from Alfa Aesar.

2.2.2 Preparation of pristine and doped SnO_2 films

Diluted SnO_2 colloid precursor with H_2O to 2.67% before use. Spin coating (3500 r.p.m., 30s) this diluted precursor and annealed at 180 ˚C for the formation of SnO_2 films. Various concentrations (from 0.25 to 1.5 mg/mL) of TPPO (dissolved in ACN) was loaded and spin coated, following annealed at 100 ˚C. CB was introduced to wash the remained molecule before spin coating of the perovskite.

2.2.3 Planar n-i-p PSCs preparation

Firstly, ITO was cleaned with detergent, deionized water, ACN and IPA, sequentially. Then, deal with UVO for 15 minutes. Following, spin coating the pristine and TPPO

doped SnO_2. After depositing the ETL, the perovskite layer was deposited through anti-solvent assisted one-step procedure. Here, perovskite precursor was achieved by mixing MABr, FAI, $PbBr_2$ and PbI_2 in DMF/DMSO (volume ratio is 4:1) with the mole ratio of FA/MA and I/Br maintained at 0.87/0.13, and the mole concentration of PbI_2 kept at 1.1 M. After stirring for 1 hour at 60 ˚C, 35 µL of CsI (2 M dissolved in DMSO) was injected and stirred for another 1 hour. Spin coating (2000, 10s and 6000, 20s) the precursor solution and antisolvent (100 µL CB) was dropped 10 s prior to the end. After perovskite growth, Spiro-OMeTAD/CB (72.3 $mg \cdot mL^{-1}$) solution with tBP (28.5 µL), Li-TFSI/ACN (17.8 µL, 520 $mg \cdot mL^{-1}$) and FK209/ACN (30µL, 300 $mg \cdot mL^{-1}$) was spin coated (4,000 r.p.m., 30 s). At last, Au was deposited by thermal evaporation method.

2.2.4 Characterization

AFM-based characterizations were realized with Atomic Force Microscope (AFM) (MFP-3D-BIO, Asylum Research, USA) under atmospheric conditions (26 ˚C and 39% RH). Silicon tips coated Ti/Ir (ASYELELC-01-R2, k ~ 1.4-5.8 N/m, f ~ 58-97 KHz) were employed in Electrostatic Force Microscopy (EFM) and Scanning Kelvin Probe Microscopy (SKPM) imaging. Silicon tips coated with Pt/Ir (Econo-SCM-PIC, k ~ 0.4-0.7 N/m, f ~ 9-17 KHz) were utilized in Conductivity Atomic Force Microscope (c-AFM) imaging. X-ray Photoelectron Spectroscopy (XPS) and Ultraviolet Photoelectron Spectroscopy (UPS) measurements were performed on Thermo Fisher (ESCALAB 250Xi, Al Kα x-ray source, 10^{-9} mbar). XPS results were calibrated with C 1s. 10 V bias was applied in the UPS test with Au as reference. UV measurements were completed with UV/Vis/NIR Spectrometer (Perkin Elmer, Lambda 950). *J-V* measurements were performed in in ambient condition (27 ºC, 75% RH) with a Keithley 2400 sourcemete. Illumination was provided by solar simulator (Oriel Sol3A, AM1.5G spectrum, calibrated

by KG-5 Si diode). All devices were measured with 10 ms delay time. EQE results were carried out by Enli Tech (Taiwan). Morphology was achieved by Scanning Electron Microscope (TESCAN MIRA3), cross-section morphology, Energy Dispersive X-Ray Spectroscopy (EDX) mapping and Scanning Transmission Electron Microscopy (STEM) images were realized by Transmission Electron Microscopy (TEM, FEI Talos) and Focus Ion Beam (FIB, Helios Nanolab 600i). X-Ray Diffraction (XRD) patterns were achieved from X-ray Diffractometer (BRUKER ECO D8 series). Depth profiling data was received from Time-of-Flight Secondary Ions Mass Spectroscopy (ToF-SIMS). Photoluminescence (PL) and Time Resolution Photoluminescence (TRPL) spectrums were achieved with Spectrofluorometer (FS5, Edinburgh, 405 nm pulsed laser). Electrochemical Impedance Spectroscopy (EIS) were studied in ambient environment (26 ˚C, 39% RH) by electrochemical station (Zahner IM6e, Zahner, Germany).

2.2.5 Computational methods

Density Functional Theory (DFT) calculations were performed within the Perdew-Burke-Brinkerhoff parametrization of the generalized gradient approximation (PBE-GGA), as implemented in the Vienna ab initio simulation package (VASP) with 500 eV energy cutoff. Atomic coordinates and lattice parameters were optimized till the force less than 0.02 $eVÅ^{-1}$ for each atom. Van der Waals (VdW) interaction between TPPO molecule and SnO2 (110) surface was considered. 15 Å vacuum space in the vertical direction was used to separate each slab to avoid the inter-layer interaction.

2.3 Results and Discussion

2.3.1 EFM characterization of charge transfer

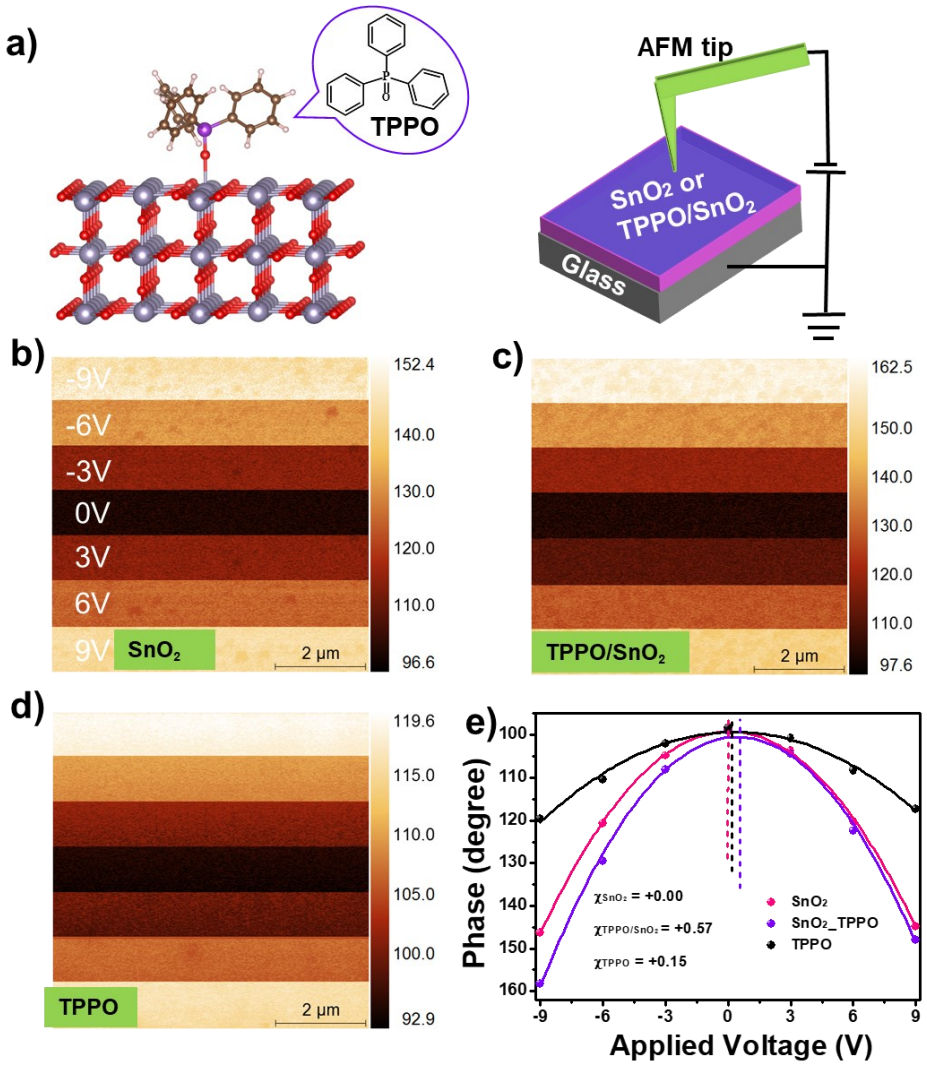

Figure 2.3 a) The relaxed model of a TPPO molecule absorbed on SnO_2 (110) surface and the EFM measurement. b-d) The phase images of bare SnO_2, TPPO doped SnO_2, and TPPO, respectively. e) The plots for phase as function of applied bis. The dash lines denote the symmetry axis of the fitting parabola while the solid lines denote the corresponding Gaussian fittings.

TPPO is a tetrahedral molecule with three benzenes rings at the three vertices in a plane and the oxygen atom at the other vertex (Spek, 1987). Expected molecule configuration of TPPO due to linkage between oxygen atoms of TPPO and tin atoms on SnO_2 surface was depicted as Figure 2.3a. We employed EFM to discover whether any charge transfer

occurs between the absorbed TPPO molecules and underlying SnO_2 nanocrystals film occurs. The testing scheme is illustrated in Figure 2.3a, where -9 to 9 V bias voltage with 3 V increment was applied to extract the Coulombic Force (Yalcin, Labastide, Sowle, & Barnes, 2011). Figure 2.3b-d compared the phase shift mapping results. It should be noted here that the size of SnO_2 nanocrystals involved in this work was 3-4 nm and the nanocrystals are dispersed in water (Jiang et al., 2017). To prepare the standard EFM samples, SnO_2, TPPO and TPPO/ SnO_2 were coated on glass.

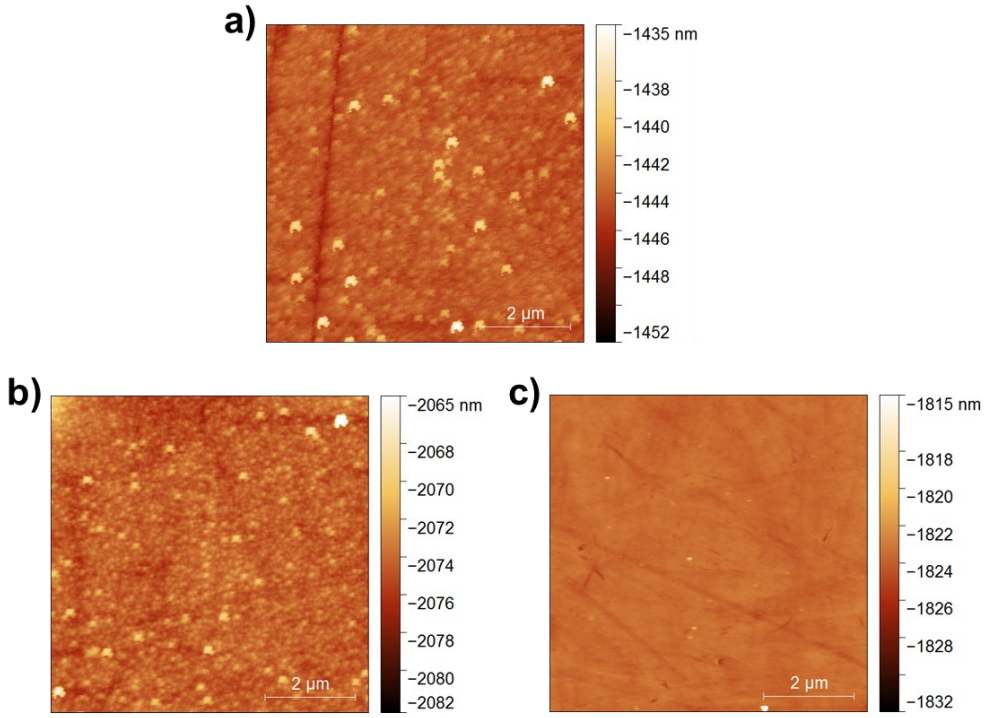

Figure 2.4 Topographic AFM images of SnO_2 (a), TPPO doped SnO_2 (b) and TPPO (c).

The topographic AFM images of the three EFM samples are shown in Figure 2.4. The SnO_2 nanocrystals show obvious grains morphology while the surface of TPPO-only sample shows too flat to be discerned. Correspondingly, the phase images in Figure 2.3b-d also show clear grains and grain boundaries owing to the high space resolution of our EFM results. The differences in the phase shift degree of the samples can be easily distinguished. Different from our former report (Chen et al., 2018), the positive shifts of

the symmetry axis of the fitting parabola in this work indicate positive charge induced at the sample surface (Figure 2.3e). The *x*-value of the symmetric axis listed inside are 0.00 V for SnO_2, 0.15 V for TPPO and 0.57 V for TPPO/SnO_2, respectively. They are proportional to surface charge density at the surface. For the bare SnO_2 0.00 V means hardly any charge induced. Turn to TPPO film, a small amount of positive charges was induced while their concentration of them was obviously augmented for the TPPO modified SnO_2 sample. This phenomenon moves us to learn in-depth about TPPO molecule itself and its interaction with SnO_2. Firstly, this interaction may be origin from the polarized singly σ-bond, R_3P^+-$O^-$of TPPO molecule (Bryce, Eichele, & Wasylishen, 2003; Chesnut, 1998; Dobado, Martínez-García, Molina, & Sundberg, 1998). Rationally, the polarized oxygen (O^-) atom with rich electrons is inclined to loss electrons to directly connected tin atoms at the surface, which leads to positively ionized TPPO molecules and hence accounts for the positive charges detected by EFM (Figure 2.3) (Yalcin et al., 2011).

2.3.2 DFT characterization of charge transfer

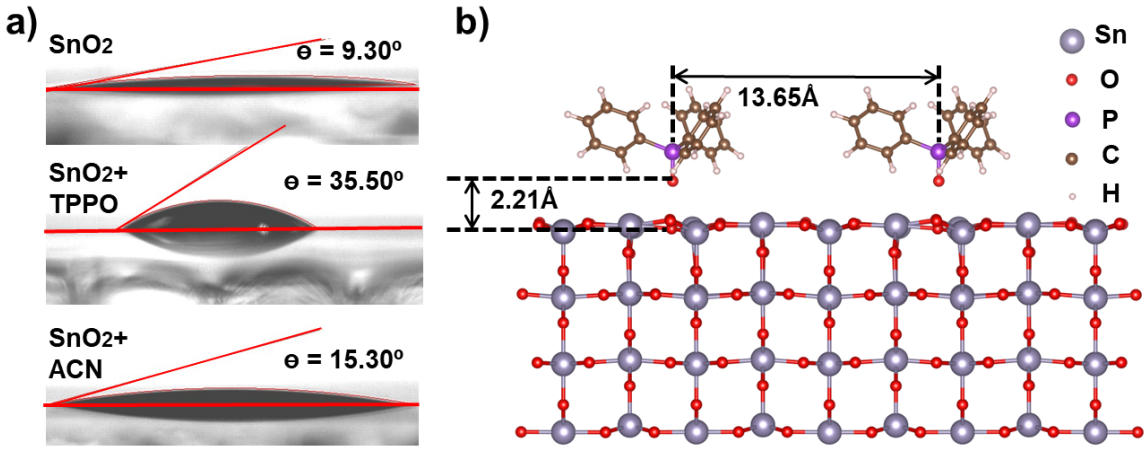

Figure 2.5 a) Surface contact angles of SnO_2, TPPO doped SnO_2 and SnO_2 treated with acetonitrile on ITO substrates. b) Side-view of the relaxed model of TPPO absorbed SnO_2 (110) surface. The different atoms are labeled in panel (b).

To confirm our speculation and gain insight into the experimental results, theoretical calculations were performed by using DFT. As mentioned above, the oxygen atom of TPPO molecule may connect with Sn atom of SnO_2 nanocrystals at the film surface, which leaves the other three ends of this tetrahedral molecule facing upward, which is tested by the contact angle measurement (Figure 2.5a). The contact angle increases obviously after coating a thin layer of TPPO on SnO_2 films. Based on this configuration, a TPPO molecule was put on a 4×2 (110) surface with lattice parameters of 12.97 Å ×13.65 Å (Figure 2.5b) (Batzill & Diebold, 2005). Several different adsorption configurations of TPPO molecule on SnO_2 (110) are considered. The adsorption energy is defined by $E_{ads} = E_{SnO_2+TPPO} - E_{SnO_2} - E_{TPPO}$, where E_{SnO_2+TPPO} is the last energy when TPPO adsorbed on SnO_2 (110) surface, E_{SnO_2} is the energy of SnO_2 (110) surface, and E_{TPPO} is the energy of TPPO molecule. The Van der Waals interactions are also considered. Negative adsorption energies indicate that TPPO molecule adsorbed on SnO_2 (110) surface are stable. According to the definition of E_{ads}, a more negative value of adsorption energy indicates stronger interactions between molecule and SnO_2 surface. The calculated adsorption energies are -1.44 eV for defect-free surface and -1.56 eV for surface with O vacancy. The optimal vertical interlayer-distance between molecule and surface are 2.28 Å for TPPO on perfect surface and 2.21 Å for O vacancy structure (Figure 2.5b), respectively. The TPPO molecule adsorption on SnO_2 surface causes a change in the local structure.

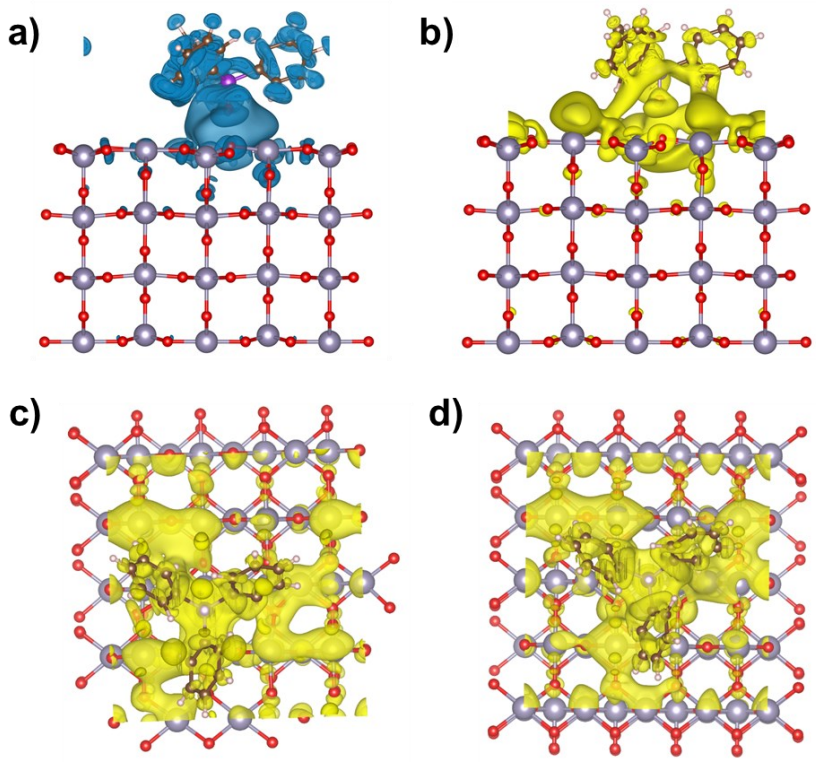

Figure 2.6 Charge density difference (Δρ) of TPPO on SnO_2 (110) surface was calculated at isovalue of 1.2×10^{-4}|e|/Å^3: a) Blue indicate electron depletion and b) yellow indicate electron accumulation. c) Charge density difference (Δρ) top view of TPPO absorbed on SnO_2 (110), electron gain is indicated by yellow. d) Charge density difference (Δρ) top view of TPPO on SnO_2 (110) surface (w/o oxygen vacancy), electron gain is indicated by yellow at isovalue of 1.2×10^{-4}e/Å^3.

In addition, the charge density differences ($\Delta\rho = \rho_{SnO_2+TPPO} - \rho_{SnO_2} - \rho_{TPPO}$) of TPPO on SnO_2 (110) surface are calculated to express the interaction between SnO_2 and TPPO molecule (Figure 2.6a-b). The resulting electron clouds at the interface demonstrate charge redistribution and a strong interaction between SnO_2 and TPPO. The blue could (Figure 2.6a) denotes the electron loss from the relative bonds or atoms after charge redistribution while the yellow (Figure 2.6b) means the electron acquired by the relative atoms. Most importantly, besides the fluctuation of electron cloud from the three benzene rings, it is vital in the conclusion that R_3P^+-O^- bond is mainly responsible for the loss of electrons while the peripheral tin atoms obtain the electrons, which is clearly shown in top

view of Figure 2.6c. This calculation result confirms our speculation that the positive charge induced by the bias voltage of EFM can be attributed to electron loss of R_3P^+-O^- σ bond. Strikingly, as Figure 2.6c shows, more received electron clouds spread to peripheral tin atoms other than the directly connected tin atoms in the redistribution. According to Bader charge analysis (Grimme, Antony, Ehrlich, & Krieg, 2010), the direct connected tin atom does not get electrons from R_3P^+-O^- σ bond. That indicates the electrons received by the peripheral tin atoms at the surface are delocalized. The yield of surface delocalized electron previously reported was attributed to non-stoichiometric states of SnO_{2-x} (Kang et al., 2010; Jung et al., 2012). As a result, the number of delocalized electrons on Sn atoms of SnO_2 surface is remarkably augmented after absorption of TPPO molecules. By the doping of TPPO, the surface electron concentration is 3.9×10^{12} cm^{-2} for the SnO_2 nanocrystals with oxygen vacancies (Figure 2.6c), and 5.1×10^{12} cm^{-2} for the defect-free SnO_2 (Figure 2.6d). From the measured electron concentration of SnO_2 nanoparticles reported recently for comparison (Xiong, Qin, et al., 2018), the two-dimensional (2D) surface electron concentration is about ~10^{10} cm^{-2} deduced from the reported values. (from the values in this literature extracted by a factor of 2/3 ($n_{2D}=(n_{3D})^{2/3}$) (Kittel & Holcomb, 1967). The possible reason for the change in the conductivity of SnO_2 ETL by TPPO doping is the improved conductivity across the grain boundaries doped by TPPO molecules.

2.3.3 c-AFM and SKPM characterization

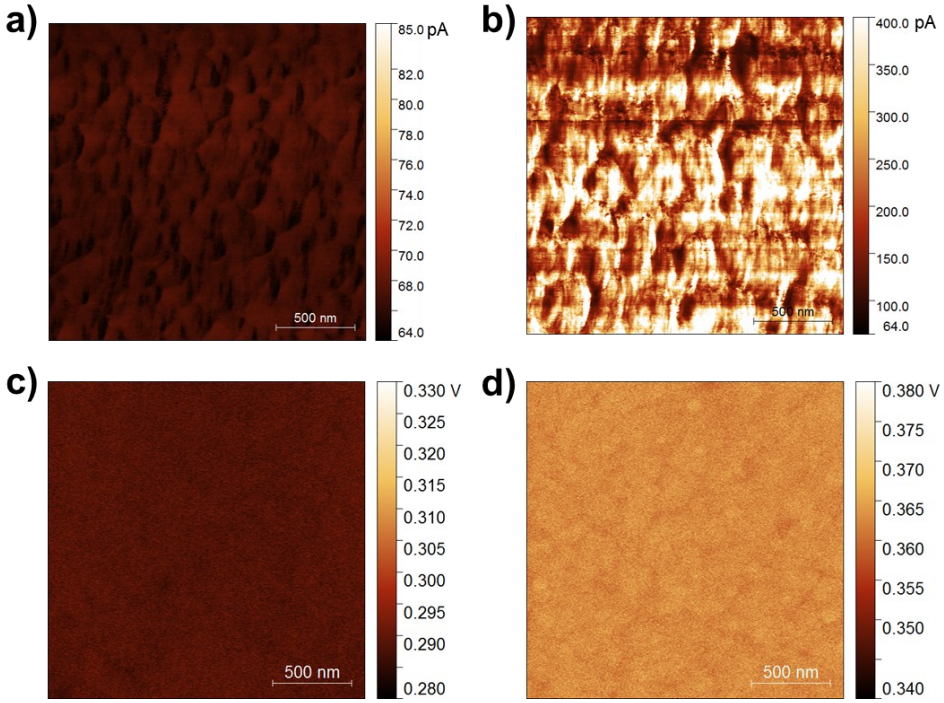

Figure 2.7 c-AFM mapping of SnO_2 (a) and TPPO doped SnO_2 (b) films. The averaged current values are 66 pA and 262 pA, respectively. SKPM images of SnO_2 (c) and TPPO doped SnO_2 (d) films.

To confirm the improved conductivity, c-AFM was introduced. As shown in Figure 2.7, the c-AFM current is enhanced from 66 pA to 260 pA in mean of the scan region after coating of TPPO molecules. The obvious topographic current contrast indicates the coverage divergence of ionized TPPO molecules penetrating throughout the bulk of SnO_2 film more than just absorbed on the film surface, which will be illustrated below. The surface delocalized electrons would also cause anisotropic dipole polarizability and hence the change of surface electrical field (MedveĎ, Fowler, & Hutson, 2000), which is verified by the increase of surface potential measured by Kelvin probe. The results show us that the surface potential of SnO_2 increased from 288 mV to 363 mV after TPPO modification.

2.3.4 Spectral properties characterization

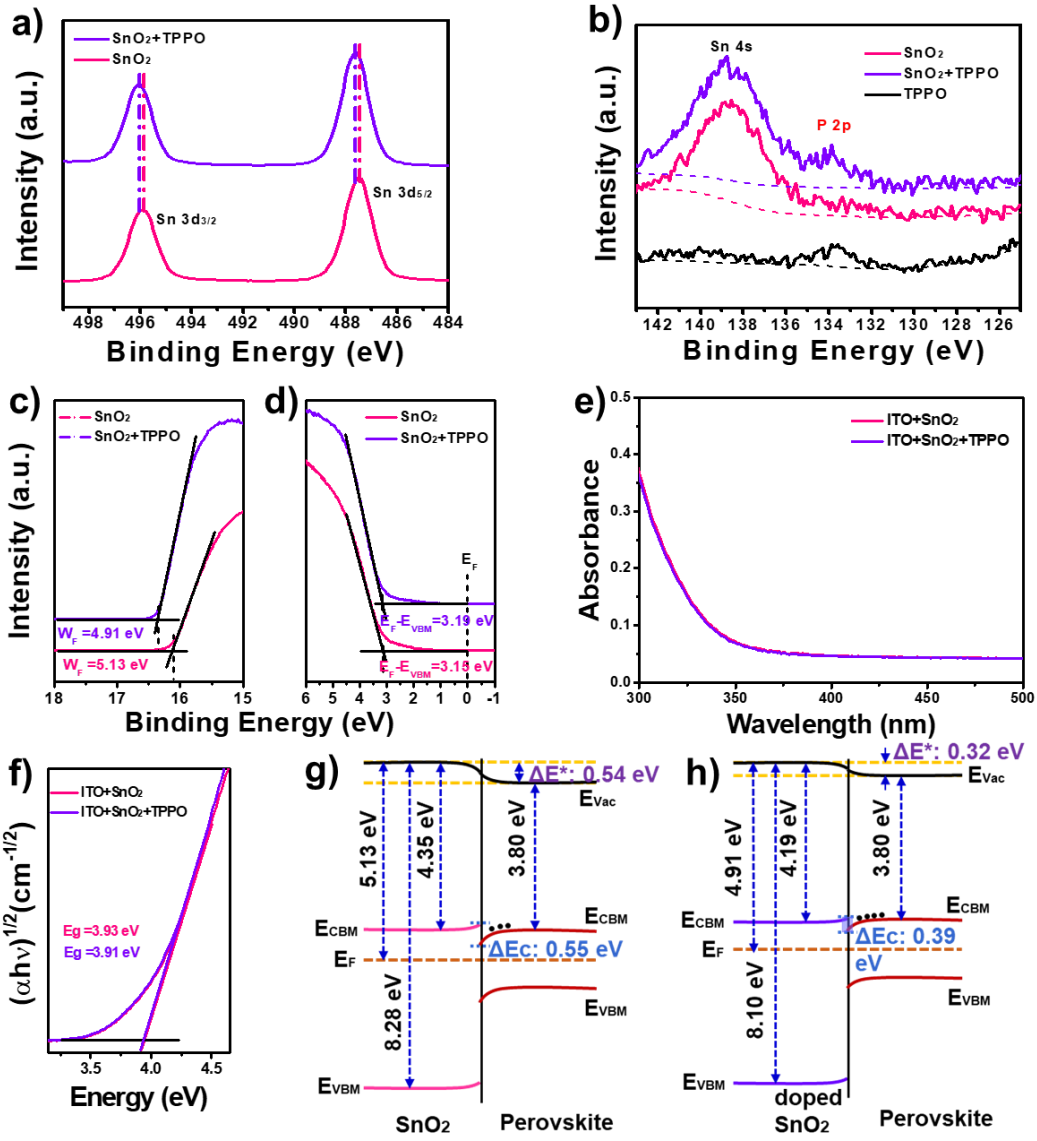

Figure 2.8 a) Sn 3d XPS spectra on SnO_2 and TPPO doped SnO_2 film. b) The signal of phosphorus circled in red in the XPS spectra of the above three samples. c) and d) The onset and tail of UPS spectra of the bare SnO_2 and TPPO doped SnO_2, respectively, where their work functions and VBMs can be derived. e) and f) UV-vis spectra and *Tauc* plots of SnO_2 and doped SnO_2, respectively. g) and h) Band level diagram of SnO_2/CsFAMA heterojunction before and after doping of TPPO, respectively.

To further confirm electron transfer from TPPO to SnO_2, XPS was used to investigate the chemical shift of tin (Figure 2.8a-b). Figure 2.8b examines the existence of TPPO thin layer on the SnO_2 surface via phosphorus element. The blue shift (towards high binding

energy) of Sn 3d shown in Figure 2.8a demonstrates electron transfer to tin atoms at the surface (Rietwyk et al., 2014; Tarasov et al., 2015). Thereafter, the work function of SnO_2 surface also shifted from -5.13 eV to -4.91 eV after modification of TPPO as the UPS results show in Figure 2.8c, the XPS and UPS results verify the electron transfer from TPPO to SnO_2. The *Tauc* plots and UV-vis spectra of SnO_2 before and after doping are shown (Figure 2.8e-f). These results show us that the doping of SnO_2 by TPPO make an decrease in band gap (from 3.93 eV to 3.91 eV), which indicates that E_{CBM}-E_F decreases after coating the thin layer of TPPO molecules, which indicates that the electron density in the SnO_2 ETL is enhanced by the surface doping. Along with the values of E_F of SnO_2 and SnO_2-TPPO derived from Figure 2.8c, the values of E_F-E_{VBM} of SnO_2 and SnO_2-TPPO was calculated as shown in Figure 2.8d. Because of the change in work function and surface electron density of SnO_2, energy band alignment may be affected. The band bending at the SnO_2/Perovskite interface leads to an energy barrier (ΔE_c) at the interface according to the basic theory of band alignment (Figure 2.8g-f,). A significant difference after TPPO doping can be observed, namely ΔE_c decreases from 0.55 eV to 0.39 eV. This is expected to facilitate electron transfer and reduce charge accumulation at interface.

2.3.5 Characterization of perovskite

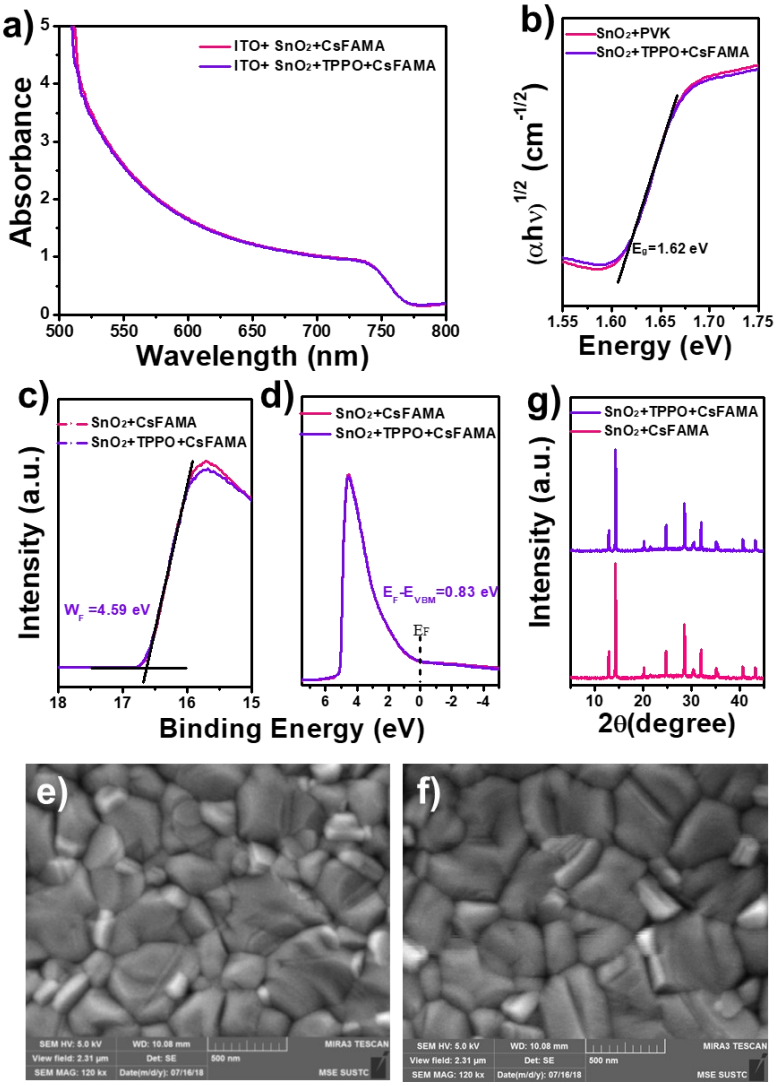

Figure 2.9 UV-vis absorption spectrum (a) and *Tauc* plots (b) of SnO_2 and perovskite in different conditions. c) and d) The onset and tail of UPS spectra of perovskite films with 600 nm in thickness deposited on the SnO_2/ITO and TPPO/SnO_2/ITO substrates, respectively. e-f) SEM images of perovskite with SnO_2 and TPPO doped SnO_2, respectively. (g) XRD patterns of perovskite with different substrates.

The UV-vis spectrum and *Tauc* plots of perovskite with different ETLs are display in Figure 2.9a-b. These results show us that the doping of SnO_2 by TPPO do not make any change to the bandgap of perovskite. The UPS results of perovskite both on SnO_2 and SnO_2-TPPO were also obtained as shown in Figure 2.9c-d. The obtained values of E_F, E_{VBM} and E_{CBM} for perovskite are -4.59 eV, -5.42 eV, and -3.8 eV, respectively. Their fermi

levels remain just 0.02 eV higher than the center of their bandgaps, which can be ascribed to the large thickness (hundreds of nm) of the perovskite layer, so that the perovskite surface is far from the interface of SnO_2/perovskite (Lu et al., 2017). In addition, Figure 2.9e-g show the topographic SEM images and XRD patterns of perovskite. High quality perovskite films are clearly obtained on both SnO_2 and SnO_2-TPPO, so that any difference in photovoltaic performance can be ascribed to the change from SnO_2 after TPPO doping (Yang et al., 2018).

2.3.6 Characterization of device performance

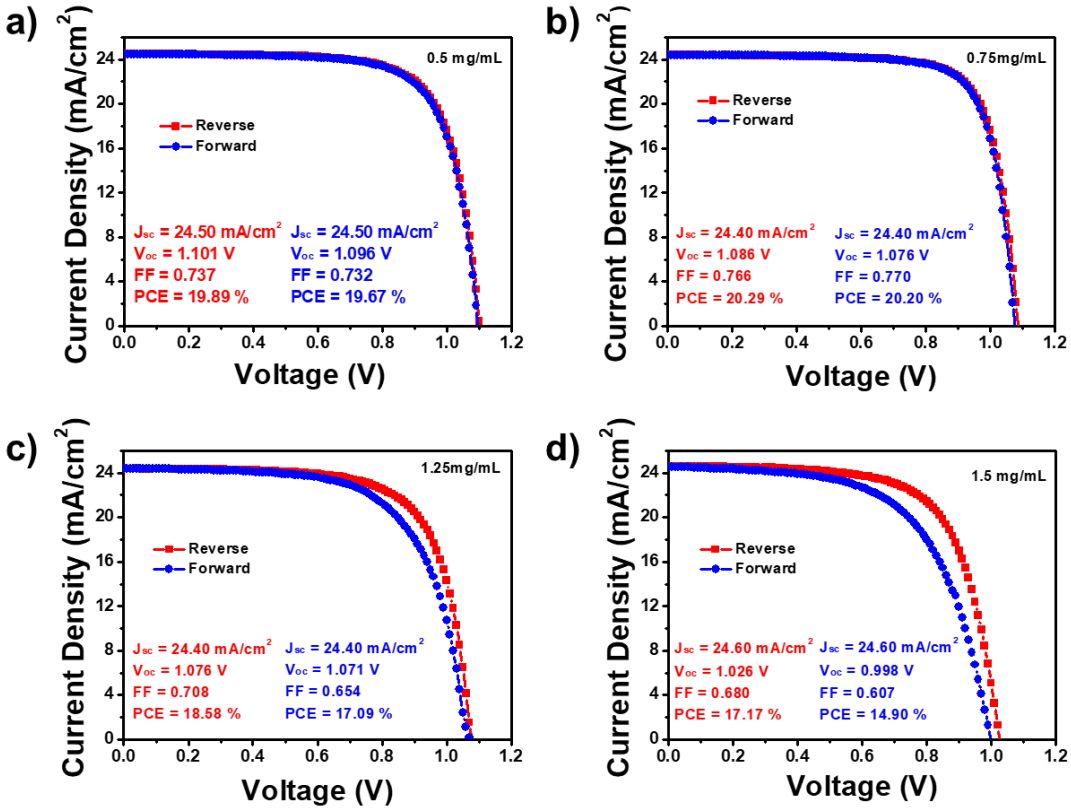

Figure 2.10 *J-V* curves of optimal devices with different TPPO concentration doped SnO_2 ETL.

The surface molecular doping effect in this work was demonstrated in device performance by "ITO/SnO_2(-TPPO)/CsFAMA/Spiro-MeOTAD/Au" configuration. According to the performance sensitivity with the molecule layer thickness and coverage

(Chen et al., 2018; Chen, Xu, Feng, Jie, & He, 2017; Chen et al., 2016), different concentration of TPPO solutions were employed to tune them and optimize the device performance (Figure 2.10). The best device performance was obtained for TPPO concentration of 1 mg/mL.

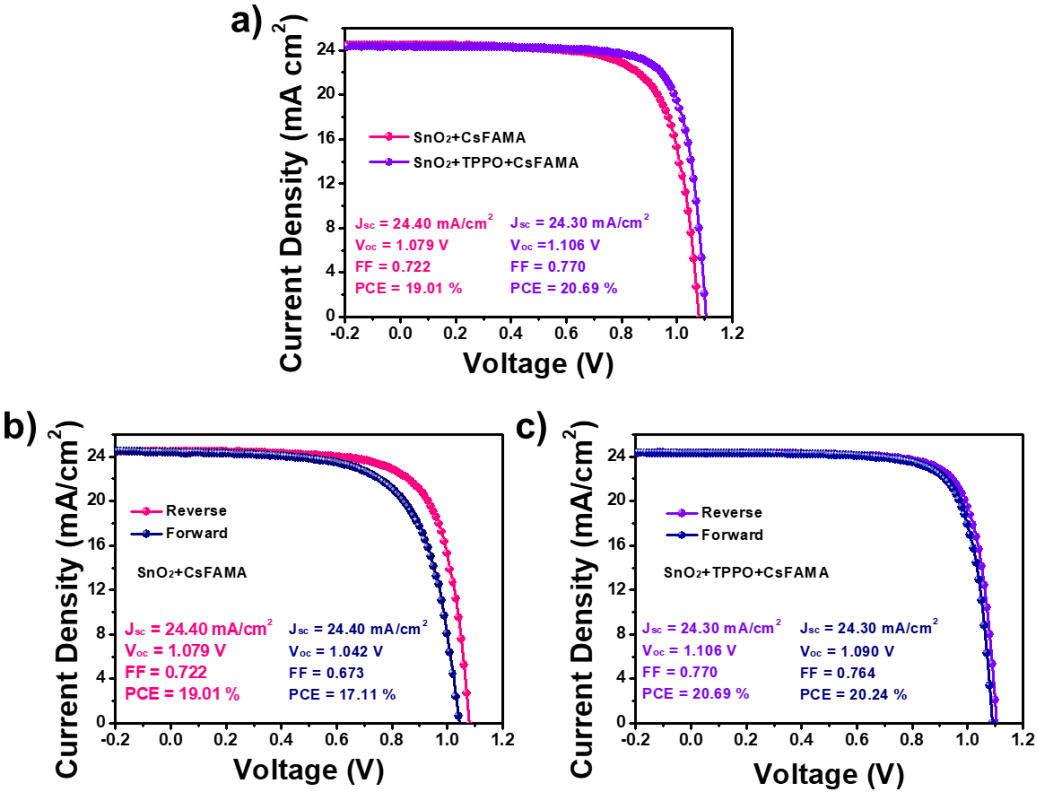

Figure 2.11 a) *J-V* curves of optimal devices with SnO_2 and TPPO (1mg/mL)-doped SnO_2 in reverse scan. Hysteresis characteristics of each optimal devices with SnO_2 (b) and TPPO-doped SnO_2 (c).

The champion cell's *J-V* curves in reverse scan based on bare SnO_2 based (pink) and the SnO_2-TPPO based (purple) devices along with their corresponding parameters are shown in Figure 2.11. The PCE shows obvious improvement from 19.01% to 20.69%, and V_{oc} increased from 1.079 V to 1.106 V while current density (J_{sc}) shows small decrease after surface doping of TPPO on SnO_2 ETLs.

Table 2.1 Photovoltaic parameters based on SnO_2 and TPPO doped SnO_2 ETLs derived from *J-V* measurements.

ETLs	Scan direction	J_{sc} [mA/cm^2]	J_{sc} by EQE [mA/cm^2]	Voc [V]	*FF* [%]	PCE [%]	H-index [%]
SnO_2	Reverse	24.27±0.66[a] (24.40)[b]	23.10	1.06±0.03[a] (1.079)[b]	72.20±2.50[a] (72.22)[b]	18.59±0.42[a] (19.01)[b]	9.99
	Forward	24.40		1.073	67.3	17.11	
TPPO doped SnO_2	Reverse	24.38±0.14[a] (24.30)[b]	22.97	1.10±0.02[a] (1.106)[b]	73.73±3.42[a] (77.0)[b]	19.84±0.85[a] (20.69)[b]	2.17
	Forward	24.30		1.090	76.4	20.24	

a) The averaged values; b) The values corresponding to the champion devices.

The performance parameters statistic results can be found in Figure 2.12 and Table 2.1. The average value of J_{sc}, increased from 24.27 mA/cm^2 to 24.38 mA/cm^2 with the PCE improved from 18.59% to 19.84%. Also noted that the J_{sc} of devices on bare SnO_2 exhibit significantly larger standard deviation compared to those on SnO_2-TPPO (0.66 vs. 0.14 mA/cm^2). This indicates improvement in surface quality and uniformity with TPPO doping. Figure 2.12d shows us the PCE distribution of the two kinds of devices for comparison, which shows the average PCE value was augmented obviously.

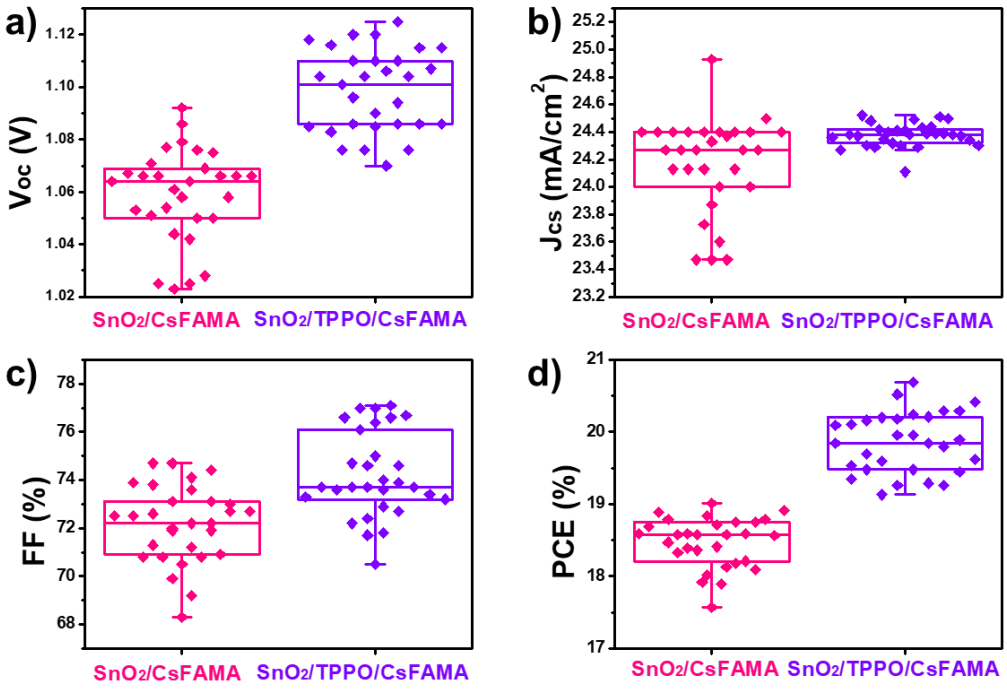

Figure 2.12 Photovoltaic parameters statistics for SnO_2 and TPPO doped SnO_2 devices.

From the EQE spectra of each champion device (Figure 2.13a), the integrated J_{sc} values are 23.10 mA/cm^2 and 22.95 mA/cm^2 respectively. Small underestimation of J_{sc} from EQE measurements is common, and it likely originates from the spectral mismatch from solar simulator and theoretical AM1.5G spectrum, although the effect of device degradation during transportation to another building for the measurement cannot be excluded. The increased V_{oc} can be ascribed to the barrier reduction and band alignment at the SnO_2/Perovskite by TPPO modification (Correa Baena et al., 2015; D. Yang et al., 2016). The key factor for the increased PCE derived from the enhancement of *FF* from 0.722 to 0.770. Maximum power point tracking (MPPT) was also performed to evaluate the stabilized power output (Figure 2.13b) (D. Yang et al., 2015), the optimal device yielded a stabilized PCE of 18.71% for the SnO_2 and 20.42% for the TPPO doped SnO_2, which were recorded after 300 s light soaking and are comparable to the reference.

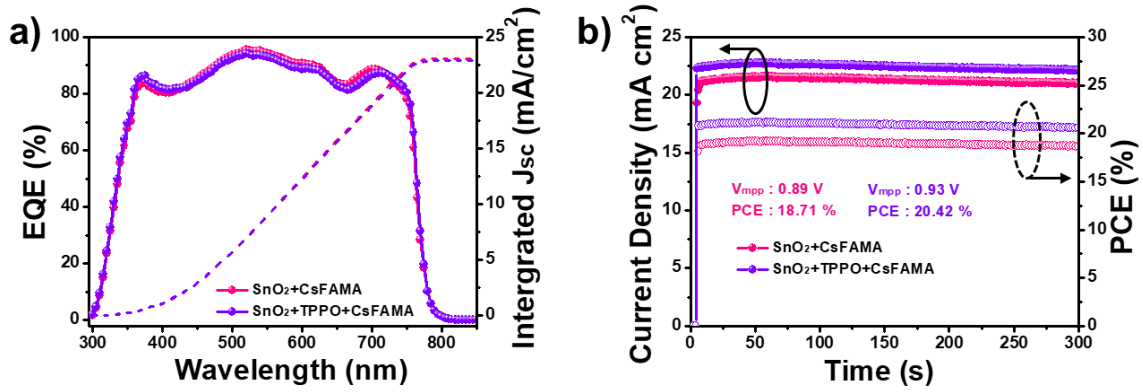

Figure 2.13 a) EQE results and corresponded integrated J_{sc} of each PSCs. b) The output of photocurrent and PCE at a fixed bias voltage of its initial maximal power point of each champion device.

In addition to the enhancement of PCE, the hysteresis was also suppressed after TPPO doping (Figure 2.11b-c). Since the PSCs commonly exhibit hysteresis, hysteresis index "*H*-index" was introduced to quantify the hysteresis degree: *H*-index = ($PCE_{reverse}$ − $PCE_{forward}$)/$PCE_{reverse}$.(Q. Jiang et al., 2017) *H*-index decreases remarkably from 9.99% to

2.17% after doping of TPPO, which may be attributed to the optimization of energy level alignment, which enhanced electron transfer at the interface and reduced charge accumulation (Ayguler et al., 2018; Tan et al., 2017).

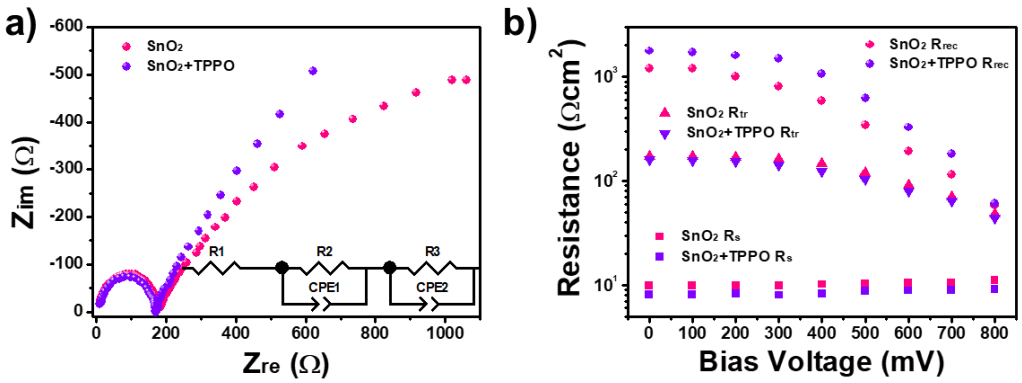

Figure 2.14 a) Nyquist plots of different devices, the insert is equivalent circuit of the solar cells. b) Interfacial Series resistance, recombination resistance and electric charge transfer at different bias.

To investigate the mechanisms responsible for the increased *FF*, EIS measurements were performed. Figure 2.14a shows us the Nyquist plots of different devices with their equivalent circuit also shown. From the plots, high-frequency intercept value on the real axis is equal to the series resistance (R_s) (Todinova, Idigoras, Salado, Kazim, & Anta, 2015), low-frequency component refers to the recombination resistance (R_{rec}) (Yang et al., 2015) and high-frequency component corresponds to the transfer resistance (R_{tr}). Shown as Figure 2.14b, the R_s of the SnO_2-TPPO based device is always lower than that of the bare SnO_2 based one. Both devices have low R_s values of several ohms. The observed trend for R_{tr} is similar to R_s. The recombination resistance, however, increased for SnO_2-TPPO based devices. This indicates lower recombination rate and/or faster extraction of the electrons after TPPO doping (Todinova et al., 2015), in agreement with the device performance improvements and the reduction of the energy barrier for electron transfer.

2.3.7 Characterization of structure and composition

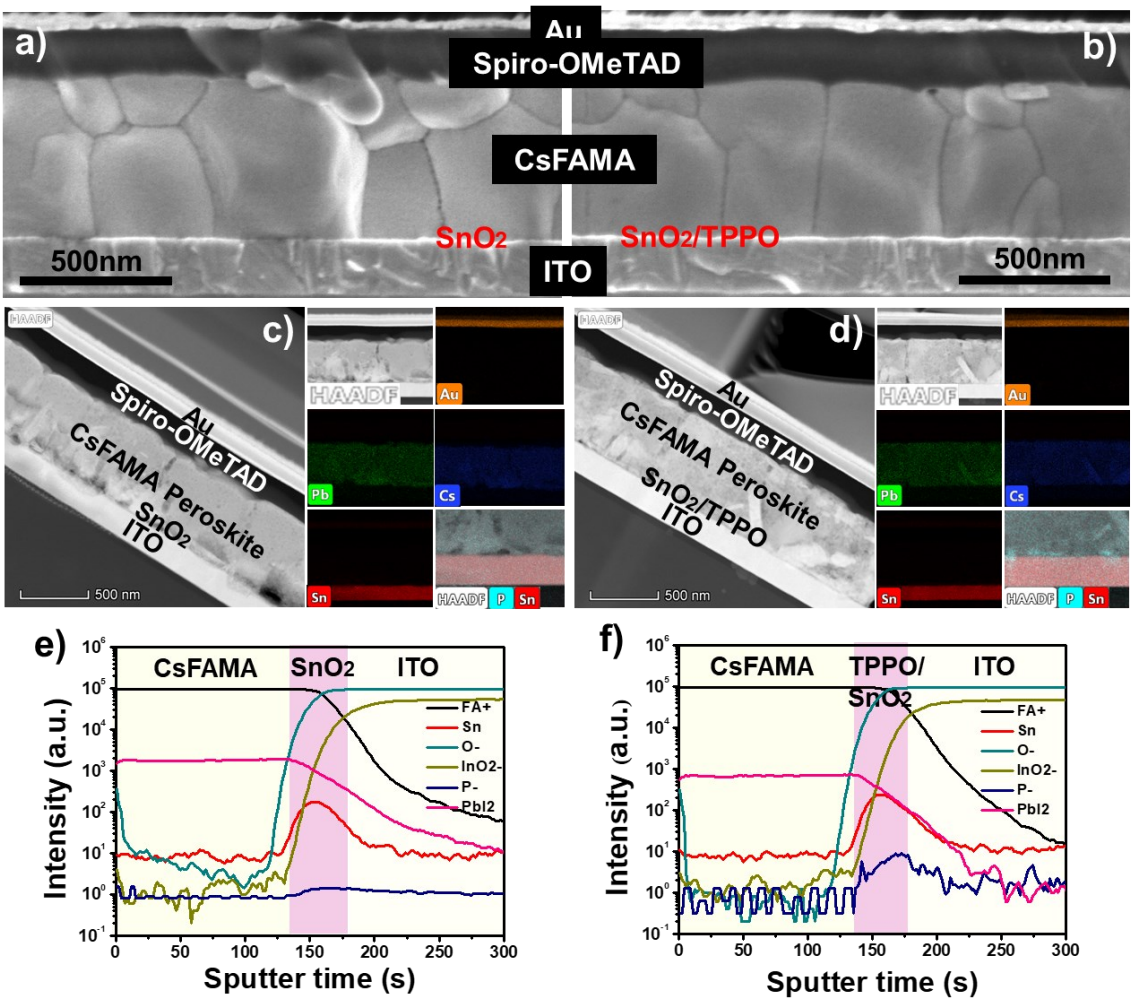

Figure 2.15 Cross-section SEM images of devices with SnO_2 (a) and TPPO doped SnO_2 (a), respectively. Cross-sectional STEM images and related elemental mappings of PSCs with SnO_2 (c) and TPPO doped SnO_2 (d), respectively. ToF-SIMS profiles of heterojunctions ITO/SnO_2/perovskite (e) and ITO/SnO_2-TPPO/perovskite (f), respectively.

The obtained results clearly demonstrate device performance improvement of PSCs with doping of SnO_2 ETL by TPPO molecules. To further examine the effect of TPPO on the devices and rule out additional differences affecting the device performance, further structural and compositional characterization was performed. Typical cross-section SEM images of PSCs with different substrates were displayed in Figure 2.15a-b. The perovskite films inside are ~600 nm in thickness with compact and large crystalline grains for both

kinds of ETLs. The thickness of Spiro-MeOTAD and Au layers are also comparable with each other. Due to the resolution limit, the SnO_2 nanocrystals morphologies cannot be distinguished in these images. Elemental mapping using STEM was also investigated for detailed information in high resolution, especially the element mapping function. Here, the cross-section samples with thickness of ~100 nm were prepared by the FIB technique. In Figure 2.15c-d, the elemental mappings of Pb and Cs prove their uniformity in the perovskite layer. The gold electrode layers are also clearly detected. Because the ITO film also contains tin, it's difficult to specify the SnO_2 nanocrystals from the ITO electrode film in these elemental mapping. However, tiny amount of phosphorus was clearly detected in the cross section of SnO_2-TPPO based devices (Figure 2.15d). This result was also confirmed by the depth profile of phosphorus concentration characterized by ToF-SIMS. Figure 2.15e-f list depth profile concentration of some key elements involved in the device structure, where the pink band indicates the approximate position of the SnO_2 ETL layer. The presence of phosphorus (dark blue line in Figure 2.15e-f) can be clearly observed throughout the SnO_2-TPPO, which indicates that TPPO molecules may penetrate throughout the SnO_2 layer and be absorbed at the grain boundaries. In addition, we can observe a difference in perovskite ion profiles, which may indicate possible reduction in the ion diffusion, which is consistent with grain boundary passivation in SnO_2 ETL and may also contribute to the reduced hysteresis.

2.4 Conclusions

In summary, the optimization of ETL has been realized by the molecular doping of SnO_2. The electron transfer was verified directly by EFM and confirmed by the shift in Sn 3d core level of XPS results to higher energy. The DFT simulation reveals that the interaction between TPPO and SnO_2 surface (with or w/o oxygen vacancy) is very strong

and the electrons are transferred mainly to peripheral tin atoms instead of directly connected tin atoms from the high polarity σ-bond, which results in the presence of delocalized electrons at the surface, and consequently increased conductivity and decreased work function. This in turn results in an increasement in built-in field and a reduction in energy barrier at ETL/perovskite interface. Molecular doping by TPPO enables an increase in PCE from 19.01% to 20.69%, while the hysteresis index is significantly reduced from 9.99 % to 2.17%. The improvements in the device performance can be attributed to faster electron extraction and lower recombination rate. This comprehensive work confirms the availability of transport layer optimization, broadens the scope of rising organic/inorganic hybrid electronics, and provides deeper insight into the mechanisms of surface molecular doping.

3. Optimization of SnO_2 transport layer by defects passivation

3.1 Introduction

PSCs has given rise to extensive interests owing to their fascinating photovoltaic properties, with certified PCE as high as 25.2% within a short period of time (Jung et al., 2019; Luo et al., 2019). High efficiency PSCs typically have n-i-p architecture with high temperature (＞500 ˚C) processed mesoporous oxide charge collection layers, which complicate device fabrication and are only compatible with rigid substrates.

Planar PSCs recently have attracted tremendous attention based on simplified process at low temperature, which enable their fabrication compatible with large scale slot die coating technique on flexible substrates. Perovskite active layer is required to be deposited on n-type charge collective layers in planar n-i-p PSCs. Thus, the n-type semiconductor significantly determines the crystallization quality of the perovskite. Perovskite with high crystallinity, large grain size together with low defects are important for the final PCE of PSCs. As a result, the n-type contact heterojunction plays a critical role in suppressing the interfacial recombination and reducing charge accumulation, then the final PSCs efficiency and stability. SnO_2 is an effective ETL due to its high transparency, suitable energy level, superior charge collection ability and high conductivity without a high temperature process (Jiang et al., 2017; Tu et al., 2019). However, like most metal oxide semiconductors, solution processed SnO_2 ETLs usually have large amount of electronic trap states (metal ion vacancy, oxygen vacancy) and surface defects, which can function as recombination center, leading to recombination and loss of charge carriers (Boehme et al., 2015; Bozyigit, Lin, Yazdani, Yarema, & Wood, 2015; Bozyigit, Volk, Yarema, & Wood, 2013; Katsiev et al., 2014). This is likely to result in large charge accumulation and

ineffective electron transfer rate at the SnO_2/perovskite heterojunction, and thereafter large photovoltage deficits and current hysteresis.

Great efforts also have been made to optimize and stabilize the SnO_2/perovskite heterojunction via interfacial modification with functional materials such as self-assembled monolayer molecule, inorganic binary alkaline halides, fullerene derivatives, etc (Choi et al., 2018; K. Liu et al., 2018; Yang et al., 2018). For example, Yang proposed EDTA modified tin oxide effectively improve the SnO_2/perovskite interface, increased to PCE to 21.60% with negligible hysteresis (Yang et al., 2018). Because of oxygen-vacancy-related defects passivation, fullerene derivative modified SnO_2 results in suppresses charge recombination (Liu et al., 2018).

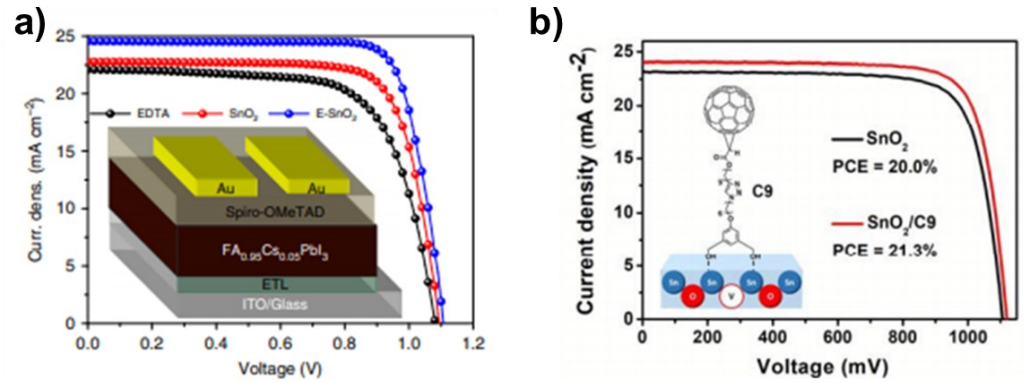

Figure 3.1 EDTA (a) and fullerene derivative (b) Modified tin dioxide for high efficiency PSCs (K. Liu et al., 2018; D. Yang et al., 2018).

However, all these interfacial modifications are only improved the SnO_2/perovskite interface without any passivation on the defects/vacancy inside SnO_2 ETL. An ideal SnO_2/perovskite heterojunction should eliminate interfacial recombination and minimize the charge transport losses within the SnO_2 layer. We believe in such way, high efficiency with low interfacial losses and high stability planar PSCs can be achieved. Here, we aim to optimize the SnO_2 transport layer by defect passivation and propose a novel strategy to stabilize the SnO_2/perovskite heterojunction via simultaneous passivation of SnO_2

nanocrystal ETL and SnO_2/perovskite interfaces by 3-aminopropyltriethoxysilane (APTMS) molecule.

3.2 Experimental section

3.2.1 Materials

Anhydrous solvents DMF, DMSO, CB were purchased from Acros Organics. Spiro-OMeTAD, FK209, Li-TFSI, and tBP were obtained from Xi'an Polymer Light Technology Corp. CsI and APTMS were achieved from Sigma-Aldrich. $PbBr_2$ and PbI_2 were obtained from TCI. FAI and MABr were achieved from Great Cell Solar Ltd (Australia). The SnO_2 colloid precursor was purchased from Alfa Aesar.

3.2.2 Preparation of SnO_2 and H_2N-SiO_X@SnO_2 films

Diluted the SnO_2 colloid precursor by H_2O to 2.67% before use. Spin coating (3500 r.p.m., 30s) this diluted solution and annealed at 180 ˚C for the deposition of SnO_2 films. For the APTMS modified SnO_2 film preparation, SnO_2 precursor solution with different APTMS percent (v/v) was coated after stirring.

3.2.3 PSCs Fabrication

Firstly, ITO was cleaned with detergent, deionized water, ACN and IPA, sequentially. Then, deal with UVO for 15 minutes. Then, SnO_2 or H_2N-SiO_X@SnO_2 was spin coated. perovskite precursor was achieved by mixing MABr, FAI, $PbBr_2$ and PbI_2 in DMF/DMSO (volume ratio is 4:1) with the mole ratio of FA/MA and I/Br maintained at 0.87/0.13, and the mole concentration of PbI_2 kept at 1.1 M. After stirring for 1 hour at 60 ˚C, 35 μL of CsI (2 M dissolved in DMSO) was injected and stirred for another 1 hour. Spin coating (2000, 10s and 6000, 20s) the precursor solution and antisolvent (100 μL CB) was dropped 10 s prior to the end. After perovskite growth, Spiro-OMeTAD/CB (72.3 $mg \cdot mL^{-1}$) solution with tBP (28.5 μL), Li-TFSI/ACN (17.8 μL, 520 $mg \cdot mL^{-1}$) and

FK209/ACN (30μL, 300 mg·mL^{-1}) was spin coated (4,000 r.p.m., 30 s). At last, Au was deposited by thermal evaporation method.

3.2.4 Characterization

All experiments were processed in ambient condition. Fourier Transform infrared spectroscopy (FTIR) was achieved by a PE Frontier FT-IR spectrometer. AFM-based characterizations were realized with AFM (MFP-3D-BIO, Asylum Research, USA). Silicon tips coated with Ti/Ir (ASYELELC-01-R2, k ~ 1.4-5.8 N/m, f ~ 58-97 KHz) were employed in SKPM imaging. XPS and UPS measurements were carried out on Thermo Fisher (ESCALAB 250Xi, Al Kα x-ray source, 10^{-9} mbar). XPS results were calibrated with C 1s. 10 V bias was applied in the UPS test with Au as reference. UV measurements were completed with UV/Vis/NIR Spectrometer (Perkin Elmer, Lambda 950). *J-V* measurements were performed in in ambient condition (27 ºC, 75% RH) with a Keithley 2400 sourcemete. Illumination was provided by solar simulator (Oriel Sol3A, AM1.5G spectrum, calibrated by KG-5 Si diode). All devices were measured both in forward scan and reverse scan with 10 ms delay time. EQE measurements were carried out by Enli Tech (Taiwan). Morphology was achieved by SEM (TESCAN MIRA3), cross-section morphology, EDX mapping and STEM images were realized by TEM (FEI Talos) and FIB (Helios Nanolab 600i). XRD was recorded from X-ray Diffractometer (BRUKER ECO D8 series). EIS was carried out in ambient environment (26 ˚C, 39% RH) by electrochemical station (Zahner IM6e, Zahner, Germany). PL and TRPL spectrums were achieved with Spectrofluorometer (FS5, Edinburgh, 405 nm pulsed laser). Electron mobilities were measured with Space-Charge-Limited Current (SCLC) method. Electron-only structure ITO/ SnO_2 or H_2N-SiO_X@SnO_2 /C60/BCP/Ag was used. The mobility was

calculated based on MOTT-Gurney equation: $J = \frac{9}{8}\varepsilon_0\varepsilon_r\mu\frac{V^2}{d^3}$ Where J refers to the current density, ε_0 refers to the permittivity of empty space, ε_r refers to the relative dielectric constant, μ refers to the electron mobility, d refers to the thickness of ETLs, V refers to the internal voltage in the device, and $V = V_{appl}$-V_{bi} where V_{appl} is the applied voltage and V_{bi} refers to the built-in voltage resulting from the relative work function difference between the two electrodes and can be neglected.

3.3 Results and discussion

3.3.1 Proposed possible reaction mechanism

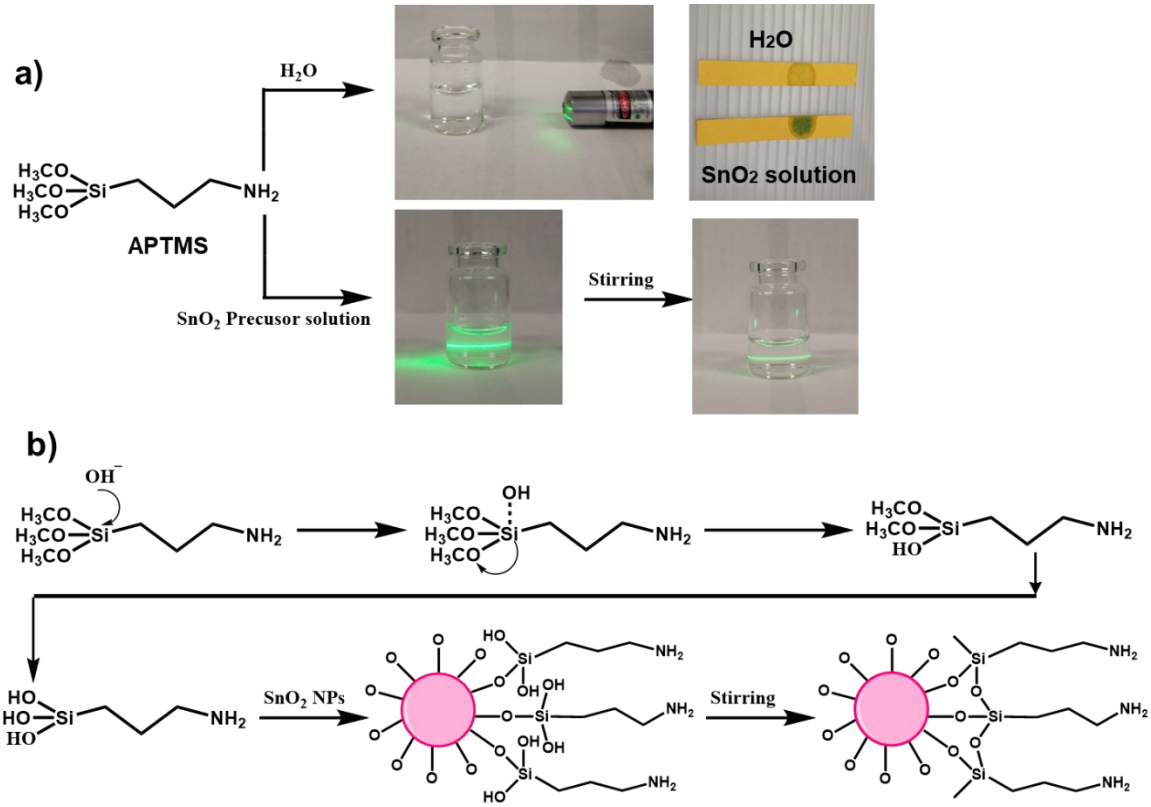

Figure 3.2 a) Photos after adding APTMS into H_2O and SnO_2 precursor solution. b) Proposed possible reaction mechanism of the H_2N-SiO_X@SnO_2 nanoparticles.

For the optimization of SnO_2, different amount of APTMS were added into SnO_2 nanoparticles solution in water. The solution became cloudy suddenly owing to the hydrolysis of APTMS and become clear after it anchored onto the SnO_2 surface via

hydrogen bonds (as shown in Figure 3.2) (Palanivel, Zhu, & Ooij, 2003). The speculated bonding mode between SnO_2 and APTMS has been illustrated in Figure 3.2b, where APTMS primers to polymerize into a polymeric network surrounding the nanoparticles.

3.3.2 Identify the formation of H_2N-SiO_X@SnO_2

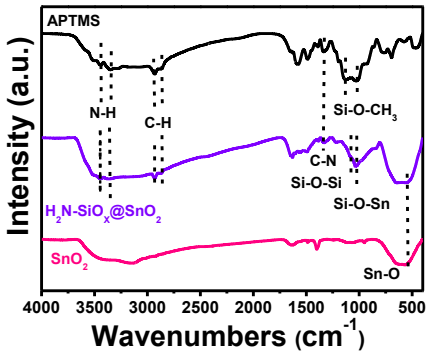

Figure 3.3 FTIR spectrum of SnO_2 and H_2N-SiO_X@SnO_2 nanoparticles.

From the FTIR results (Figure 3.3), the H_2N-SiO_X@SnO_2 nanoparticles contained the absorption bands around 600 cm^{-1}, a typical IR absorption peak originating from the stretching mode of the Sn-OH bond (Gattu et al., 2015), and the new peaks appeared upon reacted with APTMS. The additional absorptions of NH_2 at 3448 and 3355 cm^{-1}, C-N at 1331 cm^{-1}, C-H at 2927 and 2869 cm^{-1}, Si-O-Si at 1078 cm^{-1} and Si-O-Sn at 1021 cm^{-1} suggested that APTMS was introduced onto the surface of SnO_2 successfully (Maji, Choudhary, & Majhi, 2017; Moussodia, Balan, Merlin, Mustin, & Schneider, 2010).

The presence of silicon element in the mapping of H_2N-SiO_X@SnO_2 nanoparticles shown in Figure 3.4b-c also indicated the successful capping. As shown in Figure 3.4d-g, both the SnO_2 and H_2N-SiO_X@SnO_2 nanoparticles were well-dispersed in water with average diameters of approximately 3 nm, indicates the capping of APTMS does not induce any aggregation. A resembling crystal structure with the (110), (101), (200) and (211) diffraction peaks occurring at 21.2˚, 30.2˚, 35.2˚ and 50.5˚, respectively, which are ascribed to tetragonal SnO_2 (Figure 3.5) (Jiang et al., 2017).

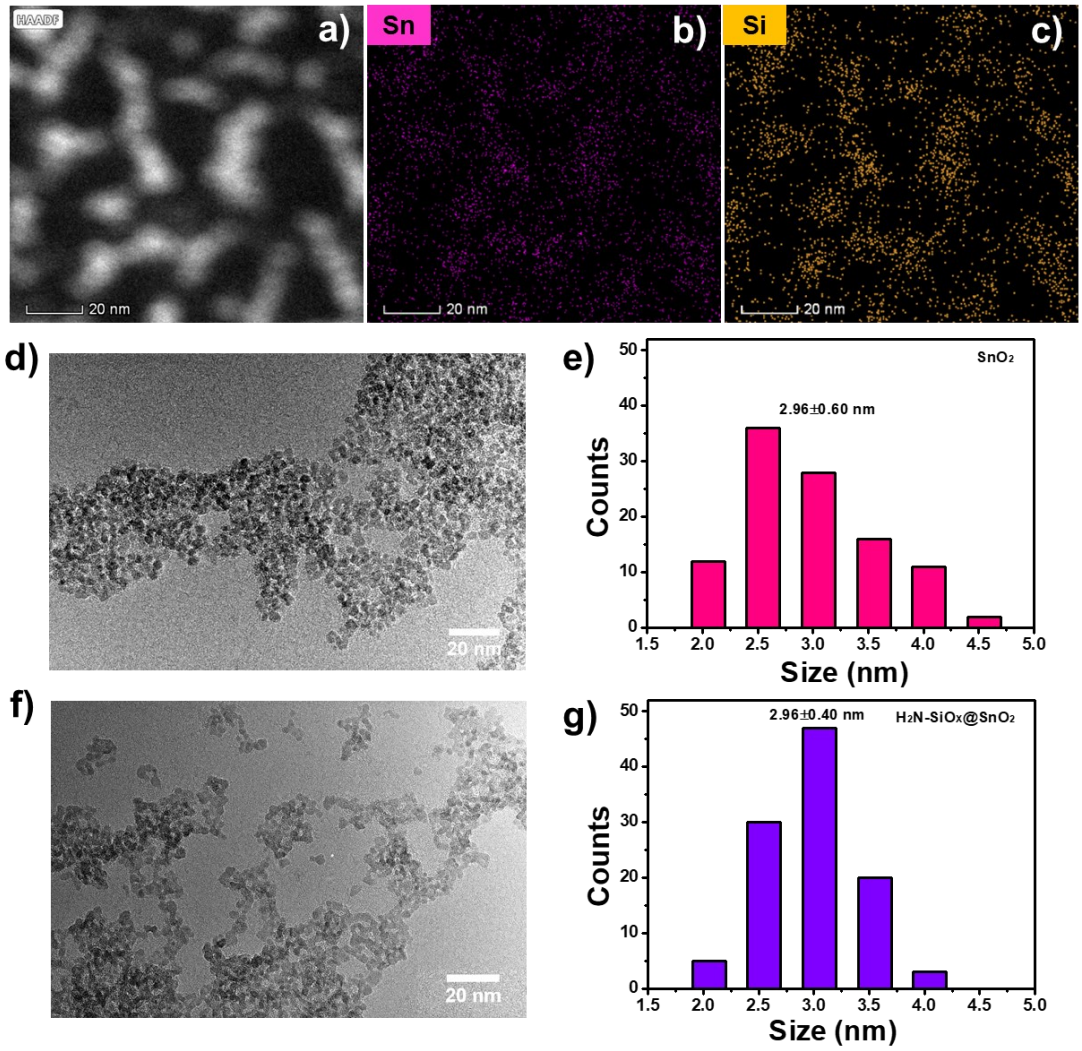

Figure 3.4 a) HAADF TEM images of H_2N-SiO_X@SnO_2 nanoparticles and b,c) EDS element mapping (Sn and Si). d-g) TEM images and average diameter of the pristine SnO_2 and H_2N-SiO_X@SnO_2 nanoparticles, respectively.

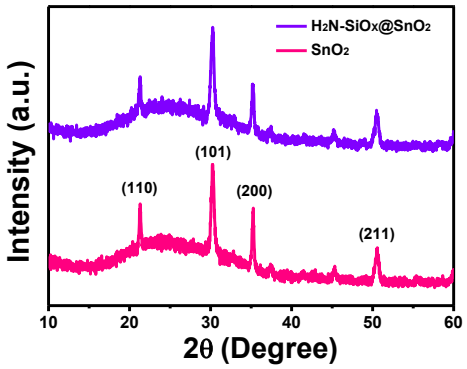

Figure 3.5 Powder XRD patterns of SnO_2 and H_2N-SiO_X@SnO_2 films.

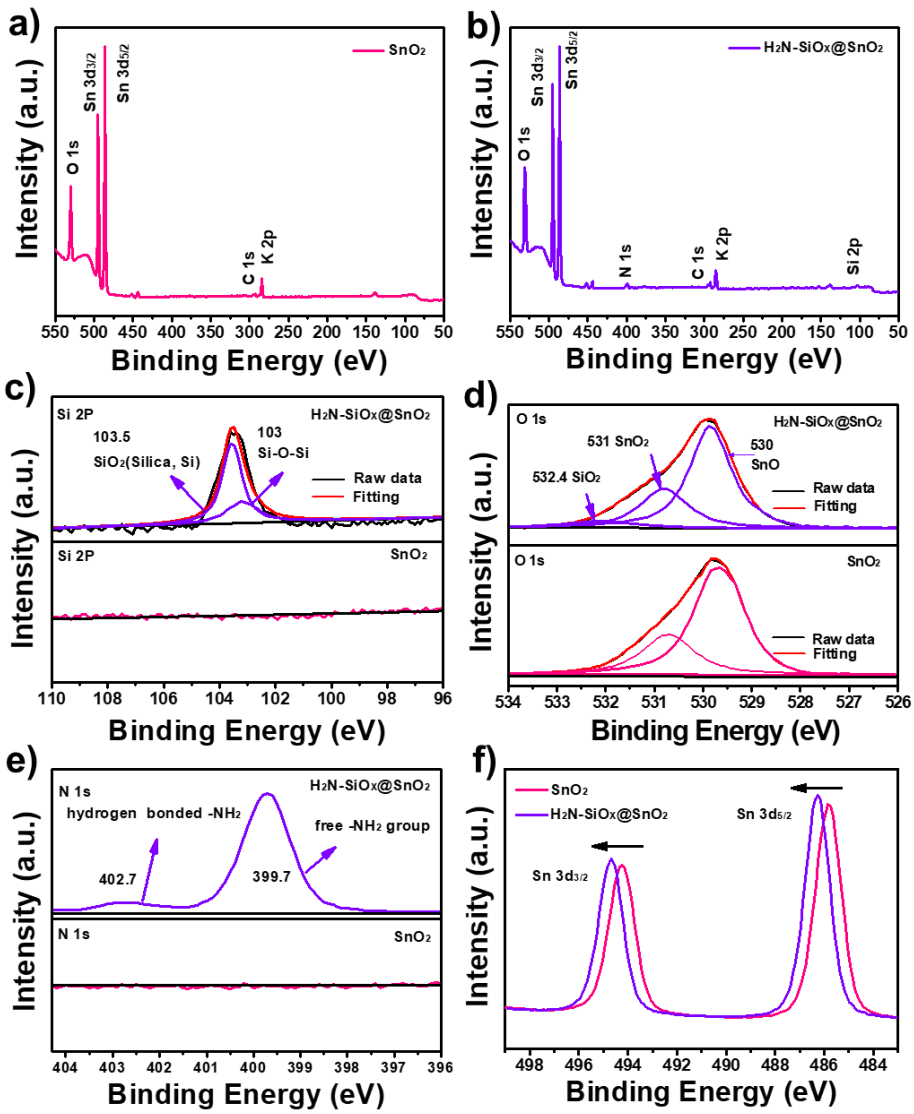

Figure 3.6 XPS survey spectrum of SnO_2 (a) and H_2N-SiO_X@SnO_2 (b) films, respectively. c) Si 2p core level XPS spectrum of SnO_2 and H_2N-SiO_X@SnO_2 films. d) O1s 3d core level XPS spectrum of SnO_2 and H_2N-SiO_X@SnO_2 films. e) N 1s core level XPS spectrum of SnO_2 and H_2N-SiO_X@SnO_2. f) Sn 3d core level XPS spectrum of SnO_2 and H_2N-SiO_X@SnO_2 films.

The presence of N 1s peak (~400 eV) and Si 2p peak (~104 eV) in the XPS survey spectrum (Figure 3.6a and b) supported the formation of H_2N-SiO_X@SnO_2 nanoparticles. Besides, the Si 2p XPS spectra (Figure 3.6c) shows the existed of Si-O group, which is confirmed from O 1s XPS spectrum (Figure 3.6d). The N 1s XPS spectra (Figure 3.6e) shows the existence of free -NH_2 groups (~399.7 eV) and hydrogen-bonded -NH_2 groups

(~402.7 eV), the higher contribution of the free -NH_2 than hydrogen-bonded -NH_2, means that the APTMS molecules are mostly bound to the SnO_2 nanoparticles through the methoxy group and the -NH_2 group remained free outside, corresponding to our assumptions above (Figure 3.2a) (Rong et al., 2018).

3.3.3 Characterization of photoelectrical properties

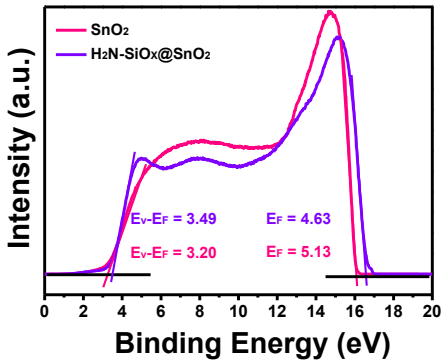

Figure 3.7 UPS spectra of SnO_2 and H_2N-SiO_X@SnO_2 films.

The influence of APTMS capping on photoelectrical properties has been studied by UPS. According to the UPS spectra as exhibited in Figure 3.7, work function shifted to 4.63 eV from 5.13 eV owing to the capping of APTMS, the reduction of work function might be ascribed to the electron donor ability of silicon (Fu, Guo, Wang, Ye, & Li, 2017). Here, XPS was also introduced. The Sn 3d binding energy peak of H_2N-SiO_X@SnO_2 shifts to higher value (Figure 3.6F), indicated that the shift of fermi level to the conduction band edge (Tarasov et al., 2015), which is match with the UPS results.

The effect of APTMS capping on the work function was also investigated by SKPM. Figure 3.8 shows the topographic AFM and SKPM results of SnO_2 and H_2N-SiO_X@SnO_2 on ITO. Compared to SnO_2, the averaged surface potential of the H_2N-SiO_X@SnO_2 is increased, suggested the reduction of work function after modification, means electrons can be extracted at relatively lower energy level (Chen et al., 2017; Chen et al., 2017).

This result is well agreement with the results calculated from UPS spectra.

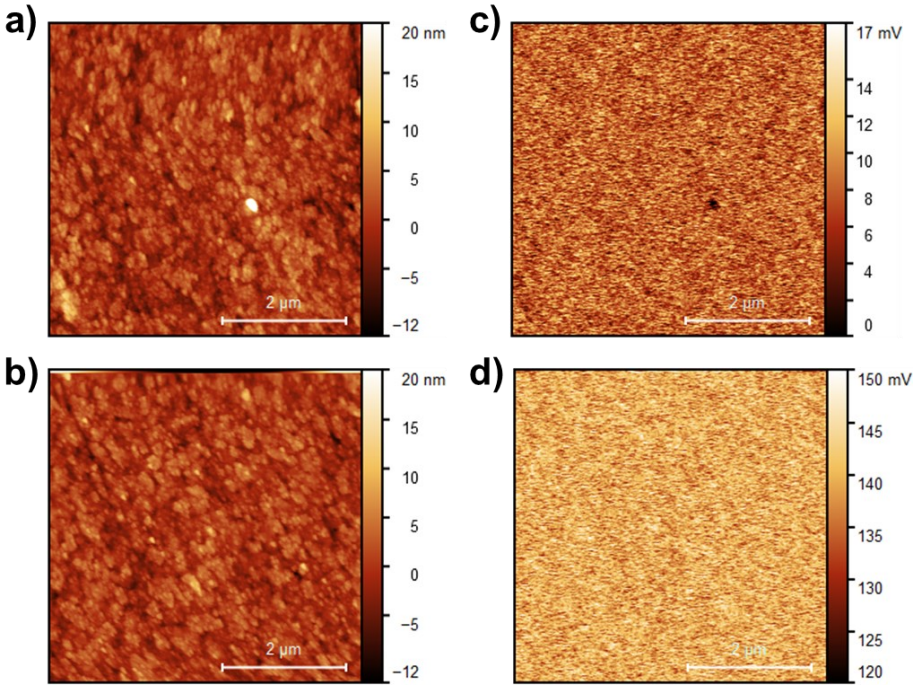

Figure 3.8 a, b) AFM images of SnO_2 and H_2N-SiO_X@SnO_2 films, respectively. c, d) SKPM images of SnO_2 and H_2N-SiO_X@SnO_2 films, respectively.

3.3.4 Characterization of electron mobility and conductivity

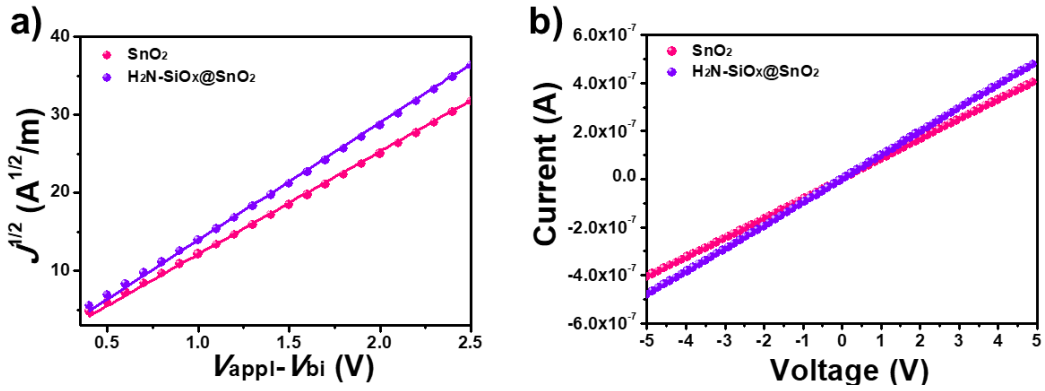

Figure 3.9 a) Mobility of SnO_2 and H_2N-SiO_X@SnO_2 based on the ITO/ETL/C_{60}/BCP/Ag, with the SCLC method. b) Conductivity measured for SnO_2 and H_2N-SiO_X@SnO_2 based film.

The measured SCLC in Figure 3.9a shows an increment in electron mobility (from 1.13×10^{-3} cm^2 $V^{-1}s^{-1}$ to 4.61×10^{-3} cm^2 $V^{-1}s^{-1}$) after formation of H_2N-SiO_X@SnO_2 indicated a reduction in the recombination in the ETL layer itself. Similar trend was found

in the measured conductivity values (Figure 3.9b). The small increase in the conductivity of H_2N-SiO_X@SnO_2 is beneficial to the increasement of *FF* for PSCs.

3.3.5 Effect of H_2N-SiO_X@SnO_2 for perovskite

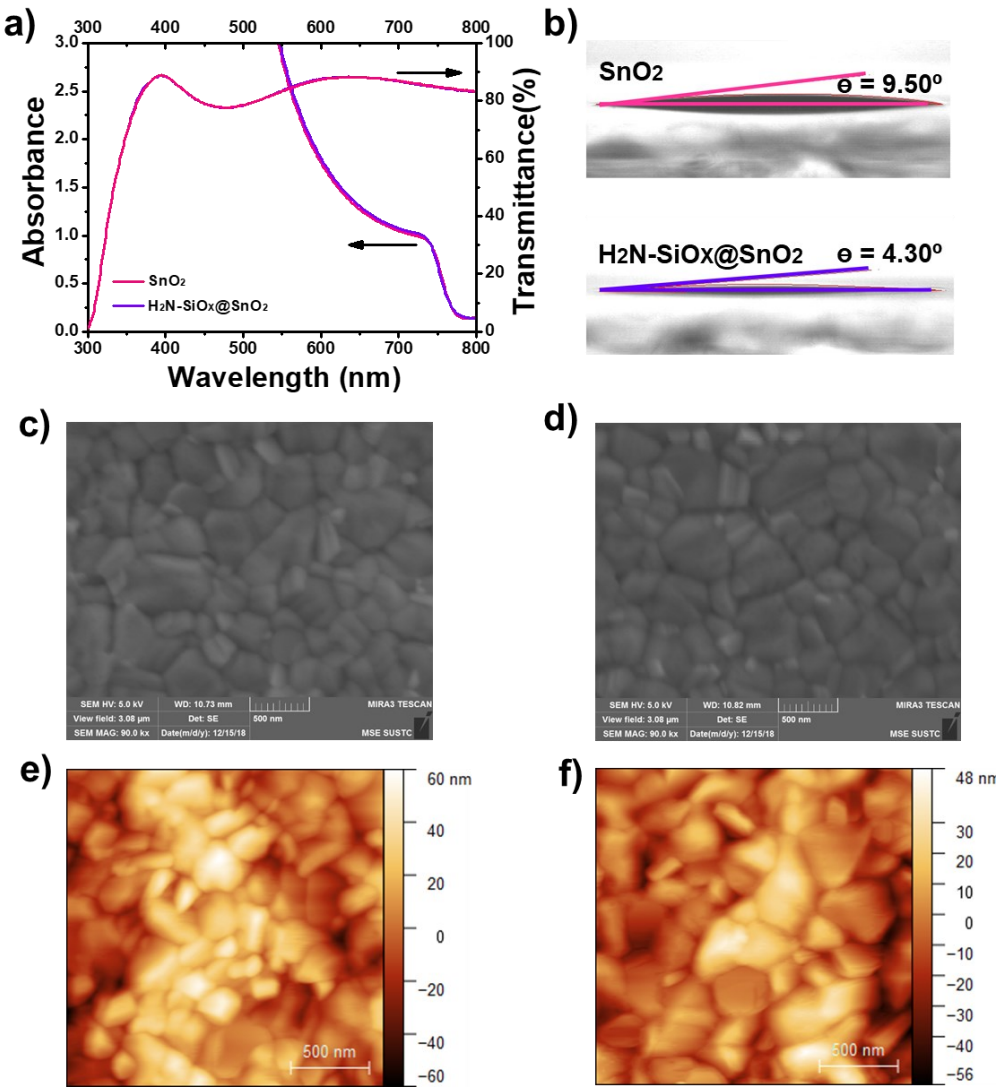

Figure 3.10 a) Transmittance spectroscopy of SnO_2 and H_2N-SiO_X@SnO_2 films prepared on ITO substrates and absorption spectroscopy of perovskite films deposited on SnO_2 and H_2N-SiO_X@SnO_2. b) Images of contact angle measurements for droplets of DMSO/DMF mixture solvent on SnO_2 and H_2N-SiO_X@SnO_2 substrates. SEM results of perovskite deposited on SnO_2 (c) and H_2N-SiO_X@SnO_2 (d). AFM results of perovskite deposited on SnO_2 (e) and H_2N-SiO_X@SnO_2 (f).

Maintaining sufficiently high transparency to minimize optical losses is an important criterion for ETL in n-i-p PSCs. From the transmittance spectrums shown in Figure 3.10a,

there is no obvious difference in 300–800 nm range, indicates that the modification of SnO_2 does not induce significant optical losses. The slight increase in absorbance when deposited on H_2N-SiO_X@SnO_2 probably comes from improved quality and coverage of perovskite (Figure 3.10c-f).

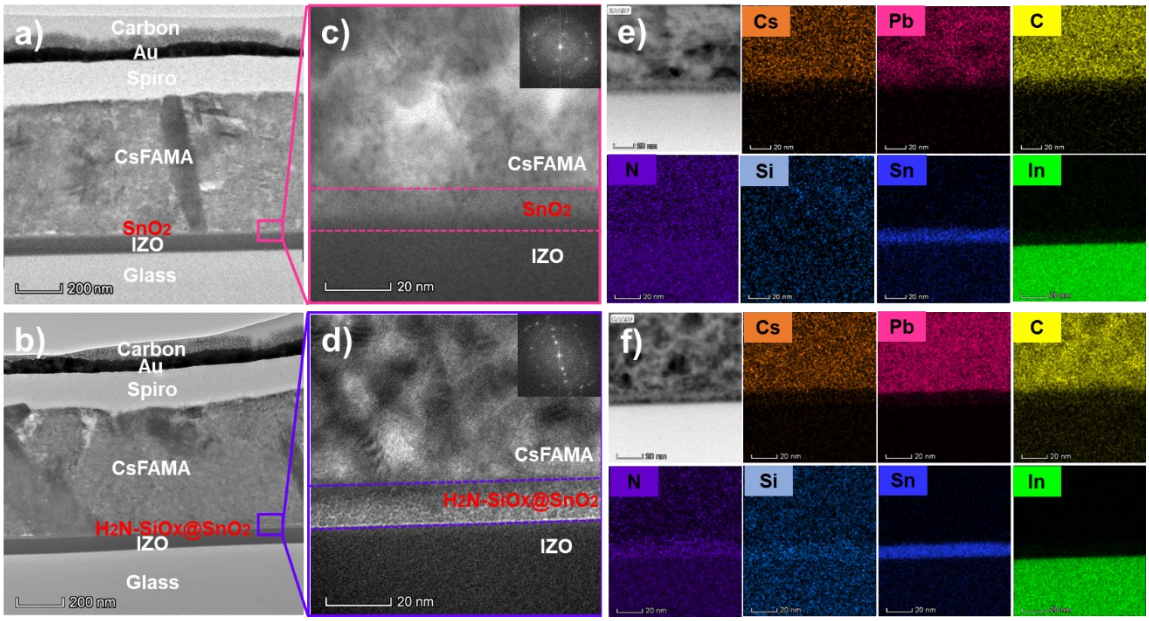

Figure 3.11 a, b) STEM images of PSCs with SnO_2 and H_2N-SiO_X@SnO_2, respectively. High magnification view of the interface and the FFT conversion view of perovskite at the interface based on SnO_2(c) and H_2N-SiO_X@SnO_2 (d), respectively. STEM and EDX mapping of the ETL/perovskite interface with SnO_2 (e) and H_2N-SiO_X@SnO_2 (f).

At the same time, cross-section SEM images of PSCs used SnO_2 and H_2N-SiO_X@SnO_2 as ETL are described (Figure 3.11a-b). The thickness of perovskite are ~ 600 nm for both ETLs. And SnO_2 and H_2N-SiO_X@SnO_2 ETLs are ~ 15 nm (Figure 3.11c-d). Obviously, the perovskite deposited on H_2N-SiO_X@SnO_2 shows higher crystallinity from the enlarged and FFT conversion view, demonstrate the modified ETLs favor the grown of perovskite film (Figure 3.11c-d). By STEM and EDX mapping, different layers include ETLs, perovskite layer, Spiro-OMeTAD layer and metal electrode are distinguished clearly. To identify the H_2N-SiO_X@SnO_2 layer, the interface between perovskite and ETLs have been zoom in (Figure 3.11e-f). Tiny amount of Si and N clearly detected in

consistent with Sn in Figure 3.11f differ from pure SnO_2, indicating the successful modification of SnO_2.

3.3.6 Characterization of device performance

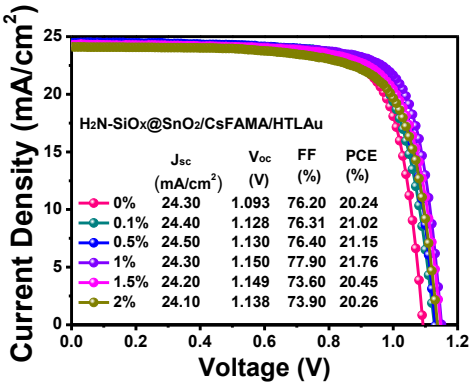

Figure 3.12 *J-V* curves of PSCs with SnO_2 modified by different vol % APTMS.

To optimize APTMS capping effect, PSCs with different APTMS percent (v/v) were fabricated. The results shown in Figure 3.12 indicated that the best device performance was obtained for 1% APTMS percent (v/v). In Figure 3.13, the champion cell's *J-V* curves in reverse scan of SnO_2 based (pink) and H_2N-SiO_X@SnO_2 based (violet) devices along with their corresponding parameters were shown, where the PCE remarkably increased from 20.24% to 21.76% with remarkable improvement of V_{oc}. Related photovoltaic parameters based on champion devices are also listed (Table 3.1).

Table 3.1 Related parameters of devices with SnO_2 and H_2N-SiO_X@SnO_2.

ETLs	Scan direction	J_{sc} [mA/cm^2]	J_{sc} by EQE [mA/cm^2]	V_{oc} [V]	*FF* [%]	PCE [%]
SnO_2	Reverse	24.16±0.62[a] (24.30)[b]	23.26	1.08±0.02[a] (1.09)[b]	74.67±2.43[a] (76.20)[b]	19.48±0.66[a] (20.18)[b]
	Forward	24.20		1.07	74.90	19.39
H_2N-SiO_X@SnO_2	Reverse	24.22±0.28[a] (24.30)[b]	23.41	1.13±0.04[a] (1.15)[b]	75.90±2.10[a] (77.90)[b]	20.77±0.92[a] (21.77)[b]
	Forward	24.30		1.14	77.10	21.36

a) Averaged values; b) The values corresponding to the champion devices.

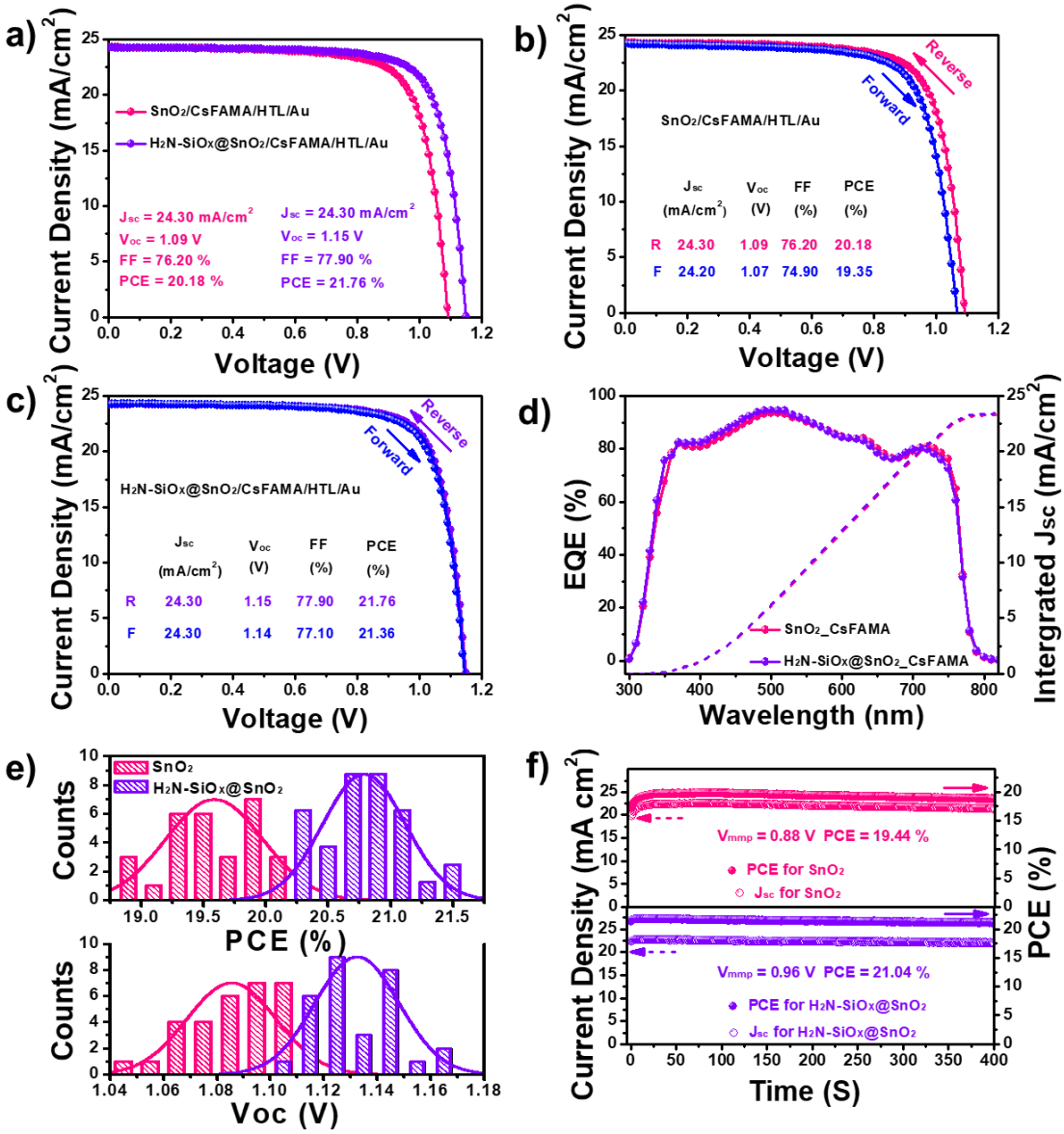

Figure 3.13 a) *J-V* curves in reverse scan of the optimal devices with SnO_2 and H_2N-SiO_X@SnO_2. b, c) Hysteresis characteristics of each optimal devices with SnO_2 and H_2N-SiO_X@SnO_2, respectively. d) EQE spectrum and their corresponding integrated J_{sc} for each device. e) Statistics distribution of V_{oc} and PCE based on SnO_2 (pink) and H_2N-SiO_X@SnO_2 (violet). f) Stabilized current and power output as a function of the time.

Figure 3.13b-c suggested that H_2N-SiO_X@SnO_2-based devices exhibited considerably weaker hysteresis behavior compared to SnO_2-based device. The reduced hysteresis was calculated quantified based on the method described in previous reports (Jiang et al., 2017). The *H*-index decreases remarkably from 4.40% to 1.38% after APTMS capping, largely owing to decreased surface charge traps of H_2N-SiO_X@SnO_2 (Tu et al., 2019). The EQE

spectra (Figure 3.13d) of each champion device show that the integrated J_{sc} values increased slightly after APTMS capping (from 23.26 to 23.41 mA/cm^2), which could original from the much more suitable energy level and higher film quality. The improved PCE mainly owing to the increased V_{oc} (Figure 3.13e) results from the shift in work function and suppressed recombination (Azmi, Hadmojo, et al., 2018). MPPT was performed to evaluate the stabilized power output (Figure 3.13f). Here, bias of 0.88 V and 0.96 V were applied to SnO_2 and H_2N-SiO_X@SnO_2-based PSCs, respectively. The optimal PSCs yielded a stabilized PCE of 19.44% for SnO_2 and 21.44% for H_2N-SiO_X@SnO_2, which were recorded after 300 s light soaking and show comparable PCE to the fresh *J-V* curves.

3.3.7 Characterization of charge recombination

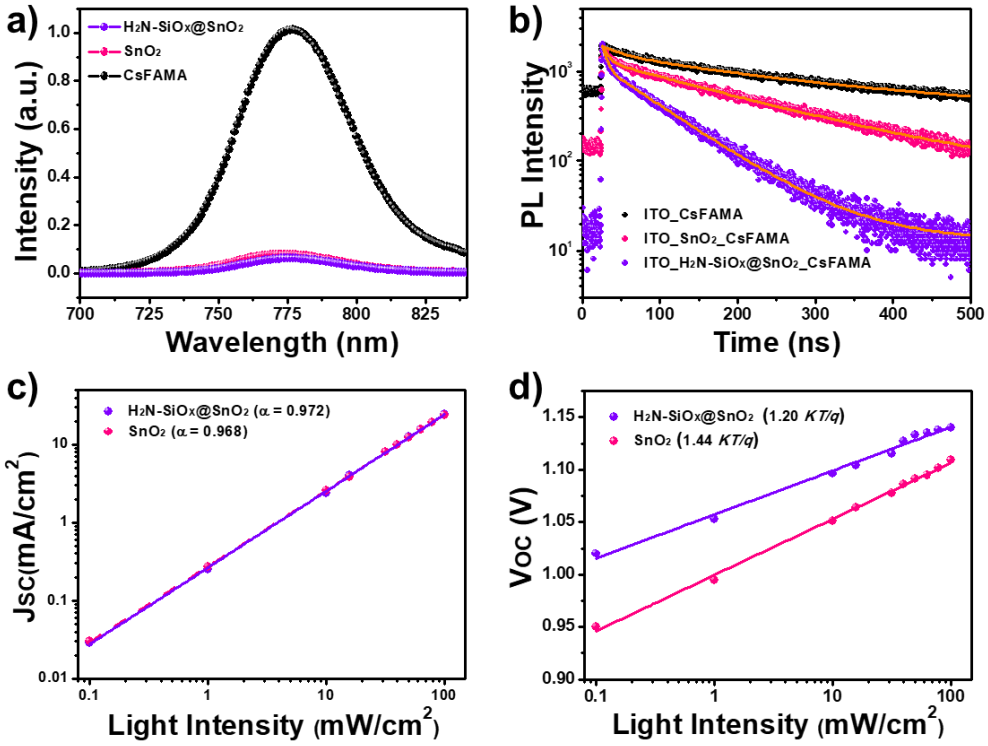

Figure 3.14 a) PL spectra of perovskite based on SnO_2 and H_2N-SiO_X@SnO_2. b) TRPL of perovskite based on SnO_2 and H_2N-SiO_X@SnO_2. c, d) J_{sc} and V_{oc} versus irradiation intensity of devices with solid lines denoting for linear fittings, respectively.

Subsequently, the underlying reason for the increased V_{oc} and PCE here after APTMS modification was further investigated. Firstly, steady-state PL and TRPL tests were conducted to reveal the impacts of APTMS modification on the interface charge extraction. As Figure 3.14a shown, more efficient quenching of $H_2N\text{-}SiO_X@SnO_2$ indicates more efficient electron extraction. Figure 3.14b shows the fitted curves where the faster decay constant τ_1 represents charge extraction. The lifetime after optimization significantly decreased from 8.38 ns to 5.07 ns, implying the improved electron extraction ability which may reduce the probability of recombination. To further investigated the charge recombination, *J-V* curves at different illumination intensity have been recorded. In the case of J_{sc} (Figure 3.14c), the slopes (α) of SnO_2 (0.968) and $H_2N\text{-}SiO_X@SnO_2$ (0.972) approaching to 1, demonstrating the negligible bimolecular recombination under short-circuit condition (Azmi, Hadmojo, et al., 2018). Differ from J_{sc}, the relationship between V_{oc} and light intensity is correlated with the trap-assisted recombination. As Figure 3.14d shown, a slope of 1.20 kTq^{-1} was estimated from the $H_2N\text{-}SiO_X@SnO_2$ based device, lower than 1.44 kTq^{-1} (SnO_2 based device), suggests an obvious rap-assisted SRH recombination reduction in PSCs, consistent with the increase in V_{oc}. The SRH recombination reduction could occur due to the passivation of the traps after the APTMS capping, leading to suppressed *J-V* hysteresis and improved V_{oc}.

3.3.8 Characterization of defect passivation

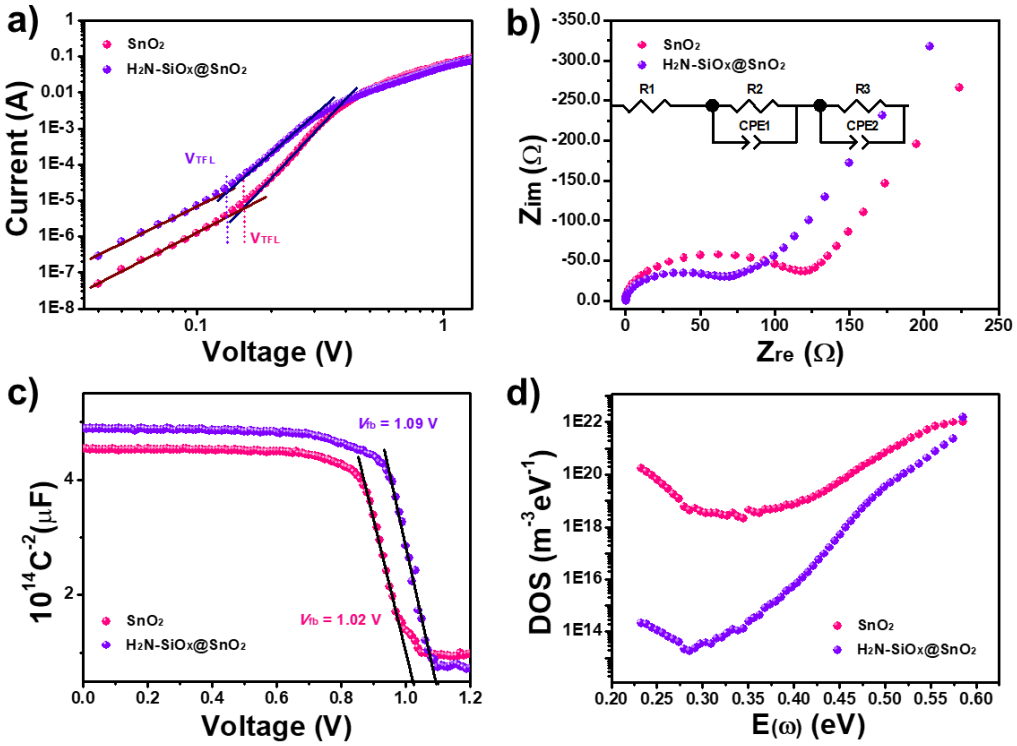

Figure 3.15 a) Dark *J-V* curves based on ITO/SnO_2 or H_2N-SiO_X@SnO_2/ perovskite/PCBM/BCP/Ag structure. b) Nyquist plots of devices with SnO_2 and H_2N-SiO_X@SnO_2 in dark. c) Mott-Schottky plots for devices with SnO_2 and H_2N-SiO_X@SnO_2 at 10 kHz. d) DOS results of devices based on SnO_2 and H_2N-SiO_X@SnO_2.

To further verify the defect passivation after formation of H_2N-SiO_X@SnO_2, the electron-only PSCs based on ITO/SnO_2 or (SiO_X@SnO_2)/perovskite/PCBM/BCP/Ag were prepared to reveal the optimization effect on trap state density of PSCs. Figure 3.15a shows *J-V* curves in dark. The linear correlation (dark red line) at low bias voltage refers to ohmic-type response. Current density dramatically increased (navy line) when exceed the kink point, indicating the traps were filled. The smaller V_{TFL} for the electron-only PSCs with H_2N-SiO_X@SnO_2 (0.13 V) suggests that the trap state is effectively passivated after APTMS capping, as expected from the enhancement of V_{oc} (Hou et al., 2018). EIS measurements was performed to further clarify the electron transport process and interface resistance in PSCs. The Nyquist plots with SnO_2 (pink) and H_2N-SiO_X@SnO_2 (purple)

are measured in dark with the equivalent circuit (Figure 3.15b). The high-frequency component refers to R_{tr} and low-frequency to R_{rec} (Xiong, Qin, et al., 2018). The measured results are summarized (Table 3.2). Since the perovskite/Spiro-OMeTAD interface is identical, R_{tr} and R_{rec} are only related to ETL/ perovskite interface. The smaller R_{tr} and larger R_{rec} based on H_2N-SiO_X@SnO_2 is beneficial for extracts electrons resists charge recombination, respectively, indicates the reduced charge recombination after APTMS capping (Yang et al., 2015).

Table 3.2 Transfer resistance (R_{tr}, Ω) and recombination resistance (R_{rec}, Ω) for SnO_2 and H_2N-SiO_X@SnO_2 systems.

ETL	R_{tr} (Ω)	R_{rec} (Ω)
SnO_2	120.3	750.9
H_2N-SiO_X@SnO_2	72.4	904.2

The interfacial properties were further investigated by capacitance-voltage (*C-V*) measurement. The Mott-Schottky curves were plotted from the *C-V* data and the built-in potential (V_{bi}) values can be estimated from the *x*-intercept (Figure 3.15c) (J.-W. Lee et al., 2015; Zheng et al., 2017). Owing to the decrease in W_F, the V_{bi} increased after APTMS capping, resulting in an extended depleted region, which not only suppresses the back transport of electrons, but also assists in the charge separation, charge transport and collection of photo-generated carriers (Chen et al., 2019). Based on the values of V_{bi}, trap densities was extracted from the thermal admittance spectroscopy analysis, where the DOS in PSCs will be analyzed effectively (Chen et al., 2019; Zheng et al., 2017). $\mathrm{DOS}(E_\omega) = -\frac{V_{bi}}{qW}\frac{dC}{d\omega}\frac{\omega}{KT}$ was applied to describe the distribution of trap state density, where W is the depletion width, V_{bi} is the built-in potential, k refers to Boltzmann constant, C is the capacitance, ω is angular frequency, q refers to elementary charge and T refers to temperature, W and V_{bi} are achieved from C^{-2}-V plots (Figure 3.15d). Here,

PSCs based on H_2N-SiO_X@SnO_2 shows lower trap density over the whole region compared to SnO_2 based PSCs. As the deeper trap region from 0.40 eV to 0.52 eV corresponds to surface traps and the shallower traps region from 0.35 eV to 0.40 eV corresponds to grain boundaries traps (Chen et al., 2017; Zheng et al., 2017), the lower trap density here indicates that the effectively defects passivation both at the interface and grain boundaries after optimization (Chen et al., 2017).

3.3.9 Characterization of stability

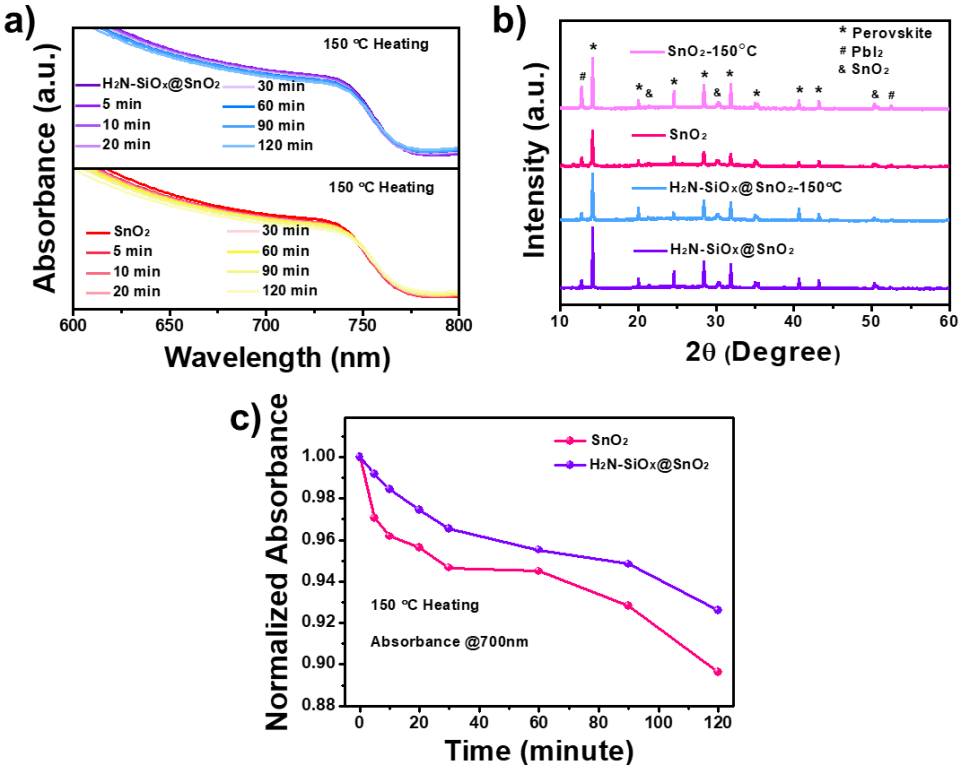

Figure 3.16 a) UV-vis absorption results of perovskite deposited on SnO_2 and H_2N-SiO_X@SnO_2 after thermal treatment at 150 ˚C with different time, respectively. b) Normalized absorbance at 700 nm for perovskite deposited on SnO_2 and H_2N-SiO_X@SnO_2, respectively. c) XRD spectra for prepared perovskite deposited on SnO_2 and H_2N-SiO_X@SnO_2 before or after thermal treatment at 150°C, respectively.

Stability is an important issue for future commercialization of PSCs. It is well known that interfacial degradation mainly results in the device instability. Thus, stable n-type heterojunction in planar PSCs plays a key role in final device stability. To examine the

defects passivation of H_2N-SiO_X@SnO_2, the stability of ETL/perovskite heterojunction based on SnO_2 and H_2N-SiO_X@SnO_2 in ambient condition was monitored. UV-vis absorption spectrum results are shown in Figure 3.16a. For comparation, samples are heated at 150 ˚C with time ranging from 5 min to 120 minutes. As the heating time increased, the absorption intensities of both samples decreased (Figure 3.16a), and the absorbance at 700 nm was normalized with an initial value to compare the thermal stability of each sample (Figure 3.16b). It was found that the perovskite deposited on the H_2N-SiO_X@SnO_2 maintained initial absorption better than that of SnO_2, this improved thermal stability implying the effective defect passivation after optimization. The retardation of the perovskite degradation was further valuated by XRD measurement (Figure 3.16c). All samples exhibited typical peaks at $2\theta = 14.1^\circ$, 28.4°, and 43.2°, which are assigned to (110), (220), and (330) lattice planes in perovskite. When samples were annealed at 150 ˚C for 120 minutes, the intensity of typical peak at 12.6˚, corresponding to PbI_2 (Conings et al., 2015), increased in both samples, in particular for SnO_2 system, confirming that perovskite deposited on H_2N-SiO_X@SnO_2 decomposed much slower at high temperatures. This result is well consistent with UV-vis absorption results.

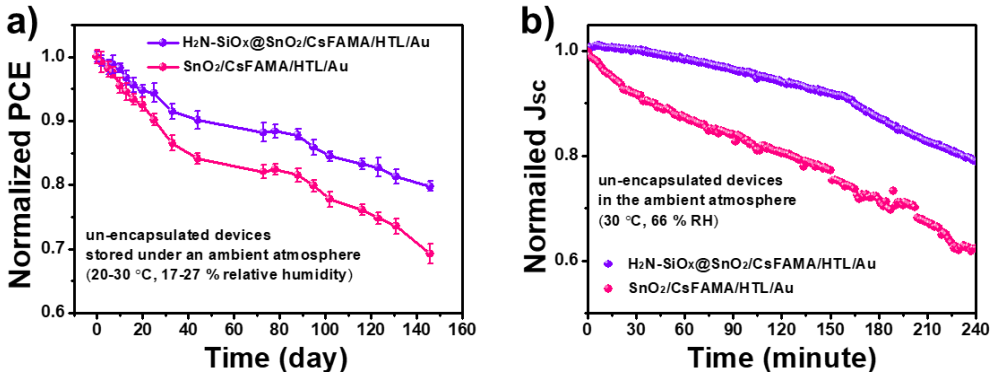

Figure 3.17 a) Normalized PCE for PSCs based on SnO_2 and H_2N-SiO_X@SnO_2 as a function of aging time. b) Stability test of the un-encapsulated devices with SnO_2 and H_2N-SiO_X@SnO_2 ETLs under continuous illuminated soaking in ambient condition.

The comparison of long-time stability was shown in Figure 3.17a, where an obvious improved stability has been achieved after optimization of SnO_2. 80% of the initial performance is maintained based on H_2N-SiO_X@SnO_2 after 140 days storage in ambient condition, while the reference cell degrades about 30%. At the same time, photo and electric field stability test shown in Figure 3.17b also indicated the improved stability, which can be attributed to highly stable ETL/perovskite heterojunction via the defect passivation and suppressed interfacial recombination after optimization of SnO_2 by APTMS.

3.4 Conclusions

In conclusion, a facile and effective method was proposed for the optimization of SnO_2 ETL by defect passivation, the successfully optimization was proven by FT-IR, XPS, STEM mapping, and UPS measurement, etc. Interestingly, the improved PCE based on H_2N-SiO_X@SnO_2 in our work is mainly attributed to the increased V_{oc}, boosts the conversion efficiency from 20.18% to 21.77% in PSCs with improved device stability. Comprehensive characterization results show that the significantly increase in V_{oc} and PCE could be attributed to the passivated defects and alleviated charge accumulation. Hence, our study demonstrates that stabilized the heterojunction by defect passivation of transport layer is a promising method to obtain high efficiency and stability PSCs.

4. Optimization of HTL by introduce dopants free HTMs

4.1 Introduction

Organic-inorganic hybrid PSCs based on SnO_2 have attracted extensive attentions and achieved remarkable progress in achieving conversion efficiencies that exceed ~23% (Abuhelaiqa et al., 2019; Gharibzadeh et al., 2019; Tu et al., 2019). PSCs is a likely candidate for future commercialization because of the native advantages of inorganic and stable SnO_2 molecules, which fit well into the PSCs. This harmonious combination makes suitable HTMs more and more important and increases concerns about the long-standing stability issue of PSCs (Kasparavicius, Magomedov, Malinauskas, & Getautis, 2018; Magomedov et al., 2018). As the currently popular HTM in current high conversion efficiency PSCs, Spiro-OMeTAD still suffers from severe instability due to the incorporation of necessary dopants such as Li-TFSI, which is highly sensitive to moisture, heat and even light (Cai et al., 2018; Hawash, Ono, & Qi, 2018; Urbani, de la Torre, Nazeeruddin, & Torres, 2019; Yin et al., 2019). At the same time, the low hole mobility and high synthesis costs of Spiro-OMeTAD would unavoidably impede its industrialization (Calió, Kazim, Grätzel, & Ahmad, 2016). Therefore, the exploration of efficient dopant-free HTMs with low synthesis costs, good reproducibility and high stability seems imperative for the rapid evolution of normal planar PSCs.

Among the promising candidates, small molecular HTMs have shown a huge potential based on their well-defined structures, good reproducibility and fine-tuned optoelectronic properties (Im et al., 2011). Observing the general principles for designing dopant-free small molecular HTMs (e.g., suitable energy levels, good film morphology, high chemical stability and hole mobility), donor-acceptor (D-A) type small molecules can be regarded

as a good candidate for dopant-free HTMs because the D-A molecular backbone features intramolecular charge transfer (ICT) characteristics and a high dipole moment, which could induce self-doping and a built-in potential to boost charge extraction (Li et al., 2016; Ok et al., 2018; Pham et al., 2018; Pham et al., 2019). Combined with the bis(4-methoxyphenyl)amine unit identified as the preferential hole-transporting moiety to improve charge mobility at the molecular level (Pham et al., 2019; Pham et al., 2018; Pham et al., 2019) and thiophene units, which are expected to reinforce intermolecular interactions and π-π stacking to achieve high conductivity (Pham et al., 2017), a novel D-A type molecular MPA-BTTI was designed and synthesized, but its role in PSCs is still unclear.

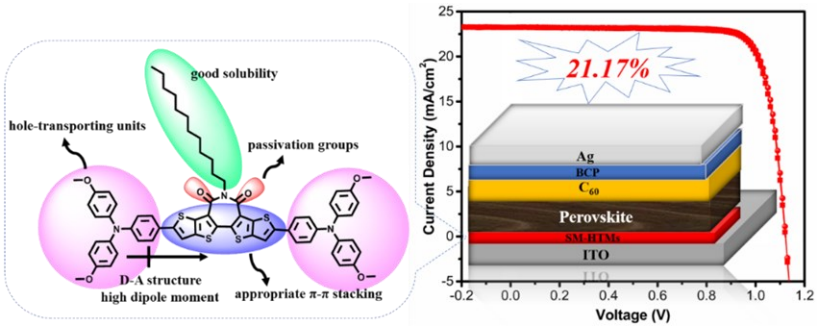

Figure 4.1 BTTI based HTL for inverted PSCs with efficiency exceeding 21% (Wang et al., 2019).

Fortunately, the good performance of devices that have adopted MPA-BTTI as the HTM in inverted planar PSCs suggests its hole transport ability and its suitable electronic structure for band level alignment in devices (Wang et al., 2019), indicating that it can be used to replace Spiro-OMeTAD in the promising normal planar PSCs. Differing from the case of inverted planar devices, a uniform and dense film of dopant-free HTMs deposited on the perovskite absorber layer is a prerequisite. As is well known, the molecular packing behavior plays a critical role in the film-forming behavior, the intrinsic hole mobility in

the finished film and the establishment of a good interfacial contact. Hence, tailoring the molecular structure is indispensable to optimizing the molecular packing behavior in the film state. Because the alkyl side-chains of organic molecules are often critical to solubility in specific solvents and the subsequent molecular packing behavior in the course of film-forming when the solvents are evaporated (Liu, Zhang, & Zhang, 2018; Truong et al., 2019; Zimmermann et al., 2016), side-chain engineering seems to be an effective strategy to modify the molecular packing, film morphology, charge mobility and resultant device performance. Therefore, we developed three derivatives of MPA-BTTI with different alkyl chains (i.e., n-dodecyl, n-octyl, n-hexyl, named as BTTI-C12, BTTI-C8 and BTTI-C6, respectively) while keeping the initial molecular backbone to investigate side chains effect on HTL.

4.2 Experimental section

4.2.1 Materials

Anhydrous solvents DMF, DMSO, and CB were purchased from Acros Organics. Spiro-OMeTAD, Li-TFSI, FK209 and tBP were achieved from Xi'an Polymer Light Technology Corp. CsI was achieved from Sigma-Aldrich. FAI and MABr were achieved from Great Cell Solar Ltd (Australia). $PbBr_2$ and PbI_2 were obtained from TCI. The SnO_2 colloid precursor was purchased from Alfa Aesar. All reagents and chemicals are purchased commercially and used without further purification unless otherwise stated. Solvents were purified by standard methods and dried if necessary.

4.2.2 Syntheses and characterization of BTTI HTMs

General synthetic procedures for compound 1, 3 and 5, which follow our previous work (Rong et al., 2018).

To a flask was charged with bithiophene anhydride, n-dodecylamine or n-octylamine or

hexylamine, 4-dimethylaminopyridine, and 1,4-dioxane, then reflux for 12 hours. Then injected acetic anhydride in one portion and reflux for another 3 hours. All solvents were removed after cooling to room temperature and purified the product with column chromatography (silica gel, petroleum ether:CH_2Cl_2 = 2:1 as the eluent) affording the corresponding target compound 1, 3 and 5.

General synthetic procedures for compound 2, 4 and 6, which follow our previous work (Rong et al., 2018).

Dissolved compound 1 or Compound 3 or Compound 5 in $CHCl_3$ and added N-bromosuccinimide into DMF solution. Then stirred for 12 hours before pour into water. Extracted the mixture with $CHCl_3$ and dried the organic layer by anhydrous Na_2SO_4. After solvent evaporation, purified the residue with column chromatography (silica gel, petroleum ether:CH_2Cl_2 = 3:1 as the eluent) to afford the corresponding target compound 2, 4 and 6.

General synthetic procedures for BTTI-C12, BTTI-C8 and BTTI-C6, which follow our previous work (Rong et al., 2018).

To a flask was charged with compound 2 or compound 4 or compound 6, $Pd(PPh_3)_4$, K_2CO_3, H_2O, and THF, reflux for 24 hours under nitrogen atmosphere. Extracted the mixture with CH_2Cl_2 after cooling to room temperature and dried the organic layer with anhydrous Na_2SO_4. After solvent evaporation, purified the residue with column chromatography (silica gel, petroleum ether:CH_2Cl_2 = 2:1 as the eluent) to afford the corresponding target HTMs BTTI-C12, BTTI-C8 and BTTI-C6.

4.2.3 Preparation of SnO_2 films

Diluted SnO_2 precursor by H_2O to 2.67% before use. Spin coating (5000 r.p.m., 30s) the diluted solution to achieve SnO_2 films and anneal at 180 ˚C for 30 minutes in ambient

air.

4.2.4 PSCs Device Fabrication

Firstly, ITO was cleaned with detergent, deionized water, ACN and IPA, sequentially. Following, deal by UV O_3 for 30 minutes. Then, SnO_2 was spin coated. P perovskite precursor was achieved by mixing MABr, FAI, $PbBr_2$ and PbI_2 in DMF/DMSO (volume ratio is 4:1) with the mole ratio of FA/MA and I/Br maintained at 0.87/0.13, and the mole concentration of PbI_2 kept at 1.1 M. After stirring for 1 hour at 60 ˚C, 35 μL of CsI (2 M dissolved in DMSO) was injected and stirred for another 1 hour. Spin coating (2000, 10s and 6000, 20s) the precursor solution and antisolvent (100 μL CB) was dropped 10 s prior to the end. After the perovskite growth, the Spiro-OMeTAD/CB (72.3 $mg \cdot mL^{-1}$) solution with tBP (28.5 μL), Li-TFSI/ACN (17.8 μL, 520 $mg \cdot mL^{-1}$) and FK209/ACN (30μL, 300 $mg \cdot mL^{-1}$) was spin coated (4,000 r.p.m., 30 s). 25 mg/mL BTTI HTMs in CB were spin coated and annealed for 10 minutes. Finally, Au was deposited by thermal evaporation method.

4.2.5 Characterization

The ^1H Nuclear Magnetic Resonance (NMR) results were obtained on the 400 MHz NMR spectrometer (Bruker Ascend). Matrix-Assisted Laser Desorption/Ionization Time-of-Flight (MALDI-TOF) mass spectra were performed on an AXIMA CFR MS apparatus (COMPACT) using 2-[(2E)-3-(4-tertbutylphenyl)-2-methylprop-2-enylidene] malononitrile (DCTB) as the matrix. Elemental analyses (EA) of the compounds were performed at Shenzhen University (Shenzhen, Guangdong, China). UV-Vis absorption spectrums of solutions (in THF) and thin films were recorded on a Shimadzu UV-3600 UV-vis-NIR spectrophotometer. Cyclic Voltammetry (CV) characterizations were performed using the CHI760E voltammetric workstation under argon atmosphere with a

N_2-saturated solution of 0.1 M tetra-n-butyl ammonium hexafluoro phosphate (Bu_4NPF_6) in CH_2Cl_2 as the supporting electrolyte. Thermogravimetric (TGA) tests were performed with TGA 1 STARe System apparatus (METTLER TOLEDO) at 10 ˚C minute^{-1} heat ramp under N_2. Differential Scanning Calorimetry (DSC) results were achieved by a differential scanning calorimetry (Mettler, STARe, heating ramp: 10 ˚C minute^{-1}) in nitrogen. Hole mobilities of BTTI HTMs were measured using the SCLC method. The structure of ITO/PEDOT:PSS/HTMs/MoO_3/Ag was used for the hole-only devices. The SCLC mobility were calculated based on the MOTT-Gurney equation: $J = \frac{9}{8}\varepsilon_0\varepsilon_r\mu\frac{V^2}{d^3}$, Where J refers to the current density, ε_0 refers to the permittivity of empty space, ε_r refers to the relative dielectric constant of BTTI HTMs, μ refers to the hole mobility, d refers to the thickness of HTMs, V refers to the internal voltage in the device, and $V = V_{appl}$-V_{bi} where V_{appl} is the applied voltage and V_{bi} refers to the built-in voltage resulting from the relative work function difference between the two electrodes and can be neglected. Morphology was achieved by SEM (TESCAN MIRA3), cross-section morphology, EDX mapping and STEM images were realized by TEM (FEI Talos) and FIB (Helios Nanolab 600i). AFM-based experiments were measured with AFM (MFP-3D-BIO, Asylum Research, USA). 2D Grazing Incidence Wide-Angle X-ray Scattering (2D GIWAXS) results were achieved by PLS-II 9A U-SAXS beam line (Pohang Accelerator Laboratory, Korea). *J-V* measurements were performed in in ambient condition (27 ºC, 75% RH) with a Keithley 2400 sourcemete. Illumination was provided by solar simulator (Oriel Sol3A, AM1.5G spectrum, calibrated by KG-5 Si diode). All PSCs were measured with 10 ms delay time. EQE characterization was carried out by Enli Tech (Taiwan). PL and TRPL spectrums were achieved with Spectrofluorometer (FS5, Edinburgh, 405 nm pulsed laser).

4.3 Results and Discussion

4.3.1 Preparation and characterization of BTTI HTMs

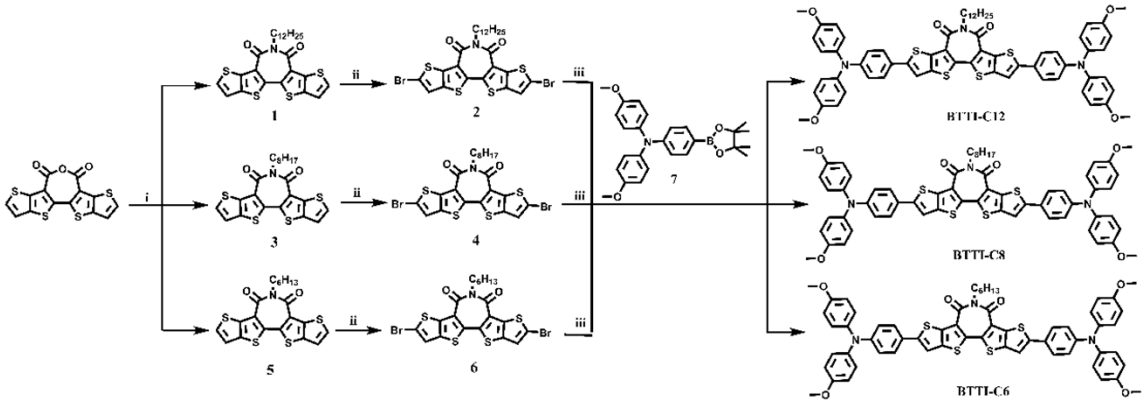

Scheme 4.1 Chemical structures and detailed synthetic routes to BTTI-C12, BTTI-C8 and BTTI-C6. Reagents and conditions: i) 1-dodecylamine (for BTTI-C12) or n-octylamine (for BTTI-C8) or n-hexylamine (for BTTI-C6), 4-dimethylaminopyridine, 1,4-dioxane, acetic anhydride, reflux; ii) N-bromosuccinimide, DMF, $CHCl_3$, room temperature.; iii) Compound 7, $Pd(PPh_3)_4$, K_2CO_3, THF, H_2O, reflux.

The synthetic route for these small molecule HTMs can be found in Scheme 4.1. By utilizing bithiophene-based anhydride as the starting material, three steps incorporating imidization, bromination and Suzuki coupling could result in BTTI-C6, BTTI-C8 and BTTI-C12 with moderate overall yields. Note that the synthetic procedures for these HTMs are nearly the same as those used in a previous study (Y. Wang et al., 2019), except that alkylamine molecules with different lengths were used to enable the side-chain engineering of such HTMs. The chemical structures of these HTMs (shown in Scheme 4.1) were well established by ^{1}H NMR, ^{13}C NMR, MALDI-TOF mass spectrometry, and EA, as results shown below.

Compound 1: ^{1}H NMR (400MHz, $CDCl_3$): δ 7.63 (d, J = 5.3 Hz, 2H), 7.30 (d, J = 5.4 Hz, 2H), 4.43-4.36 (m, 2H), 1.85-1.78 (m, 2H), 1.51-1.28 (m, 18H), 0.90 (t, J = 6.8 Hz, 3H).

Compound 2: ^{1}H NMR (400MHz, $CDCl_3$): δ 7.22 (s, 2H), 4.32-4.29 (m, 2H), 1.80-1.72

(m, 2H), 1.46-1.28 (m, 18H), 0.89 (t, J = 6.8 Hz, 3H).

BTTI-C12: ^{1}H NMR (400MHz, $CDCl_3$): δ 7.43 (d, J = 8.7 Hz, 4H), 7.24 (s, 2H), 7.07 (d, J = 8.9 Hz, 8H), 6.89 (d, J = 8.7 Hz, 4H), 6.86 (d, J = 9.0 Hz, 8H), 4.39-4.35 (m, 2H), 3.83 (s, 12H), 1.86-1.82 (m, 2H), 1.50-1.28 (m, 18H), 0.90 (t, J = 6.8 Hz, 3H). ^{13}C NMR (400MHz, $CDCl_3$): δ 160.12, 156.23, 150.87, 148.86, 141.03, 140.19, 138.51, 135.05, 127.07, 126.35, 125.57, 124.54, 119.64, 114.79, 111.98, 55.48, 46.42, 31.96, 29.80, 29.72, 29.68, 29.59, 29.40, 27.62, 27.47, 22.72, 14.16. MALDI-TOF MS: calculated for: $C_{66}H_{63}N_3O_6S_4$ 1121.3, found: 1121.3 [M^+]. Elemental Analysis: C, 70.62; H, 5.66; N, 3.74; S, 11.42, Found: C, 70.51; H, 5.71; N, 3.70; S, 11.40.

Compound 3: ^{1}H NMR (400MHz, $CDCl_3$): δ 7.61 (d, J = 5.3 Hz, 2H), 7.22 (d, J = 5.4 Hz, 2H), 4.37-4.35 (m, 2H), 1.87-1.80 (m, 2H), 1.52-1.28 (m, 10H), 0.90 (t, J = 6.8 Hz, 3H).

Compound 4: ^{1}H NMR (400MHz, $CDCl_3$): δ 7.22 (s, 2H), 4.36-4.34 (m, 2H), 1.88-1.80 (m, 2H), 1.51-1.28 (m, 10H), 0.90 (t, J = 6.8 Hz, 3H).

BTTI-C8: ^{1}H NMR (400MHz, $CDCl_3$): δ 7.43 (d, J = 8.7 Hz, 4H), 7.22 (s, 2H), 7.06 (br, 8H), 6.88-6.85 (m, 12H), 4.39-4.34 (m, 2H), 3.84 (s, 12H), 1.87-1.82 (m, 2H), 1.50-1.27 (m, 10H), 0.90 (t, J = 6.8 Hz, 3H). ^{13}C NMR (400MHz, $CDCl_3$): δ 160.32, 156.13, 150.89, 148.90, 141.02, 140.20, 138.50, 135.03, 127.08, 126.35, 125.59, 124.54, 119.65, 114.80, 111.99, 55.50, 46.31, 31.87, 29.40, 29.32, 27.75, 27.36, 22.70, 14.15. MALDI-TOF MS: calculated for: $C_{62}H_{55}N_3O_6S_4$ 1066.3, found: 1066.3 [M^+]. Elemental Analysis: C, 69.83; H, 5.20; N, 3.94; S, 12.03, Found: C, 69.89; H, 5.31; N, 3.90; S, 12.20.

Compound 5: ^{1}H NMR (400MHz, $CDCl_3$): δ 7.62 (d, J = 5.3 Hz, 2H), 7.23 (d, J = 5.4 Hz, 2H), 4.39-4.35 (m, 2H), 1.87-1.80 (m, 2H), 1.51-1.41 (m, 6H), 0.90 (t, J = 6.8 Hz, 3H).

Compound 6: ^{1}H NMR (400MHz, $CDCl_3$): δ 7.24 (s, 2H), 4.38-4.35 (m, 2H), 1.88-1.80 (m, 2H), 1.50-1.41 (m, 6H), 0.90 (t, J = 6.8 Hz, 3H).

BTTI-C6: ^{1}H NMR (400MHz, $CDCl_3$): δ 7.44 (d, J = 8.7 Hz, 4H), 7.25 (s, 2H), 7.08 (d, J = 8.9 Hz, 8H), 6.91-6.86 (m, 12H), 4.39-4.36 (m, 2H), 3.83 (s, 12H), 1.88-1.82 (m, 2H), 1.49-1.40 (m, 6H), 0.90 (t, J = 6.8 Hz, 3H). 13C NMR (400MHz, $CDCl_3$): δ 160.33, 156.11, 150.90, 148.89, 141.04, 140.22, 138.51, 135.03, 127.09, 126.36, 125.60, 124.52, 119.63, 114.81, 111.98, 55.51, 46.33, 31.88, 29.41, 27.36, 22.70, 14.15. MALDI-TOF MS: calculated for: $C_{60}H_{51}N_3O_6S_4$ 1038.3, found: 1038.3 [M^+]. Elemental Analysis: C, 69.41; H, 4.95; N, 4.05; S, 12.35, Found: C, 69.38; H, 4.90; N, 3.99; S, 12.20.

At the same time, it was found that the solubility decreased with the shortening of the side chain. As such, the trial of synthesizing HTMs with even shorter side chains such as C4 failed mainly because of the poor solubility of intermediates, results in lower purification rate and a much lower yield. Despite this, BTTI-C6 can still be dissolved in CB with a solubility ~30 mg/mL, which ensures the solution processability of these HTMs.

4.3.2 Characterization of photo-electricity properties

Table 4.1 The electrochemical, photophysical, hole mobility of the BTTI HTMs.

	$\lambda_{abs,sol}$ (nm) [a]	$\lambda_{abs,film}$ (nm) [a]	E_g^{opt} (eV) [b]	HOMO (eV) [c]	LUMO (eV) [d]	μ_h ($cm^2 V^{-1} s^{-1}$)	Conductivity (S cm^{-1})
BTTI-C6	342, 532	357,519	1.92	-5.25	-3.33	2.19×10^{-4}	3.02×10^{-5}
BTTI-C8	342, 532	357,521	1.92	-5.25	-3.33	2.08×10^{-4}	2.94×10^{-5}
BTTI-C12	343, 532	357,522	1.92	-5.24	-3.32	2.02×10^{-4}	2.79×10^{-5}

[a] Measured in THF solution with a concentration of 10^{-5} mol/L. [b] The absorption edge was estimated by equation: $E_g^{opt} = 1243 / \lambda_{onset}$ (eV). [c] $E_{HOMO} = -5.1-(E_{ox} - E_{1/2}\ (Fc/Fc^+))$. [d] $E_{LUMO} = -5.1-(E_{red} - E_{1/2}\ (Fc/Fc^+))$.

In Figure 4.2a, the absorption spectra of BTTI-C6, BTTI-C8 and BTTI-C12 in both solution and a solid-state film are very similar (also refer to Table 4.1). The low energy absorption band around 530 nm is ascribed to the ICT absorption due to the intrinsic D-A backbone of HTMs, while the absorption in the short wavelength region (< 400 nm) could

be attributed to the π–π* transition. The hypochromic shift located at the lower energy absorption band from the solution to the solid state film originates from *H*-aggregation, as reported previously in the literature (Jiang et al., 2019). It is noted that the degree of the hypochromic shift depends on the length of the side chain, with the largest blue shift (~ 13 nm) from BTTI-C6, implying a denser intermolecular stacking in the neat film.

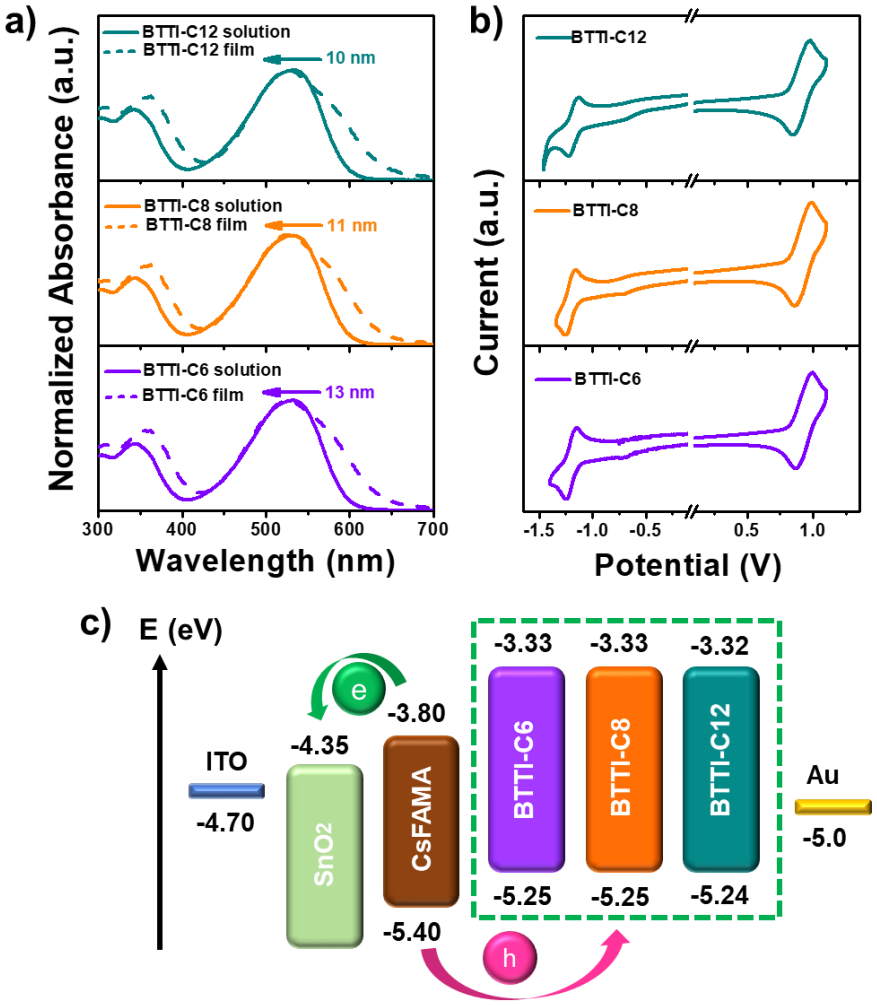

Figure 4.2 a) Absorption spectrums of the three BTTI HTMs both in the THF solution and thin films. d) Cyclic voltammetry curves of the three BTTI HTMs measured in dichloromethane, with F_c/F_c^+ added as an inner standard. c)The diagram of energy level for three BTTI HTMs.

From cyclic voltammograms of the three HTMs in Figure 4.2b, we obtained almost the same energy levels. When compared to perovskite, the observed shallower HOMO energy

and high-lying LUMO energy of these HTMs indicate a good capacity of hole injection and electron blocking (Figure 4.2c).

4.3.3 Characterization of physical properties

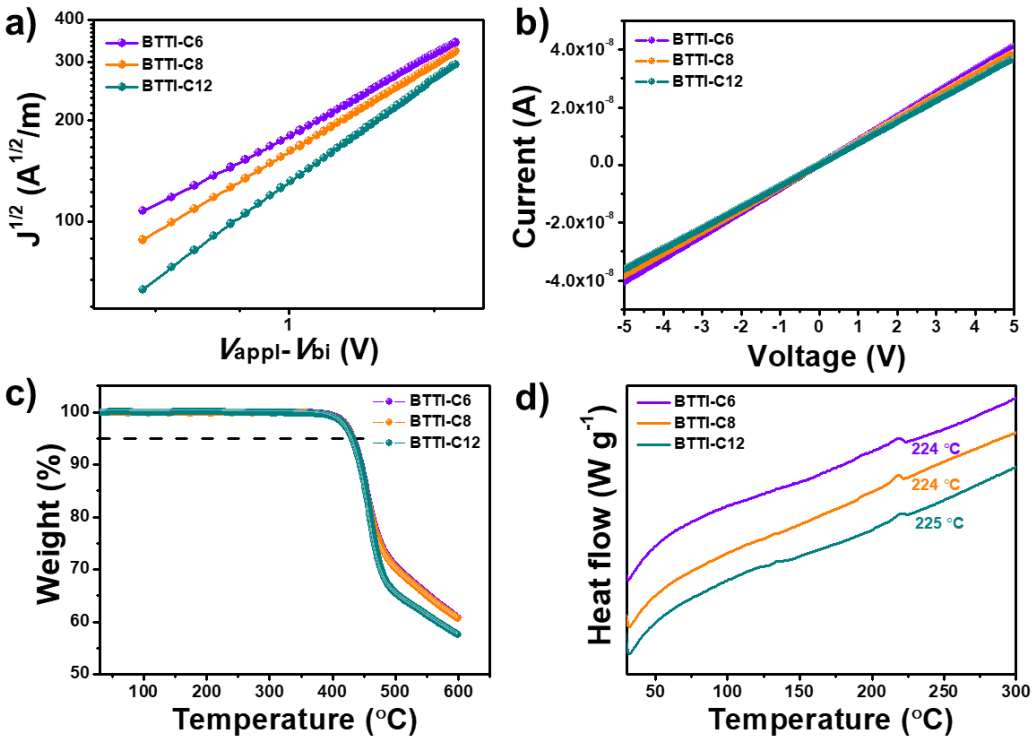

Figure 4.3 a) Measured hole mobility of the three BTTI HTMs, based on ITO/PEDOT:PSS/BTTI HTMs/MoO_3/Ag, with the SCLC method. b) Conductivity measured for the different BTTI HTMs films. c) TGA and d) DSC curves for different BTTI HTMs.

SCLC method was introduced to explore the hole mobility (μ_h) of these HTMs and Figure 4.3a shows the results. The values of these HTMs in pristine films are 2.02×10^{-4} cm^2 $V^{-1}s^{-1}$ (BTTI-C12), 2.08×10^{-4} cm^2 $V^{-1}s^{-1}$ (BTTI-C8) and 2.19×10^{-4} cm^2 $V^{-1}s^{-1}$ (BTTI-C6), which are higher than that of Spiro-OMeTAD (2.13×10^{-5} cm^2 V^{-1} s^{-1}) (Huang et al., 2016). BTTI-C6 with highest mobility indicates a more strengthened molecular packing in the neat film when shortening the side chain length of the BTTI HTMs. Similarly, the conductivity values of the undoped films are 2.79×10^{-5} S cm^{-1} (BTTI-C12), 2.94×10^{-5} S cm^{-1} (BTTI-C8) and 3.02×10^{-5} S cm^{-1} (BTTI-C6), respectively

(Figure 4.3b), which are comparable to the value of undoped Spiro-OMeTAD film (~10^{-5} S cm^{-1}) (Pham et al., 2017). The small increase in the conductivity with a decreasing chain length could be the result of the decreased intermolecular distances (Lin et al., 2018), and could make an improvement in the *FF* of PSCs. The thermal properties of the BTTI HTMs were investigated with TGA and DSC. The TGA results show that the decomposition temperatures corresponding to a 5% weight loss (T_{ds}) of the BTTI HTMs are all nearly 440 ˚C (Figure 4.3c), which is high enough to withstand the temperatures encountered during the fabrication of PSCs (100 ˚C) . Similarly, the glass transition temperatures (T_g) of different BTTI HTMs are all detected around 224 ˚C (Figure 4.3d), higher than 121 ˚C (Spiro-OMeTAD) (Yang et al., 2017). The good thermal stability and high T_g highlight their potential thermal stability in PSCs.

4.3.4 Characterization of film morphology

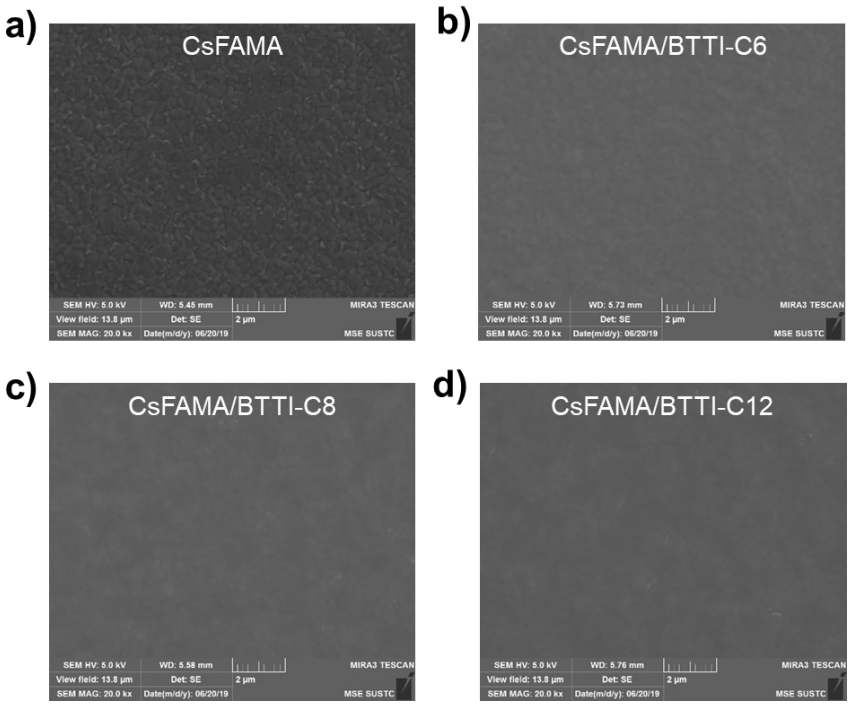

Figure 4.4 SEM images of different BTTI HTMs capping on the perovskite layers.

We first studied the impact of different side chains on the film morphology by SEM.

The results show us that it is hard to distinguish the film morphologies from each other with the SEM images (Figure 4.4).

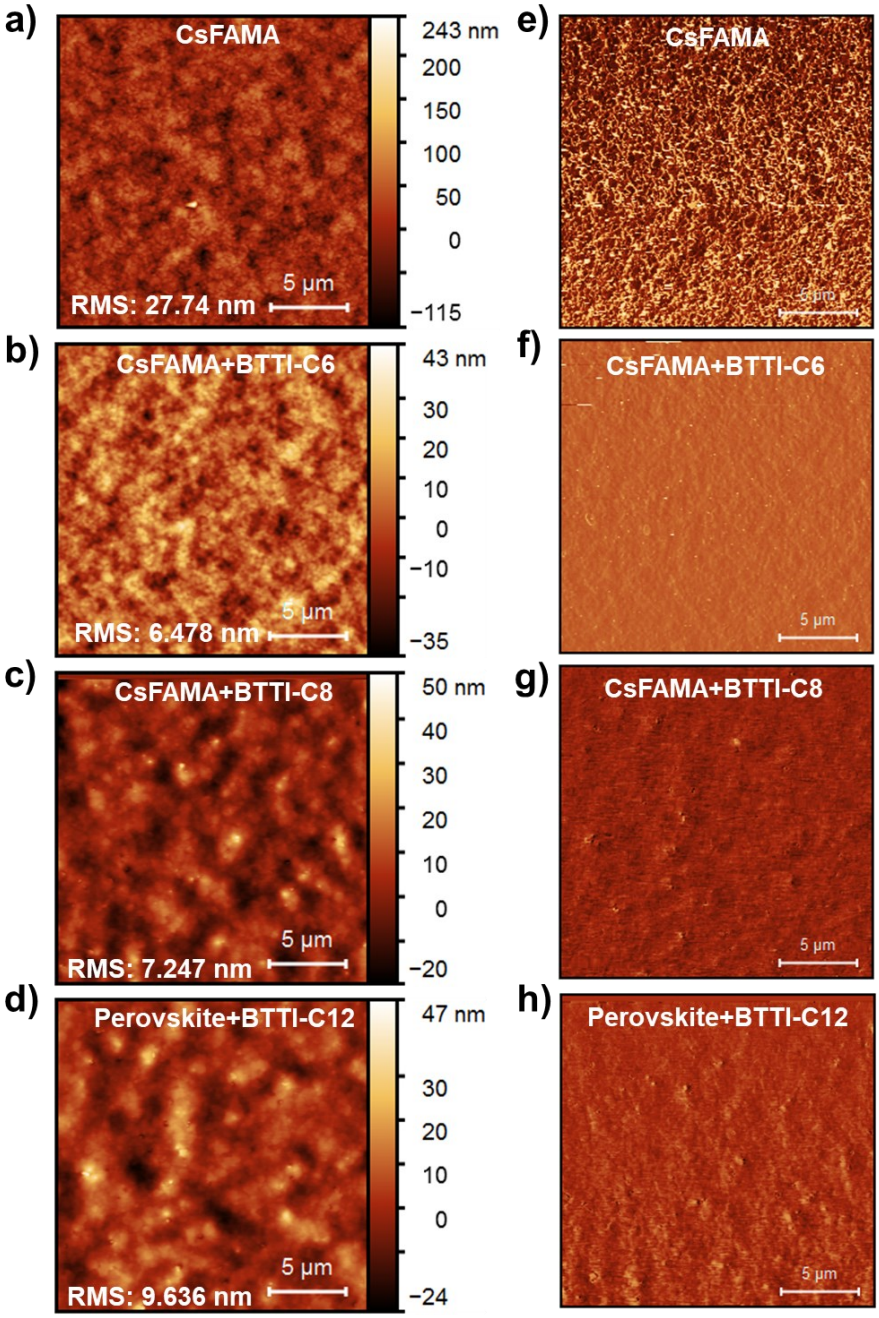

Figure 4.5 Topographic AFM images (a-d) and phase images (e-h) of the different BTTI HTMs capping on perovskite.

Then, AFM was introduced here. By comparison, the topographic AFM images show that the root means square (*RMS*) roughness of the perovskite layers decreased sharply

because of capping with the HTMs, rendering a uniform and pinhole-free HTM layer in the device. Specifically, the *RMS* value was gradually reduced from ~ 9.6 nm (BTTI-C12) to ~ 7.2 nm (BTTI-C8) and then to ~ 6.5 nm (BTTI-C6) (Figure 4.5), indicating the formation of a smoother film after employing a shorter side chain BTTI HTM, which may lead to a good perovskite/HTM contact and/or HTM/anode electrode, results in an improved FF of PSCs (Lee et al., 2019; Wang et al., 2018).

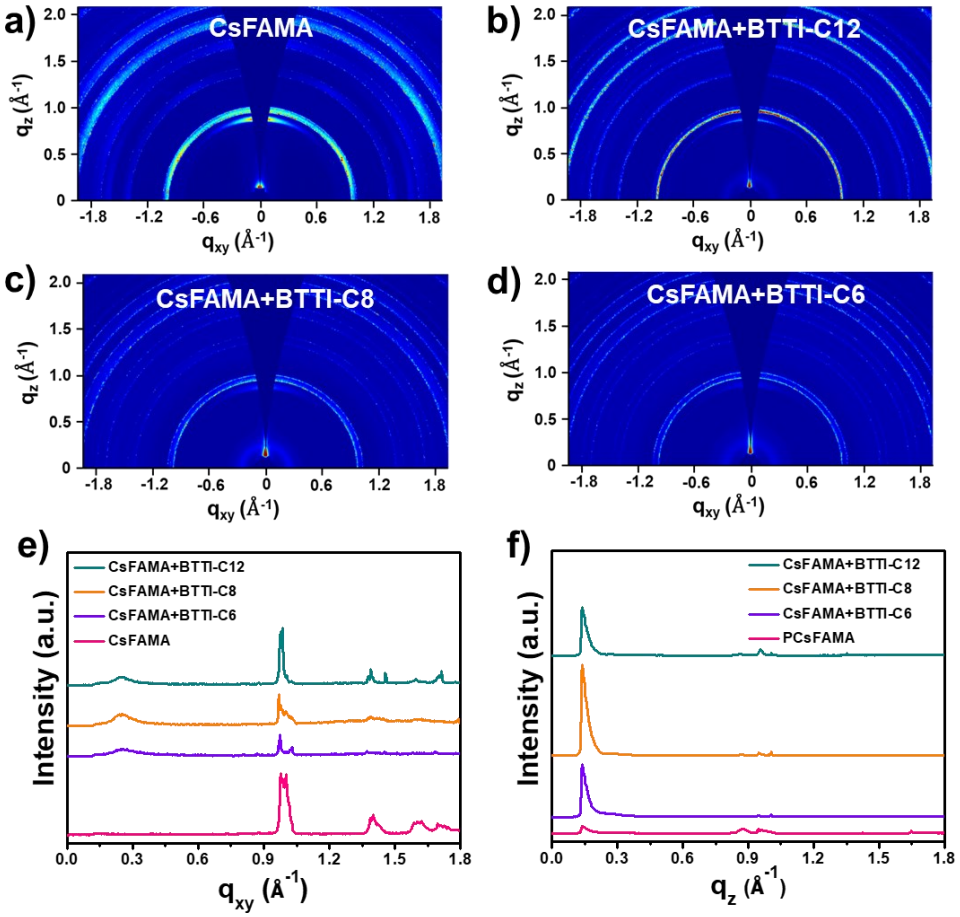

Figure 4.6 a-d) 2D GIWAXS patterns for perovskite, perovskite+BTTI-C6, perovskite+BTTI-C8 and perovskite+BTTI-C12, respectively. The line-cut profiles along the in-plane (e) and out-of-plane (f) directions of perovskite, perovskite+BTTI-C6, perovskite+BTTI-C8 and perovskite+BTTI-C12, respectively.

Furthermore, we measured the 2D-GIWAXS of the perovskite/HTMs bilayer films, with pure perovskite film as the control. Figure 4.6 shows that the diffraction peak

intensity weakens apparently from perovskite/BTTI-C12 film to the perovskite/BTTI-C6 film, indicating the formation of a denser pinhole-free film of BTTI-C6.

4.3.5 Characterization of devices performance

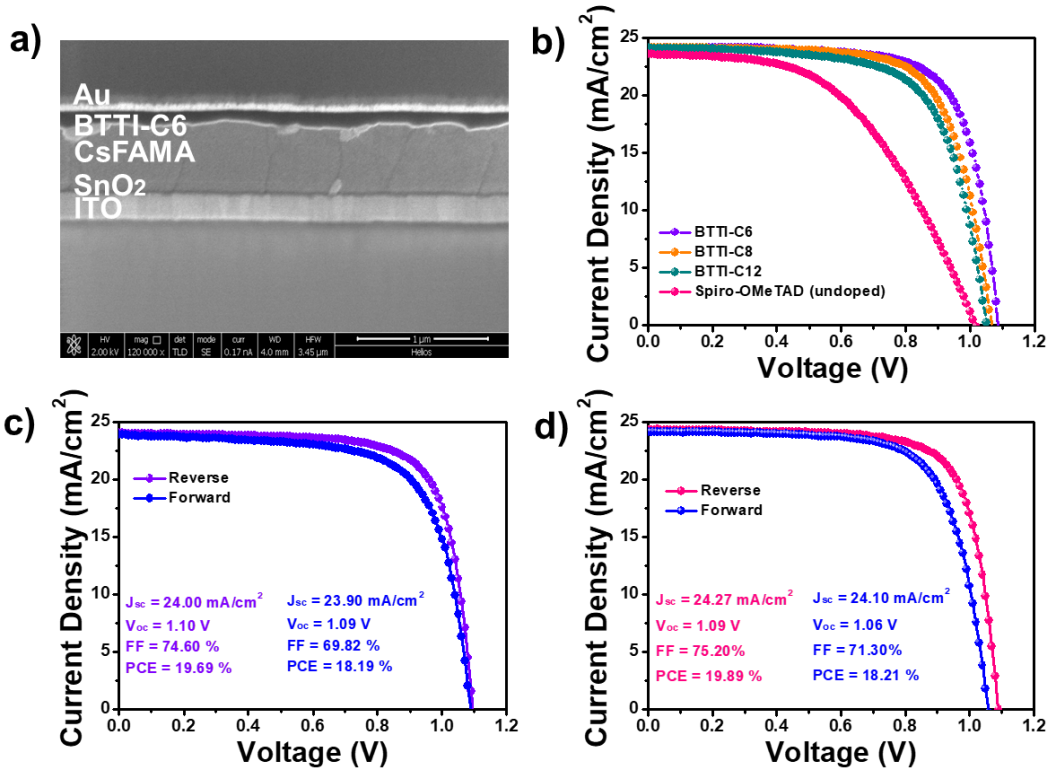

Figure 4.7 a) SEM image of devices with BTTI-C6. b) *J-V* curves of devices with the three dopant-free BTTI HTMs and Spiro-OMeTAD. c) Reverse and forward *J-V* curves of devices with BTTI-C6. d) *J-V* curves of PSCs with doped Spiro-OMeTAD.

We measured the device performance of the BTTI HTMs with a normal planar configuration of ITO/SnO_2/perovskite/HTMs/Au. Figure 4.7a shows a typical cross-section SEM image for BTTI-C6-based PSCs. BTTI-C6 HTM here is ~ 100 nm thickness and that of the underlying CsFAMA perovskite film is ~ 600 nm, with compact and large crystalline grains. The *J-V* curves of device with un-doped HTMs and Spiro-OMeTAD were shown in Figure 4.7b. Obviously, PSCs based on those BTTI HTMs have significantly improved conversion efficiencies compared to that of un-doped Spiro-OMeTAD. Clearly, highest PCE (19.69%) is achieved by BTTI-C6-based (with the

shortest side chain length) champion device, along with V_{oc} ~ 1.10 V, J_{sc} ~ 24.00 mA cm^{-2} and FF ~ 74.6% in the reverse mode (Figure 4.7c). And this best performance is comparable to doped Spiro-OMeTAD (19.90%) (Figure 4.7d).

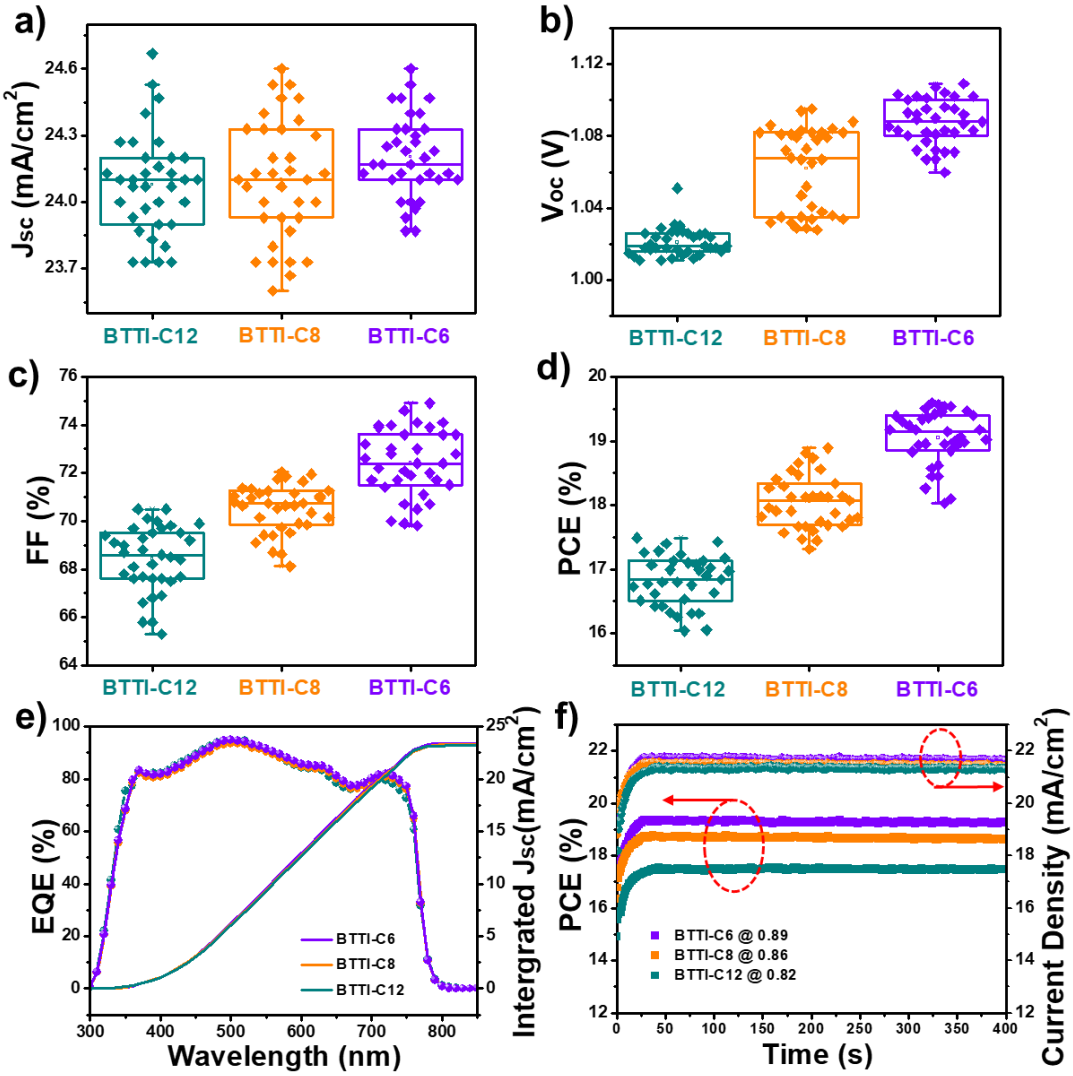

Figure 4.8 Statistics of J_{sc} (a), V_{oc} (b) and *FF* (c) based on the different BTTI HTMs. d) Histograms of the PCE devices based on the three BTTI HTMs. e) EQE spectrum of devices with the three BTTI HTMs. f) Stable output efficiency and current of the PSCs based on the three BTTI HTMs.

Figure 4.8a-d show the statistical data. The averages PCE are 16.83% (BTTI-C12), 18.04% (BTTI-C8) and 19.05% (BTTI-C6), respectively. The PCE improvement results from the augmentation of the V_{oc}, with values of 1.02 V (BTTI-C12), 1.06 V (BTTI-C8)

and 1.09 V (BTTI-C6). Simultaneously, the FF increases, 68.39% (BTTI-C12), 70.52% (BTTI-C8) and 72.43% (BTTI-C6), respectively (Table 4.2). The increases in V_{oc} and *FF* may be ascribed to the denser pinhole-free film, which enhanced the hole extraction, hole transport and interfacial contact between perovskite/HTM and/or HTM/anode electrode (Bin et al., 2018).

Figure 4.8e shows the EQE spectra, representing the photon responsibility of the three BTTI-HTM-based devices in the entire visible region. The extracted J_{sc} values within the present experimental accuracy are 23.41 (BTTI-C6), 23.27 (BTTI-C8) and 23.26 mA/cm^2 (BTTI-C12), in agreement with our *J-V* curve measurement. Meanwhile, we monitored the MPPT to evaluate the stabilized power output. Figure 4.8f shows the photocurrent densities and the power output of these devices are nearly constant over time, clearly demonstrating the stability of the devices.

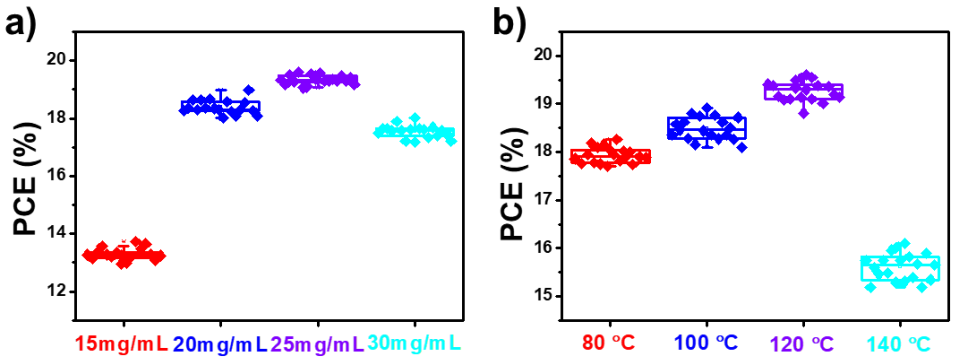

Figure 4.9 Optimization of BTTI-C6 based solar cells. a) PCE dependence of the solution concentration, b) PCE dependence of the annealing temperature.

Meantime, the optimization results of BTTI-C6 based solar cells on the solution concentration and annealing temperature are shown in Figure 4.9. These results indicated that the best concentration and annealing temperature are 25 mg/mL and 120˚C, respectively.

Table 4.2 Photovoltaic parameters of devices based on different HTLs.

HTL	J_{sc} [mA/cm^2]	Integrated J_{sc} [mA/cm^2]	V_{oc} [V]	*FF* [%]	PCE [%]
BTTI-C6	24.00[a] (24.20±0.40)[b]	23.41	1.10[a] (1.09±0.02)[b]	74.60[a] (72.43±2.46)[b]	19.69[a] (19.05±0.55)[b]
BTTI-C8	24.10[a] (24.10±0.50)[b]	23.27	1.094[a] (1.06±0.03)[b]	71.36[a] (70.52±1.54)[b]	18.89[a] (18.04±0.85)[b]
BTTI-C12	24.26[a] (24.08±0.44)[b]	23.26	1.031[a] (1.02±0.01)[b]	69.91[a] (68.39±2.13)[b]	17.49[a] (16.83±0.66)[b]

[a] The values correspond to the champion devices. [b] Averaged values.

4.3.6 Characterization of side chain effect

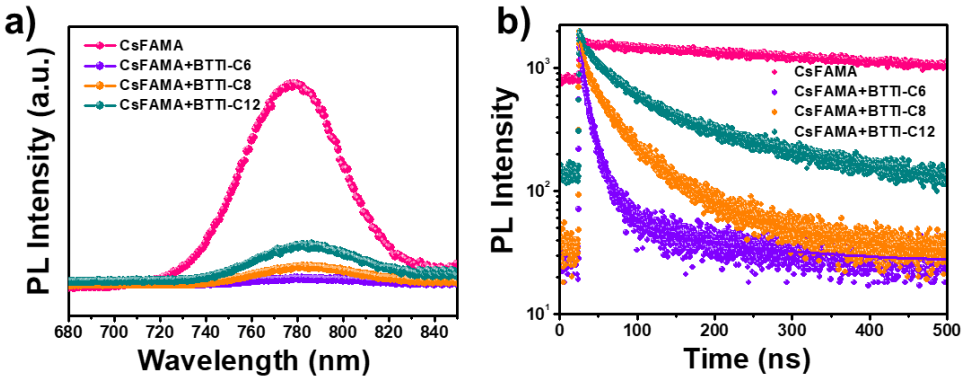

Figure 4.10 Steady PL spectrum (a) and TRPL spectrum (b) of perovskite capped with different BTTI HTMs.

To make clear the origin of the higher V_{oc} and FF by BTTI-C6, as foregoing remark, we characterized the charge extraction rate of the HTMs by steady-state PL measurements. The quench effect of those dopant-free HTMs on the perovskite was observed clearly. The largest quenching effect made by the BTTI-C6 HTM implies the highest charge extraction rate from perovskite to HTM (Figure 4.10a) (Aranda, Guerrero, & Bisquert, 2019). This was further confirmed by our time-resolved PL measurements (Figure 4.10b).

Table 4.3 Carrier lifetime based on the TRPL results.

Samples	τ_1 [ns]	A_1[%]	τ_2 [ns]	A_2[%]	Average τ [ns]
Glass/PVK	-	-	869.92	100	869.92
Glass/PVK/BTTI-C6	12.94	89.62	143.72	10.38	86.52
Glass/PVK/BTTI-C8	28.27	60.07	237.70	39.93	205.92
Glass/PVK/BTTI-C12	47.22	32.12	298.84	67.88	281.34

When fitted the PL decaying results by a bi-exponential equation (González-Pedro et al., 2018;Wu, Liao, Chan, Lu, & Su, 2018; Zhang et al., 2016), we extracted the decay time τ_1 that reflects the monomolecular recombination, and the fastest hole extraction ability is from the BTTI-C6 at τ_1 ~ 12.94 ns (BTTI-C6), followed by 28.27 ns (BTTI-C8) and 47.22 ns (BTTI-C12) (Table 4.3). The accelerated hole extraction may be attributed to the improved molecular packing, which leads to a denser pinhole-free film on the perovskite, resulting from an improved interfacial contact and an enhanced hole-transporting ability (Chen et al., 2017; Lee et al., 2019).

Meanwhile, we also study the relationship between *J-V* characteristics and illumination intensity to elaborate the recombination mechanism in PSCs based on those BTTI series HTMs. J_{sc} is dependent to light intensity (as Figure 4.11a shown), where the slope (α) follows a trend of BTTI-C6 (0.923) > BTTI-C8 (0.913) > BTTI-C12 (0.898), suggesting suppressed bimolecular recombination at the interface by shortening the side chain length of the HTMs (Cai et al., 2018). In addition, the V_{oc} dependence on the illumination intensity is probably related to a trap-assisted recombination behavior. As shown in Figure 4.11b, the diode ideality factor decreases from 1.38 *KT/q* (BTTI-C12) to 1.22 K*T/q* (BTTI-C6), indicating a lower trap-assisted SRH monomolecular recombination. This finding is consistent with the increased V_{oc} and *FF* values in the PSCs (Azmi et al., 2018; Choi et al., 2018). To confirm the changed trap densities in the BTTI HTMs-based PSCs, hole-only PSCs with ITO/NiO_X/perovskite/BTTI HTMs/Au structure was prepared to reveal

the trap state density of perovskite under dark conditions (Figure 4.11c). All curves show a nearly linear response at a low applied bias and kink points indicative of an ohmic response of the devices. The sharp increases in current density, when the applied bias is higher than the kink point, the trap states will be filled, as marked on each curve (Chen et al., 2017). The kink point, therefore, represents the V_{TFL}, which is believed to correlate with the trap state density (Chen et al., 2019). The V_{TFL} values for the hole-only devices are 0.071 V for BTTI-C6, 0.083 V for BTTI-C8 and 0.099 V for BTTI-C12, indicating that the BTTI-C6-based device holds the lowest trap state density. We thus suggest that the decreased trap state density could be an intrinsic factor that leads to the improvement in the device performance.

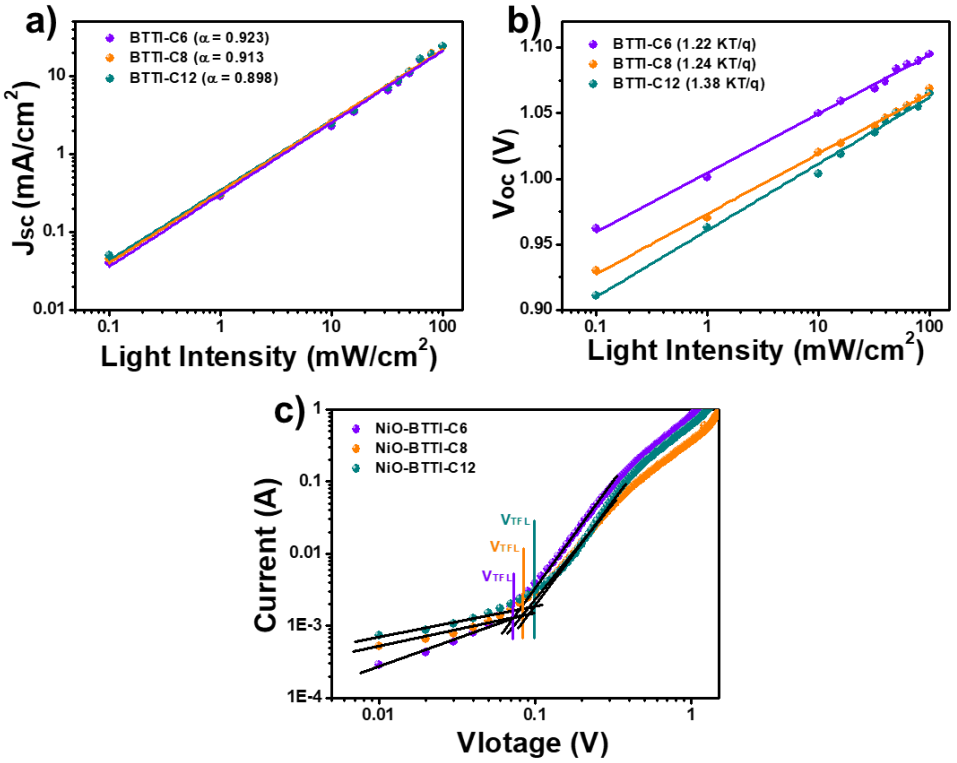

Figure 4.11 J_{sc} (a) and V_{oc} (b) as a function of the light intensity of PSCs based on the BTTI HTMs. c) *J-V* measurement for hole-only PSCs with ITO/NiOx/perovskite/BTTI HTMs/Au structure.

4.3.7 Characterization of stability

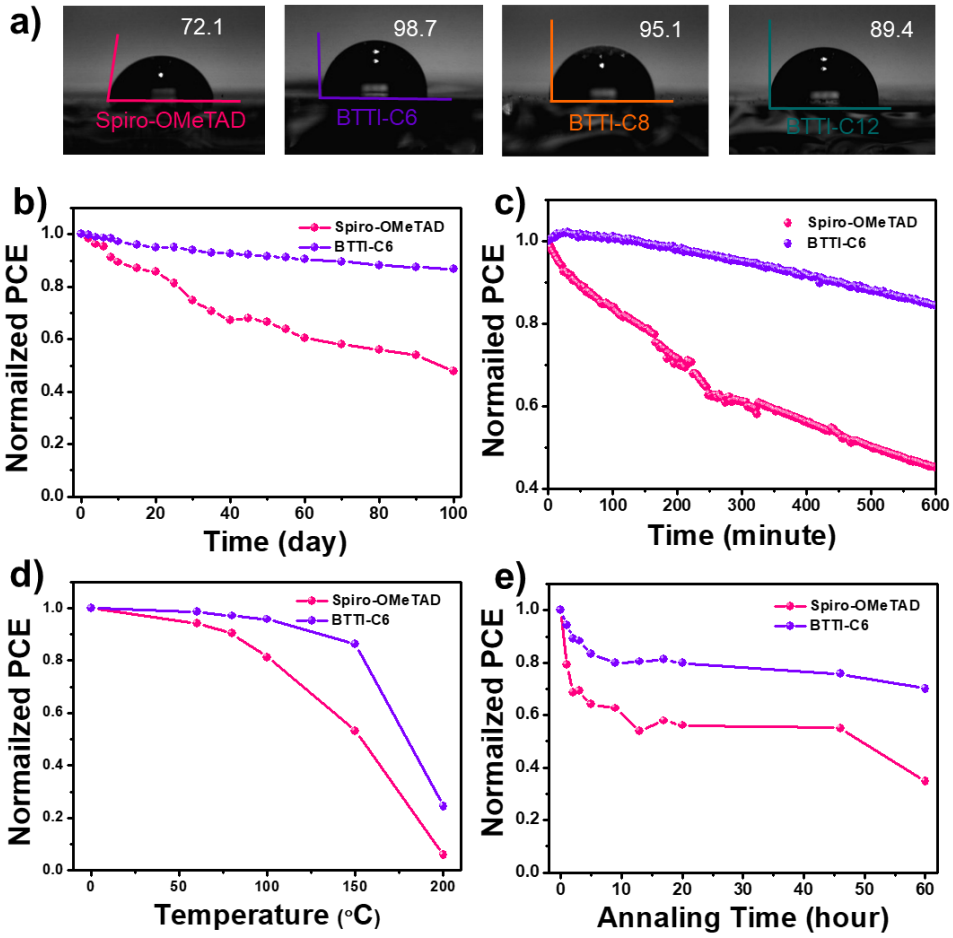

Figure 4.12 a) Contact angle of different HTLs. b) Long-term stability test of un-encapsulated devices with undoped BTTI-C6 and doped Spiro-OMeTADas HTLs at ambient conditions (28 ˚C, 24% RH), with the contact angle as marked. c) Accelerated aging test of the un-encapsulated devices based on the BTTI-C6 and the Spiro-OMeTAD under light soaking in an ambient environment (30 ˚C, 67% RH). d) Temperature-dependent thermal stability of the BTTI-C6- and the Spiro-OMeTAD-based devices in an ambient environment (67 % RH). e) Time-dependent thermal stability of the devices with BTTI-C6 and Spiro-OMeTAD under a constant 100 ˚C in N_2 atmosphere.

We monitored the stability of the PSCs derived from dopant-free BTTI-C6 and doped Spiro-OMeTAD HTMs under the same aging conditions. Firstly, we compared the long-term stability when the devices are stored atmospheric atmosphere with relative humidity ~ 24%. Figure 4.12b shows that the device employing the BTTI-C6 as the HTM maintained more than 85% of the initial efficiency even after 100 days, while that of doped

Spiro-OMeTAD-based PSCs has degraded to 45%. The enhanced long-term stability may be ascribed to the improved hydrophobic property of the BTTI-C6 film, as the static contact angle (α) of the deionized water droplet increases from 72.1° (Spiro-OMeTAD) to 98.7° (BTTI-C6). The static contact angle is dependent on alkyl chain length (Figure 4.12a). The enhancement verifies again that the BTTI-C6 has the most compact stacking in the solid state, which inhibits the water penetration to the largest extent.

Additionally, we also monitor the stability of the un-encapsulated dopant-free BTTI-C6-based and doped Spiro-OMeTAD-based PSCs under light soaking in an ambient environment (~ 30 ˚C, 67% humidity). Figure 4.12c shows that approximately 85% of the initial PCE remains for the dopant-free BTTI-C6 device after 10 h, however that of doped Spiro-OMeTAD based PSCs drops to 40%. Moreover, we evaluated the thermal stability of both devices at different temperatures (60-300 ˚C) for 10 mins. Our results show that even after heating at 100 ˚C for 10 mins, the PCE of BTTI-C6-based device remained nearly 95% and after another heating at 150 ˚C for an additional 10 minutes, only degraded by 15%. By comparison, the PCE of the Spiro-OMeTAD-based device decreased to 50% (Figure 4.12d). Furthermore, we tested the time-dependent thermal stability of the un-encapsulated devices in an N_2 atmosphere at 100 ˚C. Figure 4.12e shows that both devices degraded rapidly in the first 5 h and then smoothly became stable. The retained PCE of 70% for BTTI-C6-based PSCs was much higher than that (30%) of the Spiro-OMeTAD-based PSCs. The improved thermal stability of the BTTI-C6-based device may be ascribed to the removal of ionic dopants in the HTMs (Sun, Wu, Zhong, Zhu, & Li, 2019).

4.4 Conclusions

In summary, dopants free HTMs have been introduced for the optimization of HTL in n-i-p planar PSCs. The side chain length of hole-transport small molecules was revealed

to be important for photovoltaic performance. Molecules with different side chain lengths show comparable photophysical and electrochemical properties but are remarkably distinct in their film-forming capability, which influences the processes of charge extraction, transport and recombination and thus has a large impact on PCE. Our results suggested that BTTI-C6 with the shortest side chain exhibits the most excellent film morphology, and when it was utilized as a dopant-free HTM in a planar n-i-p PSCs, an encouraging PCE ~ 19.69% was achieved, much higher than the 18.89% for BTTI-C8 and the 17.49% for BTTI-C12. Moreover, the BTTI-HTM-based devices exhibit largely improved long-term illumination and thermal stability compared to the Spiro-OMeTAD-based devices. Our study may pave a promising way for dopant-free HTMs development in planar n-i-p PSCs.

5. Summary and future plans

5.1 Summary

PSCs has attracted extensive interest because of their fascinating photovoltaic properties, with certified PCE as high as 25.2% just in a very short time. However, improving the efficiency and stability of PSCs is still a problem that needs to be solved urgently. The history of PCE enhancement has confirmed the importance of perovskite fabrication, transport layer optimization and the interfacial passivation. Among them, the optimization of transport layers both ETL and HTL is an effective way to facilitating charge extraction, reducing charge recombination, controlling the perovskite crystals growth, increasing device stability, and so on. Based on our used architecture, optimization of SnO_2 transport layer and replacing Spiro-MeOTAD with dopant free HTMs are necessary ways to improve PCE and stability.

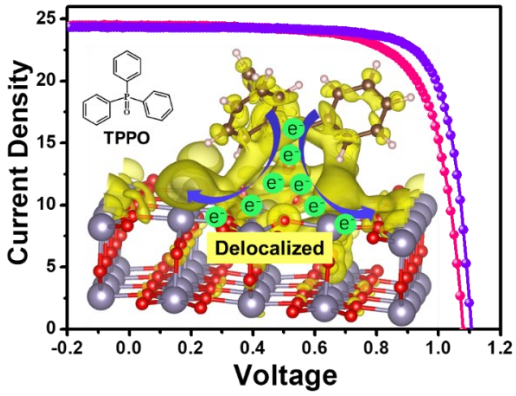

Figure 5.1 Summary of the molecular doping of SnO_2 on the PSCs.

The optimization of SnO_2 transport layer was realized by the molecular doping and defect passivation of SnO_2, respectively. For molecular doping work, a simple, air-robust and cheap electron donor, TPPO, was successfully adopted to realize n-type doping of SnO_2, which was confirmed directly by EFM and the blue shift of Sn 3d core level in XPS results. DFT calculations were employed to discover the details of charge transfer between

TPPO and SnO_2, which reveals that the interaction between TPPO and SnO_2 surface is very strong and transferred electrons are delocalized at the surface. Owing to the enhanced conductivity and decreased work function after optimization, the built-in field enlarged (from 0.01 eV to 0.07 eV) and the energy barrier decreased (from 0.55 eV to 0.39 eV), enabling an increasement in PCE from 19.01% to 20.69% (As summarized in Figure 5.1). For defect passivation work, a novel strategy was proposed to passivate SnO_2 nanocrystal ETL and SnO_2/perovskite interface synchronously. The confirmed H_2N-SiO_X@SnO_2 accounts for the suppressed defects and alleviated charge accumulation, enabled significant improvement of photovoltage from 1.09 to 1.15 V, and PCE from 20.24 to 21.76%, with a significant suppression of current hysteresis and enhanced device stability (As summarized in Figure 5.2).

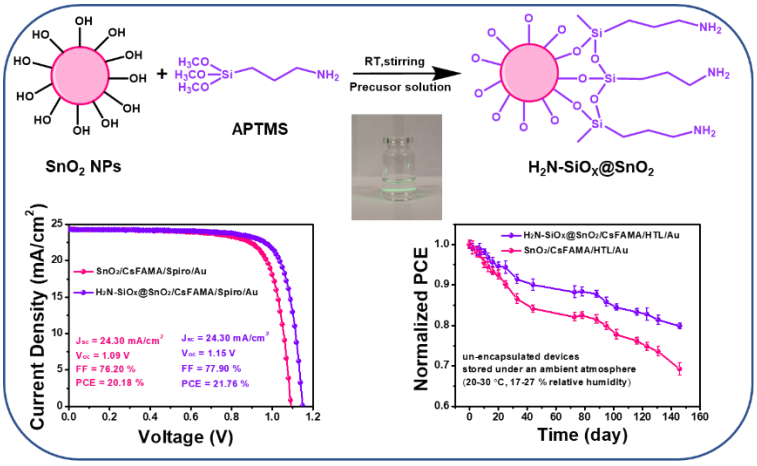

Figure 5.2 Summary of the defect passivation of SnO_2 on the PSCs.

The optimization of HTL was realized by introducing dopant free HTMs. Through tailoring its alkyl side chain length as BTTI-C6, BTTI-C8 and BTTI-C12, our study shows that the film quality was remarkably improved with a decrease in the side-chain length without losing the native photophysical and electrochemical properties. BTTI-C6 (the shortest side chain) based device shows an optimal PCE of 19.69%, which is comparable

to the routine-doped Spiro-OMeTAD-based device (19.90%), and bvious advantages of long-term storage, light soaking and thermal stability (As summarized in Figure 5.3).

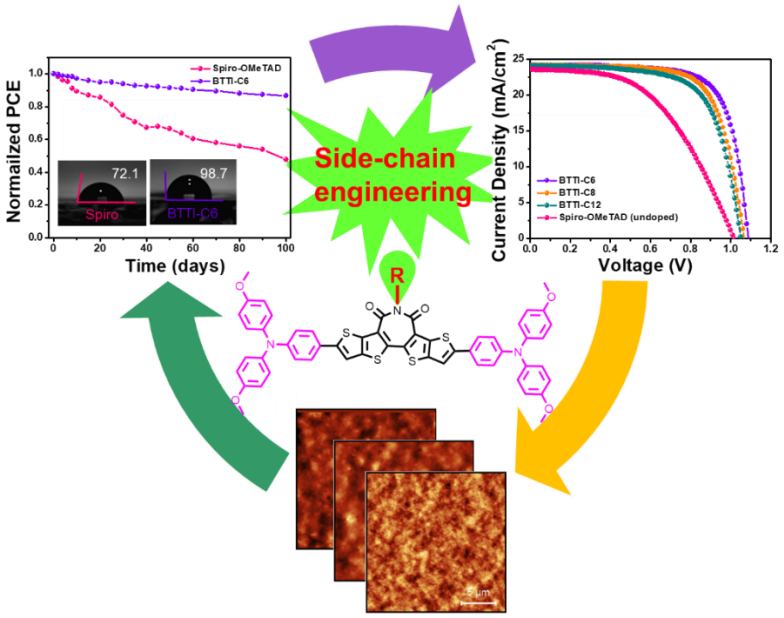

Figure 5.3 Summary of dopant-free HTMs on the PSCs.

For summary, molecular doping of SnO_2, defect passivation of SnO_2 and introduction of new dopants free HTMs have been successfully realized in our work for transport layer optimization and results in improved efficiency and stability. All these works suggested the importance of transport layer and the interface formed by transport layer and perovskite layer, demonstrated the distinct advantages of transport layer optimization. Accompany with the proposed novel ideas during the optimizations, my thesis could provide some new options to improve efficiency and stability, promote people's understanding of mechanism behind increased performance.

5.2 Simplify molecular design of new dopants free BTTI based HTMs

The exploration of efficient dopant-free HTMs with low-cost synthesis, good repeatability and high stability is urgently needed for the development of the planar n-i-p PSCs. In this event, small molecular HTMs are envisioned as excellent candidates

compared to polymer counterparts due to their well-defined structures, good reproducibility and fine-tuned optoelectronic properties (Im et al., 2011). Bearing in mind general principles for designing dopant-free small molecular HTMs (*e.g.* high chemical stability, suitable energy level, good film morphology and high hole mobility at neat film), many efficient molecules with various structures have been developed, while the PCE of nip PSCs with new designed HTM still lag far behind the doped Spiro-OMeTAD (Cai et al., 2019; Shen et al., 2019; Sun et al., 2019). Since different groups may have their own special material systems, enhancing the performance by structural optimization on specific molecular backbone seems to be more important (Cho et al., 2017; Sun et al., 2018). Despite of this, remarkable alternation of molecular backbone is usually required for searching an optimized structure and maximizing device performance in dopant-free PSCs, which seems to be a capricious and time-consuming process. As a result, alternative strategy is needed to simplify molecular design of highly efficient HTMs. Therefore, different BTTI based dopant free HTMs are expected to be synthesized to achieve the structure-activity relationship between their structure and the efficiency of the based PSCs.

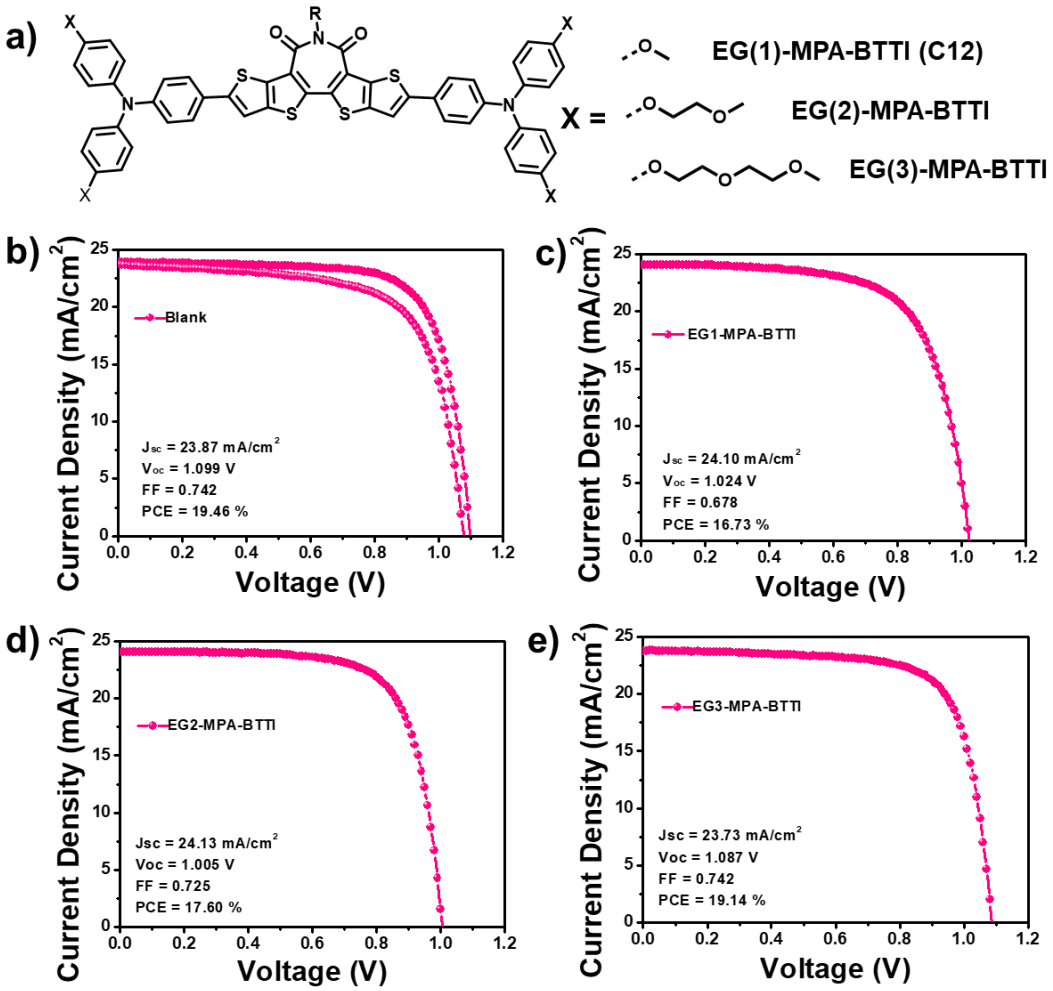

Figure 5.4 The effects of the X lengths on the PSCs.

Here, partly experiments have been accomplished. Figure 5.4 shows us that the increase in the X lengths is benefit to the improvement of the PCE. Figure 5.5 indicated that the existed of branched chain is obstruct to the increased efficiency.

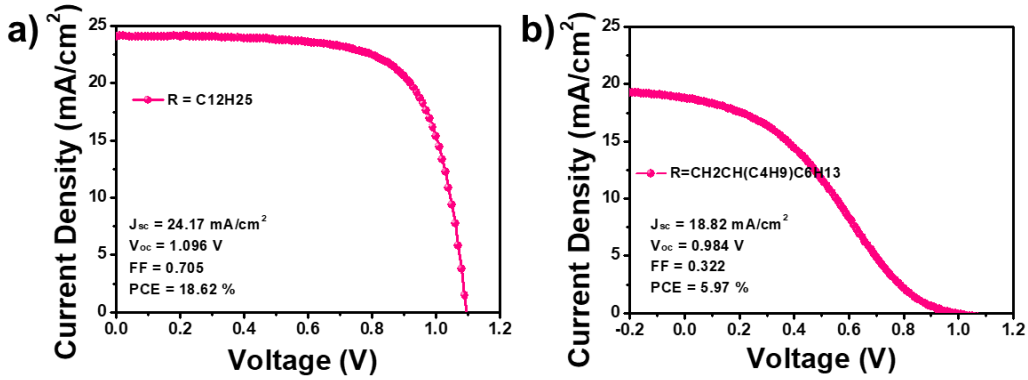

Figure 5.5 The effect of branched chain on the PSCs.

5.3 Optimization of perovskite layer

Superior quality of photoactive perovskite film is important to further increasing the photovoltaic performance of PSCs (Yang et al., 2019). However, high-quality perovskite fabrication is still a challenge due to the formation of point defects during annealing process, which make a large loss in V_{oc} (Fu et al., 2018). The emerging of the binary ligand strategy is a potential way to ameliorate morphology (Zhang et al., 2019). For example, the synergistic effect of thiourea and DMSO has been investigated to modulating the crystallization of perovskite (Lee, Kim, & Park, 2016). Another binary ligand additives such as thio-semicarbazide and methylammonium acetate have also reported to enlarge the crystal size and form uniform perovskite film with full coverage morphology, respectively (Wu et al., 2017). Other small organic molecules (e.g., 4-tert-butylpyridine,(Shi et al., 2015) benzoquinone (Qin, Matsushima, Fujihara, & Adachi, 2017), N-cyclohexyl-2-pyrrolidone (Jeon et al., 2014), and organic acids (e.g., 5-ammoniumvaleric acid (Mei et al., 2014), sulfamic acid (Guo, Sato, Shoyama, & Nakamura, 2016), and citric acid (Guo et al., 2017) have also been proposed for the improvement in film morphology and crystalline quality of perovskite film.

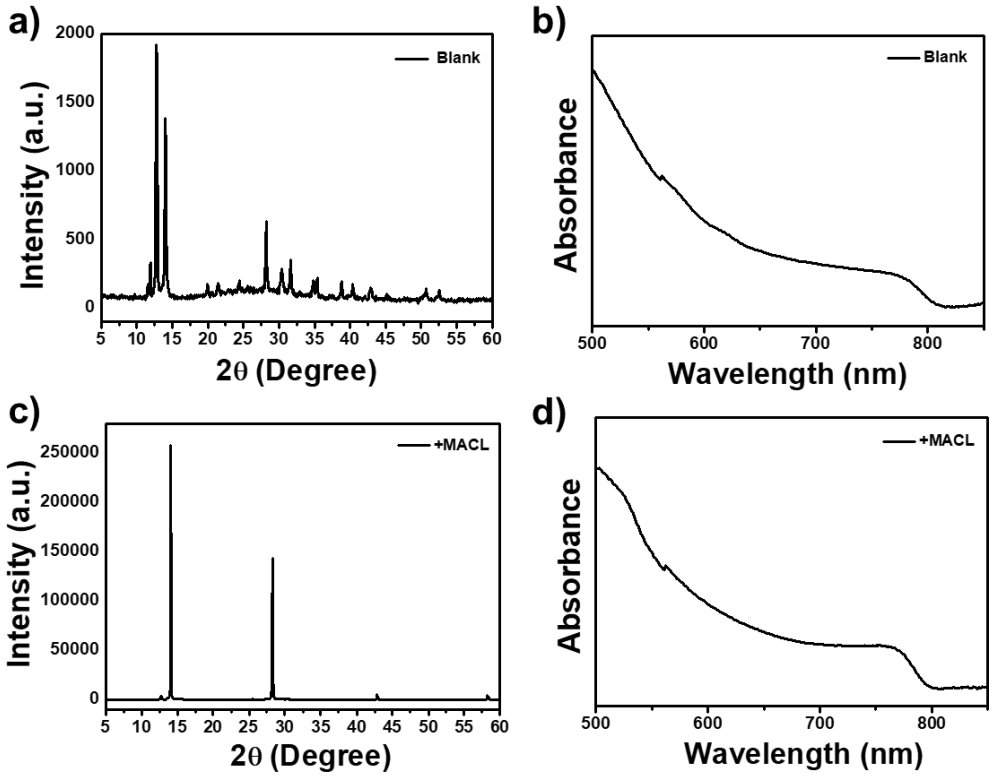

Figure 5.6 XRD (a) and UV-vis spectrums (b) with addition of MACl. XRD (c) and UV-vis (d) spectrums without addition of MACl.

Based on these, we also try to improve the perovskite (based on $Cs_{0.05}(FA_{0.99}MA_{0.01})_{0.95}Pb(I_{0.99}Br_{0.01})_3$) crystalline and morphology by the addition of additives. Our results indicated add MACl into precursor solution is benefit to the perovskite crystalline (Figure 5.6). And the following work on the photovoltaic performance will be investigated.

6. References

Abate, A., Correa-Baena, J. P., Saliba, M., Suait, M. S., & Bella, F. (2018). Perovskite solar cells: from the laboratory to the assembly line. *Chemistry, 24*(13), 3083-3100.

Abuhelaiqa, M., Paek, S., Lee, Y., Cho, K. T., Heo, S., Oveisi, E., . . . Nazeeruddin, M. K. (2019). Stable perovskite solar cells using tin acetylacetonate based electron transporting layers. *Energy & Environmental Science, 12*(6), 1910-1917.

Adams, W. G., & Day, R. E. (1876). The action of light on selenium. *Nature, 13*, 407-408.

Amat, A., Mosconi, E., Ronca, E., Quarti, C., Umari, P., Nazeeruddin, M. K., . . . De Angelis, F. (2014). Cation-induced band-gap tuning in organohalide perovskites: interplay of spin-orbit coupling and octahedra tilting. *Nano Letters, 14*(6), 3608-3616.

Ansari, M. I. H., Qurashi, A., & Nazeeruddin, M. K. (2018). Frontiers, opportunities, and challenges in perovskite solar cells: A critical review. *Journal of Photochemistry and Photobiology C: Photochemistry Reviews, 35*, 1-24.

Aranda, C., Guerrero, A., & Bisquert, J. (2019). Ionic effect enhances light emission and the photovoltage of methylammonium lead bromide perovskite solar cells by reduced surface recombination. *ACS Energy Letters, 4*(3), 741-746.

Arora, N., Dar, M. I., Hinderhofer, A., Pellet, N., Schreiber, F., Zakeeruddin, S. M., & Grätzel, M. (2017). Perovskite solar cells with CuSCN hole extraction layers yield stabilized efficiencies greater than 20%. *Science, 358*, 768-771.

Ayguler, M. F., Hufnagel, A. G., Rieder, P., Wussler, M., Jaegermann, W., Bein, T., . . . Docampo, P. (2018). Influence of fermi level alignment with tin oxide on the hysteresis of perovskite solar cells. *ACS Applied Materials & Interfaces, 10*(14), 11414-11419.

Azmi, R., Hadmojo, W. T., Sinaga, S., Lee, C.-L., Yoon, S. C., Jung, I. H., & Jang, S.-Y.

(2018). High-efficiency low-temperature ZnO based perovskite solar cells based on highly polar, nonwetting self-assembled molecular layers. *Advanced Energy Materials, 8*(5), 1701683.

Azmi, R., Nam, S. Y., Sinaga, S., Akbar, Z. A., Lee, C.-L., Yoon, S. C., . . . Jang, S.-Y. (2018). High-performance dopant-free conjugated small molecule-based hole-transport materials for perovskite solar cells. *Nano Energy, 44*, 191-198.

Babayigit, A., Ethirajan, A., Muller, M., & Conings, B. (2016). Toxicity of organometal halide perovskite solar cells. *Nature Materials, 15*(3), 247-251. doi:10.1038/nmat4572

Batzill, M., & Diebold, U. (2005). The surface and materials science of tin oxide. *Progress in Surface Science, 79*(2-4), 47-154.

Becquerel, A. E. (1839). The photovoltaic effect. *Comptes Rendus, 9* 145.

Bera, A., Sheikh, A. D., Haque, M. A., Riya Bose, R., Erkki Alarousu, E., Omar F. Mohammed, O. F., & Wu, T. (2015). Fast crystallization and improved stability of perovskite solar cells with Zn2SnO4 electron transporting layer:interface matters. *ACS Applied Materials & Interfaces, 7*, 28404-28411.

Bera, A., Wu, K., Sheikh, A., Alarousu, E., Mohammed, O. F., & Wu, T. (2014). Perovskite oxide SrTiO3 as an efficient electron transporter for hybrid perovskite solar cells. *The Journal of Physical Chemistry C, 118*(49), 28494-28501.

Bin, H., Yang, Y., Peng, Z., Ye, L., Yao, J., Zhong, L., . . . Li, Y. (2018). Effect of alkylsilyl side-chain structure on photovoltaic properties of conjugated polymer donors. *Advanced Energy Materials, 8*(8), 1702324.

Boehme, S. C., Azpiroz, J. M., Aulin, Y. V., Grozema, F. C., Vanmaekelbergh, D., Siebbeles, L. D., . . . Houtepen, A. J. (2015). Density of trap states and auger-mediated electron trapping in CdTe quantum-dot solids. *Nano Letters, 15*(5), 3056-3066.

Bozyigit, D., Lin, W. M., Yazdani, N., Yarema, O., & Wood, V. (2015). A quantitative model for charge carrier transport, trapping and recombination in nanocrystal-based solar cells. *Nature Communications, 6*, 6180.

Bozyigit, D., Volk, S., Yarema, O., & Wood, V. (2013). Quantification of deep traps in nanocrystal solids, their electronic properties, and their influence on device behavior. *Nano Letters, 13*(11), 5284-5288.

Bryce, D. L., Eichele, K., & Wasylishen, R. E. (2003). An ^{17}O NMR and quantum chemical study of monoclinic and orthorhombic polymorphs of triphenylphosphine oxide. *Inorganic Chemistry, 42*, 5085-5096.

Burschka, J., Pellet, N., Moon, S. J., Humphry-Baker, R., Gao, P., Nazeeruddin, M. K., & Gratzel, M. (2013). Sequential deposition as a route to high-performance perovskite-sensitized solar cells. *Nature, 499*(7458), 316-319.

Cai, B., Yang, X., Jiang, X., Yu, Z., Hagfeldt, A., & Sun, L. (2019). Boosting the power conversion efficiency of perovskite solar cells to 17.7% with an indolo[3,2-b]carbazole dopant-free hole transporting material by improving its spatial configuration. *Journal of Materials Chemistry A, 7*(24), 14835-14841.

Cai, F., Cai, J., Yang, L., Li, W., Gurney, R. S., Yi, H., . . . Wang, T. (2018). Molecular engineering of conjugated polymers for efficient hole transport and defect passivation in perovskite solar cells. *Nano Energy, 45*, 28-36.

Calió, L., Kazim, S., Grätzel, M., & Ahmad, S. (2016). Hole-transport materials for perovskite solar cells. *Angewandte Chemie International Edition, 55*, 14522-14545.

Chapin, D. M., Fuller, C. S., & Pearson, G. L. (1954). A new silicon p-n junction photocell for converting solar radiation into electrical power. *Journal of Applied Physics, 25*(5), 676-677.

Chen, H., Ye, F., Tang, W., He, J., Yin, M., Wang, Y., . . . Han, L. (2017). A solvent- and vacuum-free route to large-area perovskite films for efficient solar modules. *Nature, 550*(7674), 92-95.

Chen, R., Cao, J., Duan, Y., Hui, Y., Chuong, T. T., Ou, D., . . . Zheng, N. (2019). High-efficiency, hysteresis-less, uv-stable perovskite solar cells with cascade ZnO-ZnS electron transport layer. *Journal of the American Chemical Society, 141*(1), 541-547.

Chen, W., Li, K., Wang, Y., Feng, X., Liao, Z., Su, Q., . . . He, Z. (2017). Black phosphorus quantum dots for hole extraction of typical planar hybrid perovskite solar cells. *The Journal of Physical Chemistry Letters, 8*(3), 591-598.

Chen, W., Luo, S., Wan, Z., Feng, X., Liu, X., & He, Z. (2017). Ruthenium acetylacetonate in interface engineering for high performance planar hybrid perovskite solar cells. *OPTICS EXPRESS, 25*(8), A253-A263.

Chen, W., Wu, Y., Fan, J., Djurišić, A. B., Liu, F., Tam, H. W., . . . He, Z.-B. (2018). Understanding the doping effect on NiO: Toward high-performanceinverted perovskite solar cells. *Advanced Energy Materials, 8*(19), 1703519.

Chen, W., Wu, Y., Tu, B., Liu, F., Djurišić, A. B., & He, Z. (2018). Inverted planar organic-inorganic hybrid perovskite solar cells with NiOx hole-transport layers as light-in window. *Applied Surface Science, 451*, 325-332.

Chen, W., Xu, L., Feng, X., Jie, J., & He, Z. (2017). Metal acetylacetonate series in interface engineering for full low-temperature-processed, high-performance, and stable planar perovskite solar cells with conversion efficiency over 16% on 1 $cm(^2)$ scale. *Advanced Materials, 29*(16), 1603923.

Chen, W., Zhang, G., Xu, L., Gu, R., Xu, Z., Wang, H., & He, Z. (2016). Low temperature processed, high-performance and stable NiOx based inverted planar perovskite solar

cells via a poly(2-ethyl-2-oxazoline) nanodots cathode electron-extraction layer. *Materials Today Energy, 1-2*, 1-10.

Chen, W., Zhou, Y., Chen, G., Wu, Y., Tu, B., Liu, F. Z., . . . He, Z. (2019). Alkali chlorides for the suppression of the interfacial recombination in inverted planar perovskite solar cells. *Advanced Energy Materials, 9*(19), 1803872.

Chen, Z., Wang, J. J., Ren, Y., Yu, C., & Shum, K. (2012). Schottky solar cells based on CsSnI3 thin-films. *Applied Physics Letters, 101*(9), 093901.

Chesnut, D. B. (1998). An Ab initio nuclear magnetic resonance and atoms-in-molecules study of the PO bond in phosphine oxides. *Journal of the American Chemical Society, 120*, 10504-10510.

Cho, I., Jeon, N. J., Kwon, O. K., Kim, D. W., Jung, E. H., Noh, J. H., . . . Park, S. Y. (2017). Indolo[3,2-b]indole-based crystalline hole-transporting material for highly efficient perovskite solar cells. *Chemical Science, 8*(1), 734-741.

Choi, K., Lee, J., Kim, H. I., Park, C. W., Kim, G.-W., Choi, H., . . . Park, T. (2018). Thermally stable, planar hybrid perovskite solar cells with high efficiency. *Energy & Environmental Science, 11*(11), 3238-3247.

Christians, J. A., Fung, R. C., & Kamat, P. V. (2014). An inorganic hole conductor for organo-lead halide perovskite solar cells. Improved hole conductivity with copper iodide. *Journal of the American Chemical Society, 136*(2), 758-764.

Chueh, C.-C., Li, C.-Z., & Jen, A. K. Y. (2015). Recent progress and perspective in solution-processed Interfacial materials for efficient and stable polymer and organometal perovskite solar cells. *Energy & Environmental Science, 8*(4), 1160-1189.

Conings, B., Drijkoningen, J., Gauquelin, N., Babayigit, A., D'Haen, J., D'Olieslaeger, L., . . . Boyen, H.-G. (2015). Intrinsic thermal instability of methylammonium lead

trihalide perovskite. *Advanced Energy Materials, 5*(15), 1500477.

Correa Baena, J. P., Steier, L., Tress, W., Saliba, M., Neutzner, S., Matsui, T., . . . Hagfeldt, A. (2015). Highly efficient planar perovskite solar cells through band alignment engineering. *Energy & Environmental Science, 8*(10), 2928-2934.

Cortecchia, D., Dewi, H. A., Yin, J., Bruno, A., Chen, S., Baikie, T., . . . Mathews, N. (2016). Lead-Free $MA_2CuCl_{(x)}Br_{(4-x)}$ Hybrid Perovskites. *Inorganic Chemistry, 55*(3), 1044-1052.

Deng, W., Liang, X., Kubiak, P. S., & Cameron, P. J. (2018). Molecular interlayers in hybrid perovskite solar cells. *Advanced Energy Materials, 8*(1).

Djurišić, A. B., Liu, F. Z., Tam, H. W., Wong, M. K., Ng, A., Surya, C., . . . He, Z. B. (2017). Perovskite solar cells - an overview of critical issues. *Progress in Quantum Electronics, 53*, 1-37.

Dobado, J. A., Martínez-García, H., Molina, H. M.-G., & Sundberg, M. R. (1998). Chemical bonding in hypervalent molecules revised. Application of the atoms in molecules theory to Y_3X and Y_3XZ (Y = H or CH_3; X = N, P or As; Z = O or S) compounds. *Journal of the American Chemical Society, 120*(33), 8461-8471.

Duan, J., Xiong, Q., Feng, B., Xu, Y., Zhang, J., & Wang, H. (2017). Low-temperature processed SnO_2 compact layer for efficient mesostructure perovskite solar cells. *Applied Surface Science, 391*, 677-683.

Dubey, A., Adhikari, N., Mabrouk, S., Wu, F., Chen, K., Yang, S., & Qiao, Q. (2018). A strategic review on processing routes towards highly efficient perovskite solar cells. *Journal of Materials Chemistry A, 6*(6), 2406-2431.

Dunlap-Shohl, W. A., Zhou, Y., Padture, N. P., & Mitzi, D. B. (2019). Synthetic approaches for halide perovskite thin films. *Chemical Reviews, 119*(5), 3193-3295.

Fu, P., Guo, X., Wang, S., Ye, Y., & Li, C. (2017). Aminosilane as a molecular linker between the electron-transport layer and active layer for efficient inverted polymer solar cells. *ACS Applied Materials & Interfaces, 9*(15), 13390-13395.

Fu, Q., Tang, X., Huang, B., Hu, T., Tan, L., Chen, L., & Chen, Y. (2018). Recent progress on the long-term stability of perovskite solar cells. *Advanced Science, 5*(5), 1700387.

Fu, R., Zhao, Y., Zhou, W., Li, Q., Zhao, Y., & Zhao, Q. (2018). Ultrahigh open-circuit voltage for high performance mixed-cation perovskite solar cells using acetate anions. *Journal of Materials Chemistry A, 6*(29), 14387-14391.

Gangopadhyay, U., Jana, S., & Das, S. (2013). State of art of solar photovoltaic technology. *Conference Papers in Energy, 2013*, 1-9.

Gattu, K. P., Ghule, K., Kashale, A. A., Patil, V. B., Phase, D. M., Mane, R. S., . . . Ghule, A. V. (2015). Bio-green synthesis of Ni-doped tin oxide nanoparticles and its influence on gas sensing properties. *RSC Advances, 5*(89), 72849-72856.

Gharibzadeh, S., Abdollahi Nejand, B., Jakoby, M., Abzieher, T., Hauschild, D., Moghadamzadeh, S., . . . Paetzold, U. W. (2019). Record open-circuit voltage wide-bandgap perovskite solar cells utilizing 2D/3D perovskite heterostructure. *Advanced Energy Materials, 9*(21), 1803699.

González-Pedro, V., Veldhuis, S. A., Begum, R., Bañuls, M. J., Bruno, A., Mathews, N., . . . Maquieira, A. (2018). Recovery of shallow charge-trapping ddefects in $CsPbX_3$ nanocrystals through specific binding and encapsulation with amino-functionalized silanes. *ACS Energy Letters, 3*(6), 1409-1414.

Green, M. A., Ho-Baillie, A., & Snaith, H. J. (2014). The emergence of perovskite solar cells. *Nature Photonics, 8*(7), 506-514.

Grimme, S., Antony, J., Ehrlich, S., & Krieg, H. (2010). A consistent and accurate ab initio

parametrization of density functional dispersion correction (DFT-D) for the 94 elements H-Pu. *The Journal of Chemical Physics, 132*(15), 154104.

Guo, Y., Sato, W., Shoyama, K., Halim, H., Itabashi, Y., Shang, R., & Nakamura, E. (2017). Citric acid modulated growth of oriented lead perovskite crystals for efficient solar cells. *Journal of the American Chemical Society, 139*(28), 9598-9604.

Guo, Y., Sato, W., Shoyama, K., & Nakamura, E. (2016). Sulfamic acid-catalyzed lead perovskite formation for solar cell fabrication on glass or plastic substrates. *Journal of the American Chemical Society, 138*(16), 5410-5416.

Harikesh, P. C., Mulmudi, H. K., Ghosh, B., Goh, T. W., Teng, Y. T., Thirumal, K., . . . Mathews, N. (2016). Rb as an alternative cation for templating inorganic lead-free perovskites for solution processed photovoltaics. *Chemistry of Materials, 28*(20), 7496-7504.

Havelaar, A. H., Kirk, M. D., Torgerson, P. R., Gibb, H. J., Hald, T., Lake, R. J., . . . Devleesschauwer, B. (2015). World health organization global estimates and regional comparisons of the burden of foodborne disease in 2010. *PLoS Medicine, 12*(12), 1001923.

Hawash, Z., Ono, L. K., & Qi, Y. (2018). Recent advances in Spiro-MeOTAD hole transport material and its applications in organic-inorganic halide perovskite solar cells. *Advanced Materials Interfaces, 5*(1), 1700623.

Hieulle, J., Stecker, C., Ohmann, R., Ono, L. K., & Qi, Y. (2018). Scanning probe microscopy applied to organic-inorganic halide perovskite materials and solar cells. *Small Methods, 2*(1), 1700295.

Hou, M., Zhang, H., Wang, Z., Xia, Y., Chen, Y., & Huang, W. (2018). Enhancing efficiency and stability of perovskite solar cells via a self-assembled dopamine

interfacial layer. *ACS Applied Materials & Interfaces, 10*(36), 30607-30613.

Huang, C., Fu, W., Li, C. Z., Zhang, Z., Qiu, W., Shi, M., . . . Chen, H. (2016). Dopant-free hole-transporting material with a C3h symmetrical truxene core for highly efficient perovskite solar cells. *Journal of the American Chemical Society, 138*(8), 2528-2531.

Im, J. H., Jang, I. H., Pellet, N., Gratzel, M., & Park, N. G. (2014). Growth of $CH_3NH_3PbI_3$ cuboids with controlled size for high-efficiency perovskite solar cells. *Nature Nanotechnol, 9*(11), 927-932.

Im, J. H., Lee, C. R., Lee, J. W., Park, S. W., & Park, N. G. (2011). 6.5% efficient perovskite quantum-dot-sensitized solar cell. *Nanoscale, 3*(10), 4088-4093.

Ito, S., Tanaka, S., Vahlman, H., Nishino, H., Manabe, K., & Lund, P. (2014). Carbon-double-bond-free printed solar cells from TiO_2/$CH_3NH_3PbI_3$/CuSCN/Au: structural control and photoaging effects. *Chemphyschem, 15*(6), 1194-1200.

Jeon, N. J., Na, H., Jung, E. H., Yang, T.-Y., Lee, Y. G., Kim, G., . . . Seo, J. (2018). A fluorene-terminated hole-transporting material for highly efficient and stable perovskite solar cells. *Nature Energy, 3*(8), 682-689.

Jeon, N. J., Noh, J. H., Kim, Y. C., Yang, W. S., Ryu, S., & Seok, S. I. (2014). Solvent engineering for high-performance inorganic-organic hybrid perovskite solar cells. *Nature Materials, 13*(9), 897-903.

Jeon, Y. J., Lee, S., Kang, R., Kim, J. E., Yeo, J. S., Lee, S. H., . . . Kim, D. Y. (2014). Planar heterojunction perovskite solar cells with superior reproducibility. *Scientific Reports, 4*, 6953.

Jiang, Q., Chu, Z., Wang, P., Yang, X., Liu, H., Wang, Y., . . . You, J. (2017). Planar-structure perovskite solar cells with efficiency beyond 21%. *Advanced Materials, 29*(46), 1703852.

Jiang, Q., Zhang, L., Wang, H., Yang, X., Meng, J., Liu, H., . . . You, J. (2017). Enhanced electron extraction using SnO_2 for high-efficiency planar-structure $HC(NH_2)_2PbI_3$-based perovskite solar cells. *Nature Energy, 2*(1), 16177.

Jiang, Q., Zhang, X., & You, J. (2018). SnO_2 : a wonderful electron transport layer for perovskite solar cells. *Small, 14*(31), 1801154.

Jiang, Q., Zhao, Y., Zhang, X., Yang, X., Chen, Y., Chu, Z., . . . You, J. (2019). Surface passivation of perovskite film for efficient solar cells. *Nature Photonics, 13*(7), 460-466.

Jiang, X., Wang, D., Yu, Z., Ma, W., Li, H.-B., Yang, X., . . . Sun, L. (2019). Molecular engineering of copper phthalocyanines: A strategy in developing dopant-free hole-transporting materials for efficient and ambient-stable perovskite solar cells. *Advanced Energy Materials, 9*(4), 1803287.

Jung, E. H., Jeon, N. J., Park, E. Y., Moon, C. S., Shin, T. J., Yang, T. Y., . . . Seo, J. (2019). Efficient, stable and scalable perovskite solar cells using poly(3-hexylthiophene). *Nature, 567*(7749), 511-515.

Jung, J. S., Lee, J. W., Seo, M. R., Lee, H. S., Kim, J., Lee, S. W., & Joo, J. (2012). Luminescence variation of organic Alq3 nanoparticles on surface of Au nanoparticles and graphene. *Synthetic Metals, 162*(21-22), 1852-1857.

Kang, D. H., & Park, N. G. (2019). On the current-voltage hysteresis in perovskite solar cells: Dependence on perovskite composition and methods to remove hysteresis. *Advanced Materials, 31*(34), e1805214.

Kang, Y.-G., Park, H.-G., Kim, H.-J., Kim, Y.-H., Oh, B.-Y., Kim, B.-Y., . . . Seo, D.-S. (2010). Superior optical properties of homogeneous liquid crystal alignment on a tin (IV) oxide surface sequentially modulated via ion beam irradiation. *Optics Express, 18*,

21594-21602.

Kasparavicius, E., Magomedov, A., Malinauskas, T., & Getautis, V. (2018). Long-term stability of the oxidized hole-transporting materials used in perovskite solar cells. *Chemistry, 24*(39), 9910-9918.

Katsiev, K., Ip, A. H., Fischer, A., Tanabe, I., Zhang, X., Kirmani, A. R., . . . Bakr, O. M. (2014). The complete in-gap electronic structure of colloidal quantum dot solids and its correlation with electronic transport and photovoltaic performance. *Advanced Materials, 26*(6), 937-942.

Ke, W., Fang, G., Liu, Q., Xiong, L., Qin, P., Tao, H., . . . Yan, Y. (2015). Low-temperature solution-processed tin oxide as an alternative electron transporting layer for efficient perovskite solar cells. *Journal of the American Chemical Society, 137*(21), 6730-6733.

Ke, W., Zhao, D., Xiao, C., Wang, C., Cimaroli, A. J., Grice, C. R., . . . Yan, Y. (2016). Cooperative tin oxide fullerene electron selective layers for high-performance planar perovskite solar cells. *Journal of Materials Chemistry A, 4*(37), 14276-14283.

Kim, H.-S., Seo, J.-Y., & Park, N. G. (2016). Material and device stability in perovskite solar cells. *ChemSusChem, 9*, 2528-2540.

Kim, H. S., Lee, C. R., Im, J. H., Lee, K. B., Moehl, T., Marchioro, A., . . . Park, N. G. (2012). Lead iodide perovskite sensitized all-solid-state submicron thin film mesoscopic solar cell with efficiency exceeding 9%. *Scientific Reports, 2*, 591.

Kim, J. H., Williams, S. T., Cho, N., Chueh, C.-C., & Jen, A. K. Y. (2015). Enhanced environmental stability of planar heterojunction perovskite solar cells based on blade-coating. *Advanced Energy Materials, 5*(4).

Kim, Y. H., Kim, D. G., Maduwu, R. D., Jin, H. C., Moon, D. K., & Kim, J. H. (2018). Organic electrolytes doped ZnO layer as the electron transport layer for bulk

heterojunction polymer solar cells. *Solar RRL, 2*(8), 1800086.

Kirmani, A. R., Kiani, A., Said, M. M., Voznyy, O., Wehbe, N., Walters, G., . . . Amassian, A. (2016). Remote molecular doping of colloidal quantum dot photovoltaics. *ACS Energy Letters, 1*(5), 922-930.

Kittel, C., & Holcomb, D. F. (1967). Introduction to solid state pshysics. *American Journal of Physics, 35*(6), 547-548.

Kogo, A., Numata, Y., Ikegami, M., & Miyasaka, T. (2015). Nb_2O_5 blocking layer for high open-circuit voltage perovskite solar cells. *Chemistry Letters, 44*(6), 829-830.

Kojima, A., Teshima, K., Miyasaka, T., & Shirai, Y. (2006). *Meet Abstract, 02*, 397.

Kojima, A., Teshima, K., Shirai, Y., & Miyasaka, T. (2009). Organometal halide perovskites as visible-light sensitizers for photovoltaic cells. *Journal of the American Chemical Society, 131*, 6050-6051.

Krishnamoorthy, T., Ding, H., Yan, C., Leong, W. L., Baikie, T., Zhang, Z., . . . Mhaisalkar, S. G. (2015). Lead-free germanium iodide perovskite materials for photovoltaic applications. *Journal of Materials Chemistry A, 3*(47), 23829-23832.

Kumar, M. H., Yantara, N., Dharani, S., Graetzel, M., Mhaisalkar, S., Boix, P. P., & Mathews, N. (2013). Flexible, low-temperature, solution processed ZnO-based perovskite solid state solar cells. *Chemical Communications, 49*(94), 11089-11091.

Lee, J.-W., Kim, D.-H., Kim, H.-S., Seo, S.-W., Cho, S. M., & Park, N.-G. (2015). Formamidinium and cesium hybridization for photo- and moisture-stable perovskite solar cell. *Advanced Energy Materials, 5*(20), 1501310.

Lee, J. W., Kim, H. S., & Park, N. G. (2016). Lewis acid-base adduct approach for high efficiency perovskite solar cells. *Accounts of Chemical Research, 49*(2), 311-319.

Lee, M. M., Teuscher, J., Miyasaka, T., Murakami, T. N., & Snaith, H. J. (2012). Efficient

hybrid solar cells based on meso-superstructured organometal halide perovskites. *Science, 338* 643-647.

Lee, S., Park, K. H., Lee, J. H., Back, H., Sung, M. J., Lee, J., . . . Lee, K. (2019). Achieving thickness-insensitive morphology of the photoactive layer for printable organic photovoltaic cells via side chain engineering in nonfullerene acceptors. *Advanced Energy Materials, 9*(14), 1900044.

Lee, Y., Kwon, J., Hwang, E., Ra, C. H., Yoo, W. J., Ahn, J. H., . . . Cho, J. H. (2015). High-performance perovskite-graphene hybrid photodetector. *Advanced Materials, 27*(1), 41-46.

Li, C., Tscheuschner, S., Paulus, F., Hopkinson, P. E., Kiessling, J., Kohler, A., . . . Huettner, S. (2016). Iodine migration and its effect on hysteresis in perovskite solar cells. *Advanced Materials, 28*(12), 2446-2454.

Li, W., Fan, J., Li, J., Niu, G., Mai, Y., & Wang, L. (2016). High performance of perovskite solar cells via catalytic treatment in two-step process: the case of solvent engineering. *ACS Applied Materials & Interfaces, 8*(44), 30107-30115.

Li, X., Bi, D., Yi, C., Décoppet, J.-D., Luo, J., Zakeeruddin, S. M., . . . Grätzel, M. (2016). A vacuum flash-assisted solution process for high-efficiency large-area perovskite solar cells. *Science, 353*(6294), 58-62.

Li, X., Dar, M. I., Yi, C., Luo, J., Tschumi, M., Zakeeruddin, S. M., . . . Grätzel, M. (2015). Improved performance and stability of perovskite solar cells by crystal crosslinking with alkylphosphonic acid omega-ammonium chlorides. *Nature Chemistry, 7*(9), 703-711.

Li, Y., Zhu, J., Huang, Y. J., Liu, F., Lv, M., Chen, S., . . . Dai, S. (2015). Mesoporous SnO2 nanoparticle films as electron-transporting material in perovskite solar cells. *RSC*

Advances, 5(36), 28424-28429.

Li, Z., Meng, X., & Zhang, Z. (2018). Recent development on MoS2-based photocatalysis: A review. *Journal of Photochemistry and Photobiology C: Photochemistry Reviews, 35*, 39-55.

Li, Z., Zhu, Z., Chueh, C. C., Jo, S. B., Luo, J., Jang, S. H., & Jen, A. K. (2016). Rational design of dipolar chromophore as an efficient dopant-free hole-transporting material for perovskite solar cells. *Journal of the American Chemical Society, 138*(36), 11833-11839.

Lin, K., Xing, J., Quan, L. N., de Arquer, F. P. G., Gong, X., Lu, J., . . . Wei, Z. (2018). Perovskite light-emitting diodes with external quantum efficiency exceeding 20 percent. *Nature, 562*(7726), 245-248.

Liu, F., Wu, F., Tu, Z., Liao, Q., Gong, Y., Zhu, L., . . . Li, Z. (2019). Hole transport materials based on 6,12-dihydroindeno[1,2-b]fluorine with different periphery groups: a new strategy for dopant-free perovskite solar cells. *Advanced Functional Materials, 29*(24), 1901296.

Liu, K., Chen, S., Wu, J., Zhang, H., Qin, M., Lu, X., . . . Zhan, X. (2018). Fullerene derivative anchored SnO2 for high-performance perovskite solar cells. *Energy & Environmental Science, 11*(12), 3463-3471.

Liu, M., Johnston, M. B., & Snaith, H. J. (2013). Efficient planar heterojunction perovskite solar cells by vapour deposition. *Nature, 501*(7467), 395-398.

Liu, X., Tsai, K.-W., Zhu, Z., Sun, Y., Chueh, C.-C., & Jen, A. K. Y. (2016). A low-temperature, solution processable tin oxide electron-transporting layer prepared by the dual-fuel combustion method for efficient perovskite solar cells. *Advanced Materials Interfaces, 3*(13), 1600122.

Liu, Z., Zhang, G., & Zhang, D. (2018). Modification of side chains of conjugated

molecules and polymers for charge mobility enhancement and sensing functionality. *Accounts of Chemical Research, 51*(6), 1422-1432.

Lu, K., Lei, Y., Qi, R., Liu, J., Yang, X., Jia, Z., . . . Zheng, Z. (2017). Fermi level alignment by copper doping for efficient ITO/perovskite junction solar cells. *Journal of Materials Chemistry A, 5*(48), 25211-25219.

Luo, W., Wu, C., Wang, D., Zhang, Y., Zhang, Z., Qi, X., . . . Chen, Z. (2019). Efficient and stable perovskite solar cell with high open-circuit voltage by dimensional interface modification. *ACS Applied Materials & Interfaces, 11*(9), 9149-9155.

Lussem, B., Keum, C. M., Kasemann, D., Naab, B., Bao, Z., & Leo, K. (2016). Doped organic transistors. *Chemical Reviews, 116*(22), 13714-13751.

Ma, B. B., Gao, R., Wang, L. D., Zhu, Y. F., Shi, Y. T., Geng, Y., . . . Qiu, Y. (2010). Recent progress in interface modification for dye-sensitized solar cells. *Science China Chemistry, 53*(8), 1669-1678.

Magomedov, A., Kasparavičius, E., Rakstys, K., Paek, S., Gasilova, N., Genevičius, K., . . . Getautis, V. (2018). Pyridination of hole transporting material in perovskite solar cells questions the long-term stability. *Journal of Materials Chemistry C, 6*(33), 8874-8878.

Maji, P., Choudhary, R. B., & Majhi, M. (2017). Structural, electrical and optical properties of silane-modified ZnO reinforced PMMA matrix and its catalytic activities. *Journal of Non-Crystalline Solids, 456*, 40-48.

Marchioro, A., Teuscher, J., Friedrich, D., Kunst, M., van de Krol, R., Moehl, T., . . . Moser, J.-E. (2014). Unravelling the mechanism of photoinduced charge transfer processes in lead iodide perovskite solar cells. *Nature Photonics, 8*(3), 250-255.

Martinez, J. I., Flores, F., Ortega, J., Rangan, S., Ruggieri, C., & Bartynski, R. (2015). Chemical interaction, space-charge layer and molecule charging energy for a

TiO_2/TCNQ interface. *Journal of Physical Chemistry C, 119*(38), 22086-22091.

MedveĎ, M., Fowler, P. W., & Hutson, J. M. (2000). Anisotropie dipole polarizabilities and quadrupole moments of open-shell atoms and ions: O, F, S, Cl, Se, Br and isoelectronic systems. *Molecular Physics, 98*(7), 453-463.

Mei, A., Li, X., Liu, L., Ku, Z., Liu, T., Rong, Y., . . . Han, H. (2014). A hole-conductor-free, fully printable mesoscopic perovskite solar cell with high stability. *Science, 345*(6194), 295-298.

Mendez, H., Heimel, G., Winkler, S., Frisch, J., Opitz, A., Sauer, K., . . . Salzmann, I. (2015). Charge-transfer crystallites as molecular electrical dopants. *Nature Communications, 6*, 8560.

Mitzi, D. B. (2001). Thin-film deposition of organic-inorganic hybrid materials. *Chemistry Materials, 13*, 3283-3298.

Moussodia, R.-O., Balan, L., Merlin, C., Mustin, C., & Schneider, R. (2010). Biocompatible and stable ZnO quantum dots generated by functionalization with siloxane-core PAMAM dendrons. *Journal of Materials Chemistry, 20*(6), 1147-1155.

Nasti, G., & Abate, A. (2019). Tin halide perovskite (ASnX3) solar cells: a comprehensive guide toward the highest power conversion efficiency. *Advanced Energy Materials*, 1902467.

Niemann, R. G., Gouda, L., Hu, J., Tirosh, S., Gottesman, R., Cameron, P. J., & Zaban, A. (2016). Cs^+ incorporation into $CH_3NH_3PbI_3$ perovskite: substitution limit and stability enhancement. *Journal of Materials Chemistry A, 4*(45), 17819-17827.

Noel, N. K., Stranks, S. D., Abate, A., Wehrenfennig, C., Guarnera, S., Haghighirad, A.-A., . . . Snaith, H. J. (2014). Lead-free organic–inorganic tin halide perovskites for photovoltaic applications. *Energy & Environmental Science, 7*(9), 3061-3068.

Noh, J. H., Im, S. H., Heo, J. H., Mandal, T. N., & Seok, S. I. (2013). Chemical management for colorful, efficient, and stable inorganic-organic hybrid nanostructured solar cells. *Nano Letters, 13*(4), 1764-1769.

NREL. (2020). *https://www.nrel.gov/pv/assets/pdfs/best-research-cell-efficiencies.20200218.pdf*.

Ok, S. A., Jo, B., Somasundaram, S., Woo, H. J., Lee, D. W., Li, Z., . . . Park, H. J. (2018). Management of transition dipoles in organic hole-transporting materials under solar irradiation for perovskite solar cells. *Nature Communications, 9*(1), 4537.

ORegan, B., & Gratzel, M. (1991). A low cost, high efficiency solar cell based on dye-sesitized colloidal TiO_2 films. *Nature, 353*, 737-740.

Paek, S., Qin, P., Lee, Y., Cho, K. T., Gao, P., Grancini, G., . . . Nazeeruddin, M. K. (2017). Dopant-free hole-transporting materials for stable and efficient perovskite solar cells. *Advanced Materials, 29*(35), 1606555.

Palanivel, V., Zhu, D., & van Ooij, W. J. (2003). Nanoparticle-filled silane films as chromate replacements for aluminum alloys. *Progress in Organic Coatings, 47*(3-4), 384-392.

Park, B. W., Philippe, B., Zhang, X., Rensmo, H., Boschloo, G., & Johansson, E. M. (2015). Bismuth based hybrid perovskites $A_3Bi_2I_9$ (A: Methylammonium or Cesium) for solar cell application. *Advanced Materials, 27*(43), 6806-6813.

Pasquarelli, R. M., Ginley, D. S., & O'Hayre, R. (2011). Solution processing of transparent conductors: from flask to film. *Chemical Society Reviews, 40*(11), 5406-5441.

Pathak, S. K., Abate, A., Ruckdeschel, P., Roose, B., Gödel, K. C., Vaynzof, Y., . . . Steiner, U. (2014). Performance and stability enhancement of dye-sensitized and perovskite solar cells by Al doping of TiO_2. *Advanced Functional Materials, 24*(38), 6046-6055.

Pham, H. D., Do, T. T., Kim, J., Charbonneau, C., Manzhos, S., Feron, K., . . . Sonar, P. (2018). Molecular engineering using an anthanthrone dye for low-cost hole transport materials: a strategy for dopant-free, high-efficiency, and stable perovskite solar cells. *Advanced Energy Materials, 8*(16), 1703007.

Pham, H. D., Gil-Escrig, L., Feron, K., Manzhos, S., Albrecht, S., Bolink, H. J., & Sonar, P. (2019). Boosting inverted perovskite solar cell performance by using 9,9-bis(4-diphenylaminophenyl)fluorene functionalized with triphenylamine as a dopant-free hole transporting material. *Journal of Materials Chemistry A, 7*(20), 12507-12517.

Pham, H. D., Hu, H., Feron, K., Manzhos, S., Wang, H., Lam, Y. M., & Sonar, P. (2017). Thienylvinylenethienyl and naphthalene core substituted with triphenylamines-highly efficient hole transporting materials and their comparative study for inverted perovskite solar cells. *Solar RRL, 1*(8), 1700105.

Pham, H. D., Hu, H., Wong, F.-L., Lee, C.-S., Chen, W.-C., Feron, K., . . . Sonar, P. (2018). Acene-based organic semiconductors for organic light-emitting diodes and perovskite solar cells. *Journal of Materials Chemistry C, 6*(33), 9017-9029.

Pham, H. D., Jain, S. M., Li, M., Manzhos, S., Feron, K., Pitchaimuthu, S., . . . Sonar, P. (2019). Dopant-free novel hole-transporting materials based on quinacridone dye for high-performance and humidity-stable mesoporous perovskite solar cells. *Journal of Materials Chemistry A, 7*(10), 5315-5323.

Pham, H. D., Li, X., Li, W., Manzhos, S., Kyaw, A. K. K., & Sonar, P. (2019). Organic interfacial materials for perovskite-based optoelectronic devices. *Energy & Environmental Science, 12*(4), 1177-1209.

Prochowicz, D., Tavakoli, M. M., Kalam, A., Chavan, R. D., Trivedi, S., Kumar, M., & Yadav, P. (2019). Influence of A-site cations on the open-circuit voltage of efficient

perovskite solar cells: a case of rubidium and guanidinium additives. *Journal of Materials Chemistry A, 7*(14), 8218-8225.

Qiao, H. W., Yang, S., Wang, Y., Chen, X., Wen, T. Y., Tang, L. J., . . . Yang, H. G. (2019). A gradient heterostructure based on tolerance factor in high-performance perovskite solar cells with 0.84 fill factor. *Advanced Materials, 31*(5), 1804217.

Qin, C., Matsushima, T., Fujihara, T., & Adachi, C. (2017). Multifunctional benzoquinone additive for efficient and stable planar perovskite solar cells. *Advanced Materials, 29*(4), 1603808.

Qin, M., Ma, J., Ke, W., Qin, P., Lei, H., Tao, H., . . . Fang, G. (2016). Perovskite solar cells based on low-temperature processed indium oxide electron selective layers. *ACS Applied Materials & Interfaces, 8*(13), 8460-8466.

Rakstys, K., Paek, S., Gao, P., Gratia, P., Marszalek, T., Grancini, G., . . . Nazeeruddin, M. K. (2017). Molecular engineering of face-on oriented dopant-free hole transporting material for perovskite solar cells with 19% PCE. *Journal of Materials Chemistry A, 5*(17), 7811-7815.

Rao, H.-S., Chen, B.-X., Li, W.-G., Xu, Y.-F., Chen, H.-Y., Kuang, D.-B., & Su, C.-Y. (2015). Improving the extraction of photogenerated electrons with SnO2 nanocolloids for efficient planar perovskite solar cells. *Advanced Functional Materials, 25*(46), 7200-7207.

Razza, S., Di Giacomo, F., Matteocci, F., Cinà, L., Palma, A. L., Casaluci, S., . . . Di Carlo, A. (2015). Perovskite solar cells and large area modules (100 cm2) based on an air flow-assisted PbI 2 blade coating deposition process. *Journal of Power Sources, 277*, 286-291.

Rhodes, A., Adibi, A., Asakura, S., Hänsch, G., Kamiya, T., Krausz, G., . . . Weinfurter,

M. (2009). High-efficient low-cost photovoltaics. *springer*, 1-223.

Rietwyk, K. J., Smets, Y., Bashouti, M., Christiansen, S. H., Schenk, A., Tadich, A., . . . Pakes, C. I. (2014). Charge transfer doping of silicon. *PHYSICAL REVIEW LETTERS, 112*(15), 155502.

Rong, Y., Hu, Y., Mei, A., Tan, H., Saidaminov, M. I., Seok, S. I., . . . Han, H. (2018). Challenges for commercializing perovskite solar cells. *Science, 361*(6408), eaat8235

Saliba, M., Matsui, T., Domanski, K., Seo, J.-Y., Ummadisingu, A., Zakeeruddin, S. M., . . . Grätzel, M. (2016a). Incorporation of rubidium cations into perovskite solar cells improves photovoltaic performance. *Science, 354*, 206-209.

Saliba, M., Matsui, T., Domanski, K., Seo, J. Y., Ummadisingu, A., Zakeeruddin, S. M., . . . Grätzel, M. (2016b). Incorporation ofrubidium cations into perovskite solar cells improves photovoltaic performance. *Science, 354* 206-209.

Saliba, M., Matsui, T., Seo, J. Y., Domanski, K., Correa-Baena, J. P., Nazeeruddin, M. K., . . . Grätzel, M. (2016). Cesium-containing triple cation perovskite solar cells: improved stability, reproducibility and high efficiency. *Energy & Environmental Science, 9*(6), 1989-1997.

Saliba, M., Wood, S. M., Patel, J. B., Nayak, P. K., Huang, J., Alexander-Webber, J. A., . . . Riede, M. K. (2016). Structured organic-inorganic perovskite toward a distributed feedback laser. *Advanced Materials, 28*(5), 923-929.

Salzmann, I., Heimel, G., Oehzelt, M., Winkler, S., & Koch, N. (2016). Molecular electrical doping of organic semiconductors: fundamental mechanisms and emerging dopant design rules. *Accounts of Chemical Reasearch, 49*(3), 370-378.

Schiessl, S. P., Faber, H., Lin, Y. H., Rossbauer, S., Wang, Q., Zhao, K., . . . Anthopoulos, T. D. (2016). Hybrid modulation-doping of solution-processed ultrathin layers of ZnO

using molecular dopants. *Advanced Materials, 28*(20), 3952-3959.

Schlesinger, R., Bianchi, F., Blumstengel, S., Christodoulou, C., Ovsyannikov, R., Kobin, B., . . . Koch, N. (2015). Efficient light emission from inorganic and organic semiconductor hybrid structures by energy-level tuning. *Nature Communications, 6*, 6754.

Schultz, T., Niederhausen, J., Schlesinger, R., Sadofev, S., & Koch, N. (2018). Impact of surface states and bulk doping level on hybrid inorganic/organic semiconductor interface energy levels. *Journal of Applied Physics, 123*(24), 245501.

Seok, S. I., Grätzel, M., & Park, N. G. (2018). Methodologies toward highly efficient perovskite solar cells. *Small, 14*(20), 1704177.

Shahiduzzaman, M., Ashikawa, H., Kuniyoshi, M., Visal, S., Sakakibara, S., Kaneko, T., . . . Tomita, K. (2018). Compact TiO_2/anatase TiO_2 single-crystalline nanoparticle electron-transport bilayer for efficient planar perovskite solar cells. *ACS Sustainable Chemistry & Engineering, 6*(9), 12070-12078.

Shen, C., Wu, Y., Zhang, H., Li, E., Zhang, W., Xu, X., . . . Zhu, W. H. (2019). Semi-locked tetrathienylethene as a building block for hole-transporting materials: Toward efficient and stable perovskite solar cells. *Angewandte Chemie International Edition, 58*(12), 3784-3789.

Shi, B., Duan, L., Zhao, Y., Luo, J., & Zhang, X. (2020). Semitransparent perovskite solar cells: From materials and devices to applications. *Advanced Materials, 32*(3), e1806474.

Shi, Y. T., Wang, X., Zhang, H., Li, B., Lu, H., Ma, T., & Hao, C. (2015). Effects of 4-tert-butylpyridine on perovskite formation and performance of solution-processed perovskite solar cells. *Journal of Materials Chemistry A, 3*(44), 22191-22198.

Singh, T., Kulkarni, A., Ikegami, M., & Miyasaka, T. (2016). Effect of electron

transporting layer on bismuth-based lead-free perovskite $(CH_3NH_3)_3Bi_2I_9$ for photovoltaic applications. *ACS Applied Materials & Interfaces, 8*(23), 14542-14547.

Smith, I. C., Hoke, E. T., Solis-Ibarra, D., McGehee, M. D., & Karunadasa, H. I. (2014). A layered hybrid perovskite solar-cell absorber with enhanced moisture stability. *Angewandte Chemie International Edition, 53*(42), 11232-11235.

Spek, A. L. (1987). Structure of a second monoelinie polymorph of triphenylphosphine oxide. *Acta Crystallographica Section E, C43*, 1233-1235.

Subbiah, A. S., Mathews, N., Mhaisalkar, S., & Sarkar, S. K. (2018). Novel plasma-assisted low-temperature-processed SnO2 thin films for efficient flexible perovskite photovoltaics. *ACS Energy Letters, 3*(7), 1482-1491.

Sun, H., Deng, J., Qiu, L., Fang, X., & Peng, H. (2015). Recent progress in solar cells based on one-dimensional nanomaterials. *Energy & Environmental Science, 8*(4), 1139-1159.

Sun, X., Wu, F., Zhong, C., Zhu, L., & Li, Z. (2019). A structure-property study of fluoranthene-cored hole-transporting materials enables 19.3% efficiency in dopant-free perovskite solar cells. *Chemical Science, 10*(28), 6899-6907.

Sun, X., Xue, Q., Zhu, Z., Xiao, Q., Jiang, K., Yip, H. L., . . . Li, Z. (2018). Fluoranthene-based dopant-free hole transporting materials for efficient perovskite solar cells. *Chemical Science, 9*(10), 2698-2704.

Sun, Y., Wu, Y., Fang, X., Xu, L., Ma, Z., Lu, Y., . . . Ding, J. (2017). Long-term stability of organic–inorganic hybrid perovskite solar cells with high efficiency under high humidity conditions. *Journal of Materials Chemistry A, 5*(4), 1374-1379.

Tan, H., Jain, A., Voznyy, O., Lan, X., Arquer, F. P. G. D., Fan, J. Z., . . . Sargent, E. H. (2017). Efficient and stable solution-processed planar perovskite solar cells via contact

passivation. *Science, 355*, 722-726.

Tarasov, A., Zhang, S., Tsai, M. Y., Campbell, P. M., Graham, S., Barlow, S., . . . Vogel, E. M. (2015). Controlled doping of large-area trilayer MoS2 with molecular reductants and oxidants. *Advanced Materials, 27*(7), 1175-1181.

Todinova, A., Idigoras, J., Salado, M., Kazim, S., & Anta, J. A. (2015). Universal features of electron dynamics in solar cells with TiO_2 contact: From dye solar cells to perovskite solar cells. *The Journal of Physical Chemistry Letters, 6*(19), 3923-3930.

Truong, M. A., Lee, J., Nakamura, T., Seo, J. Y., Jung, M., Ozaki, M., . . . Wakamiya, A. (2019). Influence of alkoxy chain length on the properties of two-dimensionally expanded azulene-core-based hole-transporting materials for efficient perovskite solar cells. *Chemistry, 25*(27), 6741-6752.

Tsai, H., Nie, W., Blancon, J. C., Stoumpos, C. C., Asadpour, R., Harutyunyan, B., . . . Kanatzidis, M. G. (2016). High-efficiency two-dimensional Ruddlesden-Popper perovskite solar cells. *Nature, 536*(7616), 312-316.

Tu, B., Shao, Y., Chen, W., Wu, Y., Li, X., He, Y., . . . He, Z. (2019). Novel molecular doping mechanism for n-doping of SnO2 via triphenylphosphine oxide and its effect on perovskite solar cells. *Advanced Materials, 31*(15), 1805944.

Urbani, M., de la Torre, G., Nazeeruddin, M. K., & Torres, T. (2019). Phthalocyanines and porphyrinoid analogues as hole- and electron-transporting materials for perovskite solar cells. *Chemical Society Reviews, 48*(10), 2738-2766.

Wadia, C., Alivisatos, A. P., & Kammen, D. M. (2009). Materials availability expands the opportunity for large-scale photovoltaics deployment. *Environmental Science & Technology, 43*, 2072-2077.

Wang, C., Nakano, K., Lee, H. F., Chen, Y., Hong, Y. L., Nishiyama, Y., & Tajima, K.

(2018). Intermolecular arrangement of fullerene acceptors proximal to semiconducting polymers in mixed bulk heterojunctions. *Angewandte Chemie International Edition, 57*(24), 7034-7039.

Wang, C., Zhao, D., Grice, C. R., Liao, W., Yu, Y., Cimaroli, A., . . . Yan, Y. (2016). Low-temperature plasma-enhanced atomic layer deposition of tin oxide electron selective layers for highly efficient planar perovskite solar cells. *Journal of Materials Chemistry A, 4*(31), 12080-12087.

Wang, F., Jiang, X., Chen, H., Shang, Y., Liu, H., Wei, J., . . . Ning, Z. (2018). 2D-Quasi-2D-3D hierarchy structure for tin perovskite solar cells with enhanced efficiency and stability. *Joule, 2*(12), 2732-2743.

Wang, K., Zheng, L., Zhu, T., Yao, X., Yi, C., Zhang, X., . . . Gong, X. (2019). Efficient perovskite solar cells by hybrid perovskites incorporated with heterovalent neodymium cations. *Nano Energy, 61*, 352-360.

Wang, X., Deng, L.-L., Wang, L.-Y., Dai, S.-M., Xing, Z., Zhan, X.-X., . . . Zheng, L.-S. (2017). Cerium oxide standing out as an electron transport layer for efficient and stable perovskite solar cells processed at low temperature. *Journal of Materials Chemistry A, 5*(4), 1706-1712.

Wang, Y., Chen, W., Wang, L., Tu, B., Chen, T., Liu, B., . . . Guo, X. (2019). Dopant-free small-molecule hole-transporting material for inverted perovskite solar cells with efficiency exceeding 21%. *Advanced Materials, 31*(35), 1902781.

Weber, D. (1978). CH3NH3PbX3, a Pb(II)-system with cubic perovskite structure. *Zeitschrift Fur Naturforschung Section, 33 b*, 1443-1445.

Wu, D. Y., Liu, X. M., Duan, S., Xu, X., Ren, B., Lin, S. H., & Tian, Z. Q. (2008). Chemical enhancement effects in SERS spectra: A quantum chemical study of pyridine

interacting with copper, silver, gold and platinum metals. *Journal of Physical Chemistry C, 112*, 4195-4204.

Wu, M.-C., Liao, Y.-H., Chan, S.-H., Lu, C.-F., & Su, W.-F. (2018). Enhancing organolead halide perovskite solar cells performance through interfacial engineering using Ag-doped TiO_2 hole blocking layer. *Solar RRL, 2*(8), 1800072.

Wu, W.-Q., Chen, D., Cheng, Y.-B., & Caruso, R. A. (2017). Thin films of tin oxide nanosheets used as the electron transporting layer for improved performance and ambient stability of perovskite photovoltaics. *Solar RRL, 1*(11), 1700117.

Wu, Y., Xie, F., Chen, H., Yang, X., Su, H., Cai, M., . . . Han, L. (2017). Thermally stable MAPbI3 perovskite solar cells with efficiency of 19.19% and area over 1 cm^2 achieved by additive engineering. *Advanced Materials, 29*(28), 1701073.

Wu, Y., Yang, X., Chen, W., Yue, Y., Cai, M., Xie, F., . . . Han, L. (2016). Perovskite solar cells with 18.21% efficiency and area over 1 cm^2 fabricated by heterojunction engineering. *Nature Energy, 1*(11), 16148.

Xiao, M., Huang, F., Huang, W., Dkhissi, Y., Zhu, Y., Etheridge, J., . . . Spiccia, L. (2014). A fast deposition-crystallization procedure for highly efficient lead iodide perovskite thin-film solar cells. *Angewandte Chemie International Edition, 53*(37), 9898-9903.

Xie, J., Huang, K., Yu, X., Yang, Z., Xiao, K., Qiang, Y., . . . Yang, D. (2017). Enhanced electronic properties of SnO_2 via electron transfer from graphene quantum dots for efficient perovskite solar cells. *ACS Nano, 11*(9), 9176-9182.

Xiong, L., Guo, Y., Wen, J., Liu, H., Yang, G., Qin, P., & Fang, G. (2018). Review on the application of SnO_2 in perovskite solar cells. *Advanced Functional Materials, 28*(35), 1802757.

Xiong, L., Qin, M., Chen, C., Wen, J., Yang, G., Guo, Y., . . . Fang, G. (2018). Fully high-

temperature-processed SnO_2 as blocking layer and scaffold for efficient, stable, and hysteresis-free mesoporous perovskite solar cells. *Advanced Functional Materials, 28*(10), 1706276.

Xu, F., Zhang, T., Li, G., & Zhao, Y. (2017). Synergetic effect of chloride doping and $CH_3NH_3PbCl_3$ on $CH3NH_3PbI_{3-x}Cl_x$ perovskite-based solar cells. *ChemSusChem, 10*(11), 2365-2369.

Yalcin, S. E., Labastide, J. A., Sowle, D. L., & Barnes, M. D. (2011). Spectral properties of multiply charged semiconductor quantum dots. *Nano Letters, 11*(10), 4425-4430.

Yang, D., Yang, R., Wang, K., Wu, C., Zhu, X., Feng, J., . . . Liu, S. F. (2018). High efficiency planar-type perovskite solar cells with negligible hysteresis using EDTA-complexed SnO_2. *Nature Communications, 9*(1), 3239.

Yang, D., Yang, R., Zhang, J., Yang, Z., Liu, S., & Li, C. (2015). High efficiency flexible perovskite solar cells using superior low temperature TiO_2. *Energy & Environmental Science, 8*(11), 3208-3214.

Yang, D., Zhou, X., Yang, R., Yang, Z., Yu, W., Wang, X., . . . Chang, R. P. H. (2016). Surface optimization to eliminate hysteresis for record efficiency planar perovskite solar cells. *Energy & Environmental Science, 9*(10), 3071-3078.

Yang, F., Liu, J., Wang, X., Tanaka, K., Shinokita, K., Miyauchi, Y., . . . Matsuda, K. (2019). Planar perovskite solar cells with high efficiency and fill factor obtained using two-step growth process. *ACS Applied Materials & Interfaces, 11*(17), 15680-15687.

Yang, G., Chen, C., Yao, F., Chen, Z., Zhang, Q., Zheng, X., . . . Fang, G. (2018). Effective carrier-concentration tuning of SnO_2 quantum dot electron-selective layers for high-performance planar perovskite solar cells. *Advanced Materials, 30*(14), 1706023.

Yang, G., Qin, P., Fang, G., & Li, G. (2018). Tin oxide (SnO_2) as effective electron

selective layer material in hybrid organic–inorganic metal halide perovskite solar cells. *Journal of Energy Chemistry, 27*(4), 962-970.

Yang, L., Cai, F., Yan, Y., Li, J., Liu, D., Pearson, A. J., & Wang, T. (2017). Conjugated small molecule for efficient hole transport in high-performance p-i-n type perovskite solar cells. *Advanced Functional Materials, 27*(31), 1702613.

Yang, S., Dai, J., Yu, Z., Shao, Y., Zhou, Y., Xiao, X., . . . Huang, J. (2019). Tailoring passivation molecular structures for extremely small open-circuit voltage loss in perovskite solar cells. *Journal of the American Chemical Society, 141*(14), 5781-5787.

Yang, W. S., Noh, J. H., Jeon, N. J., Kim, Y. C., Ryu, S., Seo, J., & Seok, S. I. (2015). High-performance photovoltaic perovskite layers fabricated through intramolecular exchange. *Science, 348*, 1234-1237.

Yang, W. S., Park, B.-W., Jung, E. H., Jeon, N. J., Kim, Y. C., Lee, D. U., . . . Seok, S. I. (2017). Iodide management in formamidinium-lead-halide-based perovskite layers for efficient solar cells. *Science, 356*, 1376-1379.

Yao, K., Li, F., He, Q., Wang, X., Jiang, Y., Huang, H., & Jen, A. K. Y. (2017). A copper-doped nickel oxide bilayer for enhancing efficiency and stability of hysteresis-free inverted mesoporous perovskite solar cells. *Nano Energy, 40*, 155-162.

Ye, M., Hong, X., Zhang, F., & Liu, X. (2016). Recent advancements in perovskite solar cells: flexibility, stability and large scale. *Journal of Materials Chemistry A, 4*(18), 6755-6771.

Yin, X., Zhou, J., Song, Z., Dong, Z., Bao, Q., Shrestha, N., . . . Tang, W. (2019). Dithieno[3,2-b:2′,3′-d]pyrrol-cored hole transport material enabling Over 21% efficiency dopant-free perovskite solar cells. *Advanced Functional Materials, 29*(38), 1904300.

Yu, H., Yeom, H. I., Lee, J. W., Lee, K., Hwang, D., Yun, J., . . . Jang, J. (2018). Superfast room-temperature activation of SnO2 thin films via atmospheric plasma oxidation and their application in planar perovskite photovoltaics. *Advanced Materials, 30*(10), 1704825.

Zhang, H., Nazeeruddin, M. K., & Choy, W. C. H. (2019). Perovskite photovoltaics: The significant role of ligands in film formation, passivation, and stability. *Advanced Materials, 31*(8), 1805702.

Zhang, H., Wu, Y., Shen, C., Li, E., Yan, C., Zhang, W., . . . Zhu, W. H. (2019). Efficient and stable chemical passivation on perovskite surface via bidentate anchoring. *Advanced Energy Materials, 9*(13), 1803573.

Zhang, J., Hua, Y., Xu, B., Yang, L., Liu, P., Johansson, M. B., . . . Hagfeldt, A. (2016). The role of 3D molecular structural control in new hole transport materials outperforming Spiro-OMeTAD in perovskite solar cells. *Advanced Energy Materials, 6*(19), 1601062.

Zhang, J., Shi, C., Chen, J., Wang, Y., & Li, M. (2016). Preparation of ultra-thin and high-quality WO_3 compact layers and comparision of WO_3 and TiO_2 compact layer thickness in planar perovskite solar cells. *Journal of Solid State Chemistry, 238*, 223-228.

Zhao, B., Niu, G., Dong, Q., Liu, J., Li, N., Li, J., & Wang, L. (2018). The role of interface between electron transport layer and perovskite in halogen migration and stabilizing perovskite solar cells with Cs_4SnO_4. *Journal of Materials Chemistry A, 6*(46), 23797-23804.

Zhao, Z., Gu, F., Li, Y., Sun, W., Ye, S., Rao, H., . . . Huang, C. (2017). Mixed-organic-cation tin iodide for lead-free perovskite solar cells with an efficiency of 8.12. *Advanced Science, 4*(11), 1700204.

Zheng, X., Chen, B., Dai, J., Fang, Y., Bai, Y., Lin, Y., . . . Huang, J. (2017). Defect passivation in hybrid perovskite solar cells using quaternary ammonium halide anions and cations. *Nature Energy, 2*(7), 17102.

Zhou, H., Chen, Q., Li, G., Luo, S., Song, T., Duan, H. S., . . . Yang, Y. (2014). Interface engineering of highly efficient perovskite solar cells. *Science, 345* 542-546.

Zhou, H. P., Chen, Q., Li, G., Luo, S., Song, T.-B., Duan, H.-S., . . . Yang, Y. (2014). Interface engineering of highly efficient perovskite solar cells. *Science, 345*(6196), 542-546.

Zimmermann, I., Urieta-Mora, J., Gratia, P., Aragó, J., Grancini, G., Molina-Ontoria, A., . . . Nazeeruddin, M. K. (2016). High-efficiency perovskite solar cells using molecularly engineered, thiophene-rich, hole-transporting materials: Influence of alkyl chain length on power conversion efficiency. *Advanced Energy Materials, 7*(6), 1601674.

Zuo, L., Chen, Q., Marco, N. D., Hsieh, Y.-T., Chen, H., Sun, P., . . . Yang, Y. (2017). Tailoring the interfacial chemical interaction for high efficiency perovskite solar cells. *Nano Letters, 17*, 269-275.